March 2018

Defect Detection in Additive Manufacturing Utilizing Long Pulse Thermography

James Pierce
University of South Florida, jrpierce@mail.usf.edu

Defect Detection in Additive Manufacturing Utilizing Long Pulse Thermography

by

James Pierce

A thesis submitted in partial fulfillment
of the requirements for the degree of
Master of Science in Mechanical Engineering
Department of Mechanical Engineering
College of Engineering
University of South Florida

Major Professor: Nathan B. Crane, Ph.D.
Kyle Reed, Ph.D.
Wenjun Cai, Ph.D.

Date of Approval:
March 20, 2018

Keywords: pulse heating, infrared reflection, thermal diffusivity, nondestructive, quality

ACKNOWLEDGEMENTS

I would like to acknowledge my advisor Dr. Nathan Crane for accepting me to work in his lab and give me the opportunity to pursue a M.S.M.E and further my education via research. His guidance and assistance throughout my research is in part the reason for the completion of this thesis. I would also like to acknowledge my fellow lab partners who would go out of their way to assist in any issues or questions I experienced when working on this thesis. USF undergraduate Ishaat Hussain is also recognized for his help with thermal testing of BJ printed parts.

TABLE OF CONTENTS

LIST OF TABLES

LIST OF FIGURES

ABSTRACT

Additive Manufacturing (AM), over the years, has seen a tremendous amount of research for improving the manufacturability of materials into final products. The main advantages of additive manufacturing are the minimizing of waste material as it is an additive process. As well as the ability to create custom low-volume products without the need for creation of expensive tooling or programming before manufacturing begins. Because of these advantages, however, AM is susceptible to unique challenges in the quality side of manufacturing. These challenges include minimizing and detecting defects during the build. The focus of this research looks at the capability of using Pulse Thermography (PT), a nondestructive testing method, with longer than typical pulse length on additively manufactured parts for surface and sub-surface defect detection as well as thermal property determination based on a known void depth.

The first and second part of this research will look at a range of pulse lengths greater than 100ms to determine if the previously defined assumption is necessary for accurate defect detection. The significance of increasing the pulse length is to have the ability to increase the overall energy input into the part without having to increase the power. Allowing for the capability of defect detection for both shallow and deeper defects with the same overall setup. One-dimensional simulations r using Forward Time Center Space (FTCS) approximation, show that the assumption of an instantaneous pulse is relative, and defects can be accurately calculated within a range of pulse lengths. Based on the simulations, experimentation was conducted to determine the capability of calculating sub-surface defect depths with a longer pulse on a FDM printed ABS part with 100% in fill. The defect depths will range from 0.3mm to 1.8mm and the

widths of the defects used for depth calculation will be 8x8mm. Results of the experiments show that even with FDM printed parts defect depths were accurately calculated up to a depth of 1.2mm.

The third aspect of this research looks at the infrared reflections emitting off the surface during the longer pulse. With a longer pulse length, there is more time for the infrared camera to collect thermograms of the surface during the pulse. It was noticed during sub-surface defect detection that the infrared reflections paint a picture of the surface characteristics of the part. Characteristics that include surface imperfections not intended in the original build parameters such as under extrusions and cracks. Defects as small as 150μm with a thermal pixel resolution 75μm are detected.

The third and final aspect of this research looks at the ability to use PT with a longer pulse to determine thermal properties of a binder jetted additively manufactured part as well as packing factors that may be otherwise be unknown. When a product is binder jetted a chemical binder is added to the powder layer by layer until a product is formed.

CHAPTER 1: INTRODUCTION

1.1 Background to Additive Manufacturing

Manufacturing processes such as CNC machining, forging, sheet metal forming and more have been around for a very long time. The two types of manufacturing these processes fall under are subtractive and forming. Subtractive is where a product is cut away from a piece of stock material and forming involves reshaping the desired product from a piece of stock material [1]. Though these manufacturing processes have been around for years, they have some very specific drawbacks. For example, if a structurally strong part is needed, but weight reduction is critical, a lattice structure would be able to add the necessary support while keeping the weight at a minimum. It would be very difficult if even possible for a CNC machining process to be able to cut away an internal lattice structure. Or, if a part has a very complex geometry with tight tolerances; it would require multiple manufacturing processes to ultimately produce.

Recently, a new manufacturing approach has emerged on the market that addresses some of these drawbacks, and it is known as additive manufacturing (AM). Products are made by adding material layer by layer from the bottom to the top. Originally AM was called rapid prototyping because the process was mainly used as a quick way to build 3-dimensional prototypes of CAD models for hands on visualization of the design [2]. As the technology grew and the processes refined, the name was changed as parts were now being built not for prototypes, but instead as finished products used in the field. The major advantages additive manufacturing has over most other manufacturing processes are the ability to create low-volume custom, complex shapes without the need for initial expensive setup. Also, the material loss is

minimal in comparison as only the material needed to build the product is used. The leftover material, if any, can be reused in the making of another product. Thus, AM is increasingly gaining the interest of manufacturers and being used more and more for the build of final products [3].

There are multiple different AM processes, that specialize in different aspects; whether that is the type of material, dimensional accuracy, or strength of the part. The following sections will look at the more well-known additive manufacturing processes and discuss how these processes work to build a final part. Then based on the possible uses of each method the importance of quality, ensuring a part is built with minimal waste and defect free will be discussed.

1.1.1 Powder Bed Fusion

Powder Bed Fusion (PBF) is a description of the type of additive manufacturing processes that fuses the raw powder together layer by layer within a bed of powder to form a part. Different thermal sources including electron beam and laser can be used to fuse the material, though the laser is most common. When a laser source is used it is called Laser Sintering (LS) [2]. The powder is spread, layer by layer, on the bed either by a blade or counter-clockwise rotating cylinder. The layer thickness is typically 100μm. Upon completion of a newly spread layer, the powder is preheated and then the laser heats the layer to the dimensions of the specified cross section of the part. This process continues until a 3-dimensional part is formed.

The types of materials that can be made via LS include plastics, ceramic, metal and glass powder [3]. The benefits of LS is that there is no post curing of the powder required for proper strength and many parts can be built in a single build [4]. An example of laser sintered parts being studied for final product use are air cooled heat exchangers for power plants. Arie et al [5]

looked at direct metal Laser Sintered (dmLS) parts made by multiple materials for replacement of the current heat exchangers used in the plants. The goal was to be able to build the heat exchanger via additive manufacturing, that way to eliminate the need for post assembly operations to finish building the part. It was found that the Ti64 prototype heat exchanger produced an approximate 27% heat transfer density increase than the conventional dry cooling heat exchangers used.

1.1.2 Binder Jetting

Similar to PBF, Binder Jetting (BJ) utilizes a bed of powder to build the final part: that is however, one of the only similarities between the two processes. Instead of fusing the powder with a thermal source, BJ uses a binder to adhere the powder particles together. A layer of powder is spread across the bed and then the print head drops binder droplets, approximately 80μm in diameter onto the part in the shape of the cross-section of the part being built [2]. Besides the adhesion method between particles, BJ is also different in the fact that the freshly bound final part (green part) is quite fragile. Some binders require thermal post processing for adequate handling strength.

Once the binder is set, the part is removed from the powder bed and post processing can begin. This is to increase the part strength or mechanical properties to the final desired specifications. This is usually done by infiltrating the part with a lower melting point infiltrant. For most steel powders, the infiltrant is bronze. For other materials systems epoxy and cyanoacrylate have been used. The most common material used in BJ is metal powder, though a notable application in the automotive industry is the use of BJ to make sand molds and cores for

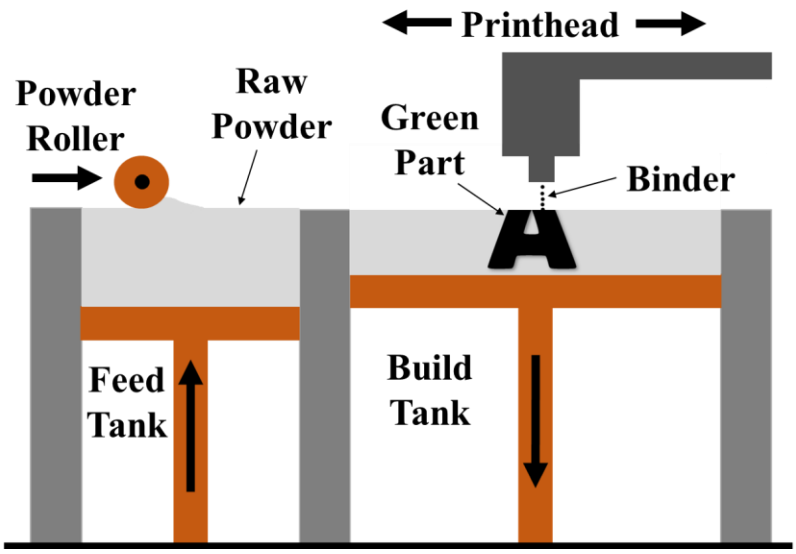

Figure 1.1 Schematic diagram of Binder Jet process

casting [2]. Though post processing is most likely required, because the binder is added to the powder to create the part and many jets can be used simultaneously to deposit the binder, it should be noted that the BJ process is very fast compared to LS processes.

1.1.3 Fused Deposition Modeling

Fused Deposition Modeling (FDM) is an extrusion based additive manufacturing system. A solid strand of material, the most common being Acrylonitrile Butadiene Styrene (ABS) and Polylactic Acid (PLA), are fed into and melted in the extruder head [6]. The melted material is then forced through the extruder head onto the build platform. This extruded material is commonly known as "roads" [2]. The roads are laid in a rastering pattern creating a single layer. Since FDM is done on a build plate and the material is extruded onto the plate, either the plate or the extruder head must move the appropriate layer height, before the process of the new layer can begin. This process continues until the part is completely built.

The benefit of FDM is the ability to create hollow, or cellularly structured parts with different infills. With powder-based processes, any hollow enclosure would be filled with raw

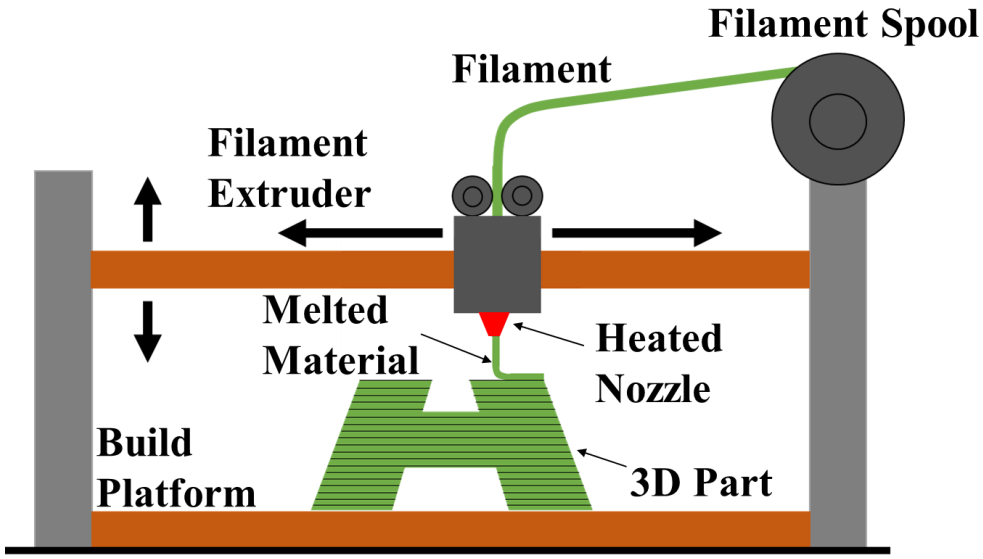

Figure 1.2 Schematic diagram of FDM process

powder. This is beneficial for reducing mass of a part that may not undergo major external forces. Unlike powder-based process however, once the filament is extruded in FDM, it becomes waste material if not utilized on the part. The amount of waste material can be substantial as shown by Song and Telenko. It was found that after a 10-week study, a commercial FDM printer in an open shop wasted about 34% of the overall plastic used [7].

In fact, whether it is waste, failed builds or part failure in the field due to defects; as AM continues to expand into the manufacturing industry the need for quality inspection of these builds must expand as well. The next sections will discuss the research being done regarding quality monitoring of additively manufactured parts, as well as inspection methods that are well known but less studied in the field of AM.

1.2 Quality in Additive Manufacturing

Quality control is an essential process in manufacturing to ensure defect-free final products. For most large-volume manufacturing processes, destructive testing of a finite sample of products is a viable method for defect detection. Large-volume allows for applying statistical

process control techniques and the cost of destructive testing is small, as it is limited to a small percentage of the parts. This approach is not effective for additive manufacturing.

The layer by layer process of AM allows it to excel in parts with low-volume and/or complex shapes. This creates a challenging environment for quality control. The complex geometries complicate quality assessment and the low quantities make destructive testing for quality control much more expensive. Also because of the customizable nature and point localized material introduction with AM, many more defect types and locations are possible. In FDM for example there are over 35 factors that can influence geometrical accuracy set by the operator alone, withholding variation from the process itself [8].

While quality might be assessed based on monitoring the process conditions, current control methods may be insufficient to guarantee that the same parameter set will consistently produce defect-free parts. Variations from input parameters as well as uncontrolled process and post-process variables may lead to variations between builds. This will affect all different types of AM technologies. For example, with powder-based processes, the powder particle size has normal variation [9]. Thus, within each layer, density variation may occur due to variation in particle size distribution at each point when the powder layer is deposited.

1.2.1 In-situ Process Monitoring in Additive Manufacturing

Given these challenges, significant work has been done to understand the processing conditions for a good product as a first step towards quality control. For example, Kousiatza and Karalekas [10] used fiber Bragg grating sensors (FBG) and thermocouples embedded in different layers of the FDM process for real time monitoring of residual strains and temperature profiles. Seppala and Migler [6] studied the ability to accurately measure welding zone temperatures in process to better understand the thermal characteristics during the build for improved weld

strengths. Taking this a step further Costa et al. [11] came up with an analytical solution to the heat conduction over time of the filament extrusion. They showed that the lower the extrusion temperature, the poorer the adhesion between roads. Improving the weld strength between roads of the FDM part will increase the overall strength as well as minimize the possibility of delamination between layers.

With melting processes, a lot of research have been done with studying the melt pool as well. The melt pool is the critical zone of any point localized melting process as that is the finite area that melts the powder and creates the part. With the thermal source localized to such a fine area, little variations in the energy input can change the outcome of the process. Craeghs et al. [12] used optical monitoring, via a CMOS camera and planar photodiode with a wavelength sensitivity of 400-900nm, to monitor the melt pool radiance. They studied the correlation with the laser location and the melt pool image data in a Selective Laser Melting (SLM) process to detect when the laser is overheating the powder. It was found that when mapping the melt pool with the laser in the X-Y plane instead of time, it could be seen when the laser is overheating an overhang (when melt pool is surrounded by raw powder) and in need of support structures to minimize the phenomenon. This overheating can ultimately affect the surface quality and create defects in the part.

Another studied method of monitoring the melt pool is via a combination of optical monitoring and thermal measurements of the surface with a pyrometer. It was shown by Chivel and Smurov that by monitoring the online optical surface temperature of the melt pool, they could determine the optimal parameters for adjusting the porosity of a SLS/SLM part. For a desired lower density part, minimal variation of the surface temperature near the melting point created by the pulsed laser action is desired, and vice versa for a higher porosity desired part

[13]. Similarly, with Electron Beam Melting, Tammas-Williams et al. [14] found via X-ray Computed Tomography (XCT) analysis as well, a correlation between pores with process parameters of the electron beam melting used for the outline as well as infill.

1.2.2 Nondestructive Quality Monitoring in Additive Manufacturing

The initial focus of most methods in the literature are in process monitoring as well as mechanical and thermal property control. This is critical to ensure the process is optimized, thus increasing the percentage of successful builds. In AM, as with other manufacturing processes however, there are possibilities of uncontrolled parameters, such as foreign debris in the filament, that can cause internal defects in the part: defects that could lead to decreased mechanical properties and possible part failure. Therefore, nondestructive methods for detecting defects are crucial in maximizing quality control for additively manufactured parts. With the improvements of process monitoring and control, research has shifted to nondestructive testing and defect detection.

With Selective Laser Melting (SLM), Rieder et al [15] also looked at detection of parts using ultrasound. They showed the capability of detecting a 2mm defect of unmelted powder in a cylinder made by a SLM process. Zeltmann et al [16], evaluated ultrasound for the ability to detect a 500μm defect in an FDM printed part; however, they were not able to distinguish the defect from the noise of the data. Another studied nondestructive testing method is optical coherence tomography (OCT) which produces a 3-dimensional representation of the part [17]. Guan et al showed that OCT detected micro-structural variations in the Selective Laser Sintered (SLS) part. However, they were only able to penetrate the part to a depth of approximately 400μm. Though, with layer thicknesses averaging 100μm, this could be a useful method for implementation for online process monitoring.

Another nondestructive method that enables non-contact measurement is infrared thermography. Infrared thermography measures the surface temperature on an object (usually at multiple points) to draw conclusions about subsurface features [18]. There are two types of infrared thermography techniques: active and passive. Passive is when a part or object being studied is producing its own heat source and active is when the object is heated and then the surface temperature is monitored. Examples of active techniques of infrared thermography in AM include evaluation of the heat affected zone in correlation with the laser scan strategy and part data of Inconel 718 in SLM, as well as sub-surface defects such as raw powder. Krauss et al. [19] found that by measuring the total irradiance of a layer during the exposure time they could detect raw powder defects as small as 100μm. The reason for this is because the heat transfer rate for raw powder is very slow in comparison to the already sintered powder. Schwerdtfeger et al [20] similarly, looked at a part built by an EBM process via an infrared camera during the build to monitor the temperature profile of the surface and determine if online defect detection was possible. When thermograms were analyzed in comparison with optical images taken of specific layers, Schwerdtfeger et al found the hotspots in the thermograms matched with that of the optical images taken at the same layer height.

These methods utilize the provided high powered localized heat source as well as the fast scan velocities in the process to analyze irregularities in the surface temperature and correlate them to surface and sub-surface defects. For AM processes such as BJ and FDM, these heat sources are not available. A more refined method of infrared thermography known as Pulse Thermography (PT), which looks at utilization of surface temperature monitoring after thermal excitation from an instantaneous pulse, will be discussed for defect detection with FDM parts in

Chapter 2. As well as utilizing known void space/raw unbound powder locations to determine thermal properties of parts in Chapter 5.

1.3 Objective and Scope

There has been a significant amount of work to improve the overall quality of parts made by AM. And it has shown, as more and more parts made by AM are no longer being used as prototypes, but instead as final products. Nondestructive testing methods have shown the capability to detect defects in AM parts. Infrared thermography among those methods is very attractive in AM as this method is relatively quick and is less sensitive to surface roughness [18]. However, there is little research in the quantification of defect depths of additively manufactured parts. The reason for this could be attributed to the lower thermal properties of thermoplastics and powders compared to common materials tested with the standard PT method. Thus, the goal of this thesis is to understand the capabilities of using active infrared thermography, more specifically a modified form of Pulse Thermography (PT), to detect and quantify surface and sub-surface defects in additively manufactured parts.

Pulse Thermography (PT) utilizes a thermal pulse to the surface of a part and monitors the spatial variation in the surface temperature over time. Materials previously studied utilizing this method of defect detection include glass fiber reinforced polymers (GFRP) and aluminum (Al) [21], 316 stainless steel [22], ceramic composite [23], and carbon fiber reinforced polymer (CFRP) [24]. In AM, this method could be applied for defect detection layer by layer or for sub-surface defects after a couple layers have been laid. This in turn, creates the possibility for online repair if a defect is detected before completion, reducing waste material.

In Chapter 2, an explanation of PT and how it can be utilized for qualification and quantification of sub-surface defects will be examined and discussed. A modified method of PT

using longer pulses (>100ms pulse) will be used based on a relaxation of the original assumptions for accurately quantifying surface and sub-surface defects. Then, the modified method will be utilized for post process sub-surface defect detection in FDM printed ABS. From there because of the modified method, the capability of surface characterization and defect detection will be reviewed.

Chapter 3 will further analyze the modification of the method by using a longer pulse (>100ms) and show how based on material properties, calculation of defect depth is relatively insensitive to pulses of varying lengths. First, the overall energy output from the setup will be evaluated and then, simulations will be studied to account for varying pulse lengths to still accurately quantify of defects. From there, simulations will be compared for two different materials (316 SS and ABS) to understand the limitations of increasing pulse lengths on accurate defect detection.

Chapter 4 will go into a deeper analysis of surface characterization by using the reflected infrared light from the thermal source into the IR camera. Including the aspects of FDM and the material that make it possible to characterize the surface defects with reflected light. Defects as small as 150μm with a thermal pixel resolution of 75μm are able to be differentiated and detected.

Chapter 5 will look at utilizing PT to determine thermal properties of BJ parts with known void depths in comparison to effective density. Based on these thermal property measurements, green parts will be analyzed for defect detection in the powder bed with the defects being raw unbound powder for capability of online implementation.

Finally, Chapter 6 will conclude the work of the research in this thesis and will look at future work that is needed to further improve understanding.

CHAPTER 2: DEFECT DETECTION IN FDM PRINTED ABS VIA INFRARED THERMOGRAPHY

Additive manufacturing (AM) offers many advantages due to the ability to form/pattern the material point by point. However, this also introduces many potential defect sources. Use of AM in critical applications requires new approaches to quality assurance to detect and/or eliminate these defects. Nondestructive testing method known as pulse thermography is a proven technique for defect detection and quantification of sub-surface defects. While this method has been studied with materials such as steel and ceramic composites, there has been little research on 3D printed thermoplastics. This paper shows that the pulse thermography method can be used effectively with longer, >100ms, pulse length on 3D printed acrylonitrile butadiene styrene (ABS) thermoplastic for detecting defects of depths from 0.3 mm to 1.2 mm. The benefit of being able to use a longer pulse is the ability to achieve the same energy into the part without requiring a high-power source. Radiant reflections in the infrared camera during the pulse are also shown to reveal small surface defects of the printed part such as under extrusions between roads and cracks in the surface.

2.1 Introduction

Quality control is an essential process in manufacturing to ensure defect-free final products. For most large-volume manufacturing processes, destructive testing of a finite sample of products is a viable method for defect detection. The large-volume allows for applying statistical process control techniques and the cost of destructive testing of the small sample is

modest. This approach is not effective for additive manufacturing where geometry is more complex and part volumes are much lower.

In Additive Manufacturing (AM), formerly known as rapid prototyping, a part is built by adding material layer by layer based on a digital design [2]. This layer by layer process allows for AM to excel in parts with low-volume and/or complex shapes. The complex geometries complicate quality assessment and the low quantities make destructive testing for quality control much more expensive. The point localized material deposition in AM creates many new defects types and more potential locations. While quality might be assessed based on monitoring the process conditions, current control methods may be insufficient to guarantee that the same parameter set will consistently produce defect-free parts. Variations from input parameters as well as uncontrolled process and post-process variables may lead to variations between builds. This affects all AM technologies.

Given these challenges, significant work has been done to understand the processing conditions for a good product as a first step towards quality control [25, 26]. For example, Kousiatza and Karalekas [10] used fiber Bragg grating sensors (FBG) and thermocouples embedded in different layers of the FDM process for real time monitoring of residual strains and temperature profiles. Seppala and Migler [6] studied the ability to accurately measure welding zone temperatures in process to better understand the thermal characteristics during the build for improved weld strengths. Taking this a step further, Costa et al. [11] came up with an analytical solution to the heat conduction over time of the filament extrusion. They showed that the lower the extrusion temperature the poorer the adhesion between roads. Improving the weld strength of the material extrusion (FDM) part will increase the overall strength as well as minimize the possibility of delamination between layers. Monitoring and control methods have also been

studied for selective melting processes as well. With Selective Electron Beam Melting, Tammas-Williams et al. [14] found a correlation between defects/pores with process parameters of the electron beam melting used for the outline as well as infill.

The initial focus of most methods in the literature are in process monitoring as well as mechanical and thermal property control. In AM, as with other manufacturing processes however, there are possibilities of uncontrolled parameters, such as filament diameter variation, foreign debris in the filament, and ambient humidity that can introduce variation or internal defects in the part. Therefore, nondestructive methods for detecting defects are crucial in maximizing quality control for additively manufactured parts. With the improvements of process monitoring and control, research has shifted to nondestructive testing and defect detection. Zeltmann et al. [16], evaluated ultrasound for ability to detect a 500μm defect, however, they were not able to distinguish the defect from the noise. Rieder et al. [15] also looked at detection using ultrasound. They showed the capability of detecting a 2mm defect of unmelted powder in a cylinder made by a Selective Laser Melting (SLM) process.

Another studied nondestructive testing method is optical coherence tomography (OCT) which produces a 3-dimensional representation of the part. Guan et al. [17] showed that using OCT they were able to detect micro-structural variations in the Selective Laser Sintered (SLS) part. They were however only able to penetrate the part to a depth of approximately 400μm. Another nondestructive method that enables non-contact measurement is infrared thermography. Infrared thermography measures the surface temperature on an object (usually at multiple points) to draw conclusions about subsurface features [18]. Pulse Thermography (PT), a form of active infrared thermography, utilizes a heating pulse applied to the surface of a part and monitors the spatial variation in the surface temperature over time. This method can quantitatively determine

defect depth [23]. In AM, this method could be applied as an online process, monitoring for sub-surface defects layer by layer or after a couple layers have been laid. If a defect is detected, the part might be repaired online or at least scraped immediately—saving time and material. This possibility, could significantly improve production efficiency as Song and Telenko [7] showed that failed prints resulted in wasting 19% of the overall material used.

If heat is applied to the surface in an instantaneous pulse, the surface temperature decay over time with one-dimensional heat conduction determined by Parker et al. [27]

$$T(t) = \frac{Q}{\rho C L}\left[1 + 2\sum_{n=1}^{\infty} exp\left(-\frac{n^2\pi^2}{L^2}\alpha t\right)\right] \quad (1)$$

where Q is the input energy on the surface, ρ is the density of the part, C is the specific heat, L is the thickness, and α is the thermal diffusivity. With an instantaneous heat pulse, there is a negligible internal temperature distribution at $t = 0$. The method also neglects heat loss of the surface to the surroundings. Once the surface is heated, the thermal energy conducts one-dimensionally through the material. Defects impede the thermal conduction forcing the energy to move around it in a three-dimensional flow. This creates a "hotspot" on the surface. From this concept, methods for quantitatively determining the defect depth were derived. Such methods include the peak temperature contrast slope method Ringermacher et al. [28] and log second derivative method from Shepherd et al. [29].

This paper utilizes pulse thermography with a long pulse (>100ms) instead of using an instantaneous pulse, for defect detection in FDM printed Acrylonitrile butadiene styrene (ABS) parts. The benefit of using a longer pulse is the ability to achieve the same overall heat energy input without requiring a large input power. This work also shows how infrared reflection from

the radiant heat source can reveal surface features. These effects were not accounted for in prior work [30].

2.2 Analysis of Thermography Quantification Methods

Several alternative methods have been proposed for extracting defect depth from surface time history data [21,23,28,29]. The most common alternatives are summarized below.

2.2.1 Peak Temperature Contrast Slope Method

Most defects generate a low thermal conductivity region where material is missing, or where bonding between layers is lost as in a delamination. When a defect is present within a part, the 3D conduction path around the defect slows heat transport from the surface and a change in the surface temperature decay is observed, as seen in Figure 2.1(a). This produces a temperature contrast over time as seen in Figure 2.1(b) where temperature contrast is defined as the difference between the surface temperature over a defect compared to a sound region. Ringermacher et al. [28] found that the time the peak slope of this temperature contrast curve occurs is directly proportional to the square of the defect depth. The correlation between the defect depth and the peak slope time (t_s) is expressed as

$$t_s = \frac{3.64L^2}{\pi^2\alpha} \tag{2}$$

where L is the defect depth. This method requires a reference sound area to calculate the temperature contrast. In the research by Ringermacher et al. [28], the reference sound temperature was taken as the average over the entire surface. This method works if the defect area is a small percentage of the total surface area of the part and the heating is uniform.

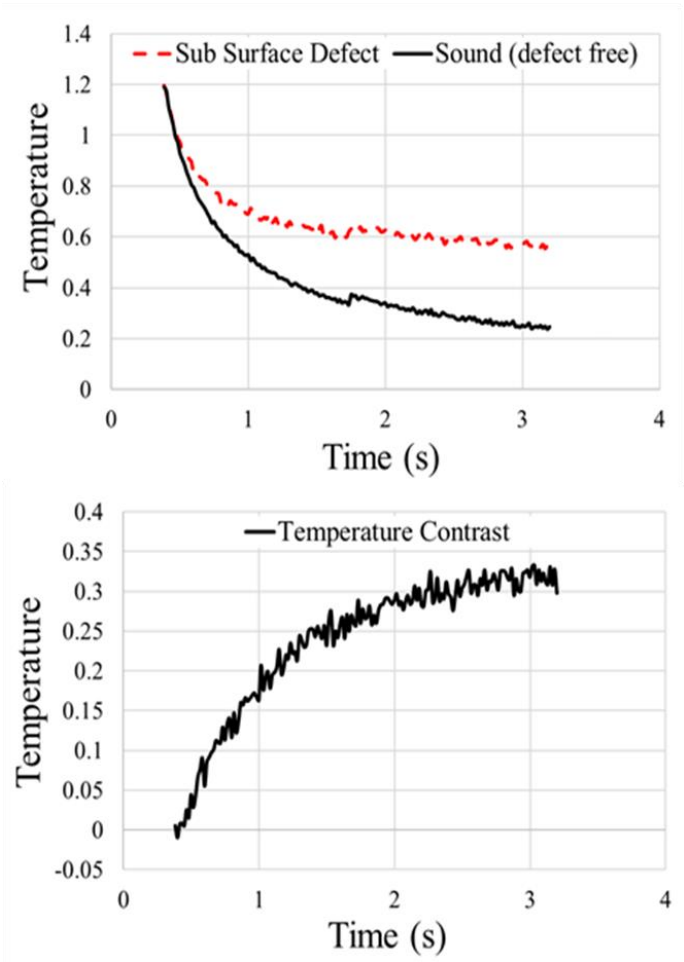

Figure 2.1 (a) Surface temperature decay curve of a sound (defect free) area of the part versus an area with a sub-surface defect. (b) Temperature difference between the defect area and the sound area of the part.

2.2.2 Log Second Derivative Method

When the temperature and time is plotted in the logarithmic scale the ideal temperature decay curve is linear, with a slope of -0.5 as expressed as

$$\ln\big(T(t)\big) = \ln\left(\frac{Q}{\sqrt{\pi\rho C\alpha}}\right) - \frac{1}{2}ln(t) \tag{3}$$

When a defect is present the temperature in the log scale will deviate from the linear trend as seen in Figure 2.2. Shepherd et al. [29] found that the second derivative of the log temperature of

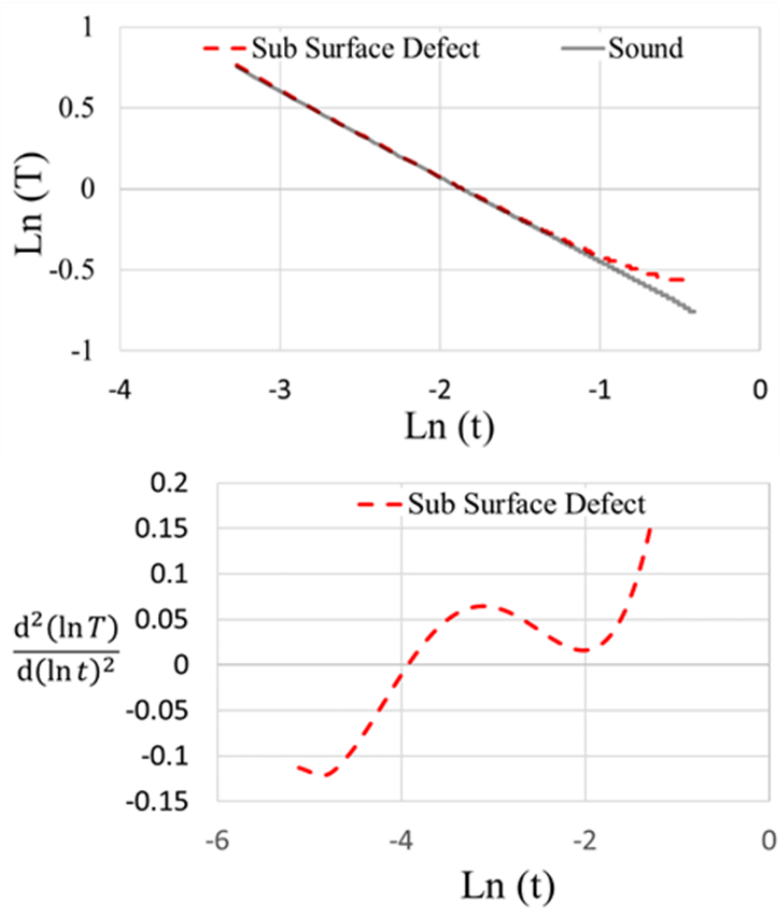

Figure 2.2 (a)Temperature over time in the logarithmic scale of an area with a sub-surface defect and a sound area. (b) Second derivative of the surface temperature decay where a defect is present in the log scale.

the defective region will produce a peak. The time where this peak occurs is proportional to the square of the defect depth. The equation for determining the defect depth from the peak second derivative time (t_2) is expressed as.

$$t_2 = \frac{L^2}{\pi\alpha} \tag{4}$$

Unlike the peak temperature contrast slope method, the log second derivative method does not require a reference sound area for determination of defect depth.

Literature reports of these methods have focused on pulse lengths of 2-10ms that approximate well the instantaneous pulse assumption. For materials such as steel, these short pulses are required to accurately detect the peak slope. Literature results show accurate detect defection to depths of 1.83 mm with peak temperature contrast method. The pulse length required to approximate the instantaneous pulse assumption will depend on both the diffusivity of the material and the depth of the defect. Since thermal diffusivity of ABS and other thermoplastics ($\alpha \approx 1.2 \times 10^{-7}$)is much smaller than for steel ($\alpha \approx 4 \times 10^{-6}$), a longer pulse is possible. The time difference is in fact proportional to the thermal diffusivity differences. Pulse length may be increased further by relaxing the assumption of negligible internal temperature distribution.

2.3 Experimental Procedure

Instead of flash lamps as required for a 2-10ms pulse, two 500W halogen bulbs rated for 120V, 56 degrees from incidence of the surface, were flashed for 300ms at 120 V. After the pulse of heat is completed two shutters are rotated into place blocking the halogen bulbs from the part as seen in Figure 2.3(a). Even after the pulse is completed the halogen bulbs emit radiant heat while cooling down. This radiant heat not only continues to input energy into the part but also reflects off the surface. This reflection introduces error in the infrared temperature measurements. The infrared camera used for the experiments is a FLIR SC4000 MWIR reading infrared in the midwave spectrum 3-5μm with a 50mm indium antimonide (InSb) lens. The frame rate was set at 60hz with a focal plane array of 320x256 pixels.

Upon completion of the pulse and the shutters engaged, blocking the radiant heat, the surface temperature was monitored for a total time of 15 seconds. A sample ABS part was printed using FDM with intentional defects introduced. These defects used in these calculations were 8 mm x 8 mm. The average temperature taken over the surface area of the defect was used for calculation of the depths. For the reference sound area, an average temperature was taken in the closest sound region to each defect depth with the same overall surface area as the defect. A reference sound area was taken for each defect to minimize any error from spatial variation in heating intensity across the surface.

Acrylonitrile butadiene styrene (ABS), one of the more common FDM printed thermoplastic materials was used for defect depth prediction. A 50x80x8mm rectangular part was printed with four different defect depths with three difference widths for each depth. The schematic of the printed part is shown in Figure 2.3(b). To minimize reflectivity and increase absorptivity the part was printed with black ABS. The defect depths were approximately 0.3, 0.8, 1.2, and 1.8mm. The layer patterning was set to standard and an infill pattern of 100% was used. Due to the variations in thermal properties that can arise from the printing process, additives in

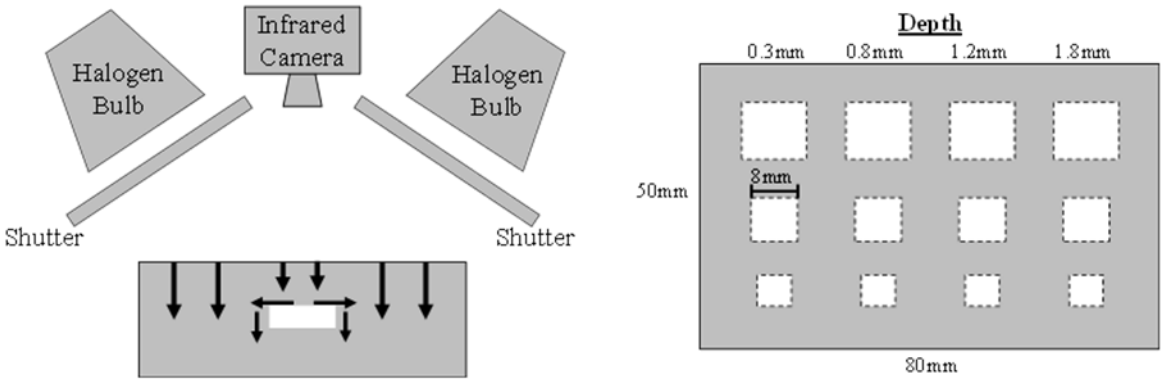

Figure 2.3 (a) Schematic diagram of the experimental setup for pulse thermography testing. (b) Schematic diagram of the ABS printed part used for testing defect depth calculations.

ABS			
Boundary Conditions			
Insulated	All 4 sides and bottom		
Radiation	Emissivity 0.9	Atm. Temp. 298K	View Factor 1.0
Convection		Coef. for air 10.45	Atm. Temp. 298K
Heat Power	Variable step function pulse length on the surface		

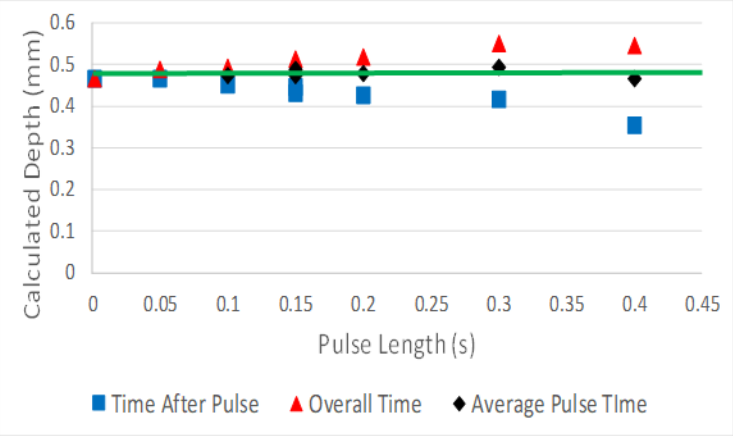

Figure 2.4 (a) Boundary conditions for simulation of ABS. (b) Calculated depths for a 0.5mm defect depth using the three peak slope time values with different starting times (t_0)

the ABS material, and the AM process itself, the thermal diffusivity used was based on the best fit of calculated depths. Each measurement was repeated multiple times in order to assess the repeatability of the method.

2.4 Measurement Starting Time Analysis

From equation (2), the peak slope time is directly proportional to the square of the defect depth. As the pulse length increases, the instantaneous heat input assumption will break down and ultimately change the calculated depth. To understand how this would affect the calculations, a Solidworks thermal simulation of a 0.5mm deep defect was analyzed with the boundary conditions shown in Figure 2.4(a). Due to the longer peak slope times with a low thermal diffusivity material like ABS, heat losses consisting of radiation and convection will be included in the simulation. Further discussion of the effects of the heat loss on the depth measurement is explained in Chapter 3. Three different starting points were used for the peak slope time calculation of the defect depth. The first value was the total time with t_0 starting at the end of the pulse, the second value was the time with t_0 starting at the beginning of the pulse, and the third value for depth calculation was the time with t_0 starting in the middle of the pulse.

Figure 2.4(b) shows the calculated depths from each of the peak slope time values. At short pulse times, all give the same results. However, when starting t_0 at the end of the pulse, the calculated depths decrease with increasing pulse length and when starting t_0 at the beginning of the pulse the calculated depths linearly increase with increased pulse length. When using the peak slope time value with t_0 starting at half the pulse length the calculated depths become independent of pulse length over the range studied. Extending the pulse length allowed for more energy input which increases the temperature contrast to detect deeper defects.

2.5 Results and Discussion

Figure 2.5 shows the surface temperature over time with the 300ms pulse. After nine seconds of surface monitoring the three defect depths of 0.3, 0.8, and 1.2mm are visible in the thermal image. The 1.8mm defect is not visible in the thermal image at any time step nor in the temperature contrast data as seen in Figure 2.6(a). Beyond 1.2 mm depth, any temperature difference between sound and defect regions are within the measurement noise. Presumably, more energy input is required for measurement of the depth of 1.8mm. Therefore, for the 1.8mm defect depth, pulse lengths of 1.5s, 4s, and 6s are used for quantification of defect depth.

2.5.1 Peak Temperature Contrast Slope Method

In order to reduce noise, a small rectangular region of pixels was averaged at each time point for the sound and defect region. The defect depths were calculated by taking a polynomial fit of the temperature contrast data, and then the first derivative of that as seen in Figure 2.6(b) was taken to find the peak slope times t_s. Based on the simulation results, $t = 0$ is taken as the midpoint of the pulse and it can be seen in Figure 2.7(a) that the theory is confirmed and that

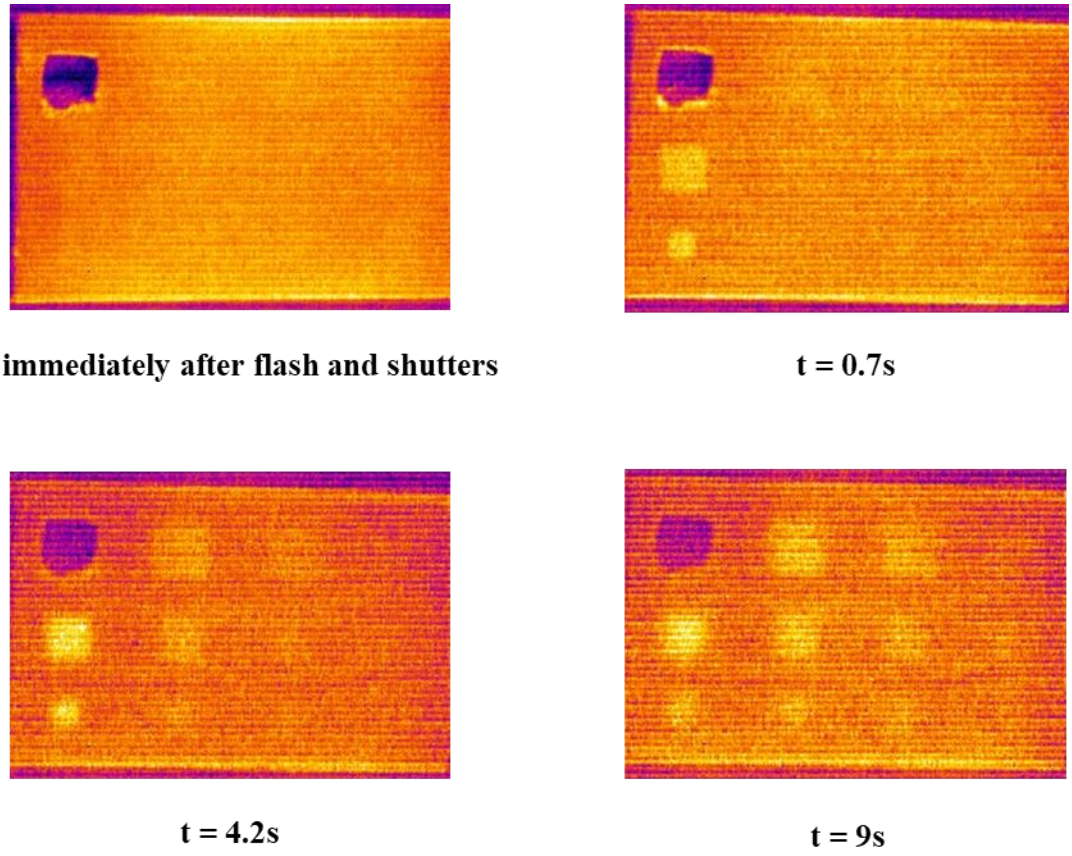

Figure 2.5 Thermal images over time of FDM printed ABS part. NOTE: The cool spot in the top left corner is a cutout that was made for depth analysis and not considered a defect for analysis purposes.

even with a longer pulse the defect depths can be calculated using the peak temperature contrast slope method.

As the defects get deeper, the variation of the calculated depth gets larger when using the peak temperature contrast slope method. That is as expected however, because the deeper defects create a much smaller temperature gradient as energy is dissipated over time. With these smaller temperature gradients, it becomes harder to differentiate from noise in the temperature measurement and the effects of substrate defects. Also, the deeper the defect the larger cross-sectional area required for accurate depth calculation. The 8x8mm width of the 1.8mm defect is not large enough for accurate prediction within ABS which has a low thermal diffusivity.

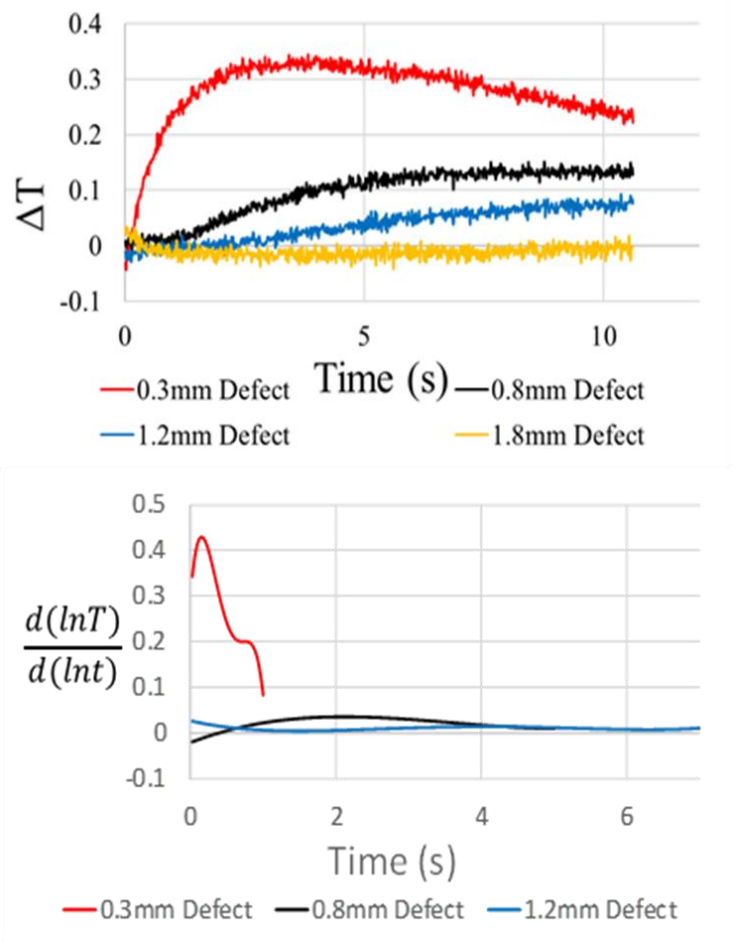

Figure 2.6 (a)Temperature contrast plotted over time for each defect depth. (b) First derivative of the polynomial fit of the temperature contrast data for peak slope time calculations.

Beyond 1.2 mm, the calculated depths were consistently shallower than the actual depth. This may be due to the approximations in the quadratic time/depth relationship. However, with AM, this is not the area of greatest interest for sub surface defect detection. For online process monitoring, defect depth quantification would be focused for only a few layers to allow for the possibility of repair or scrap before build completion. Deeper defects would be more of a qualitative analysis to determine if a defect such as delamination is present in the part.

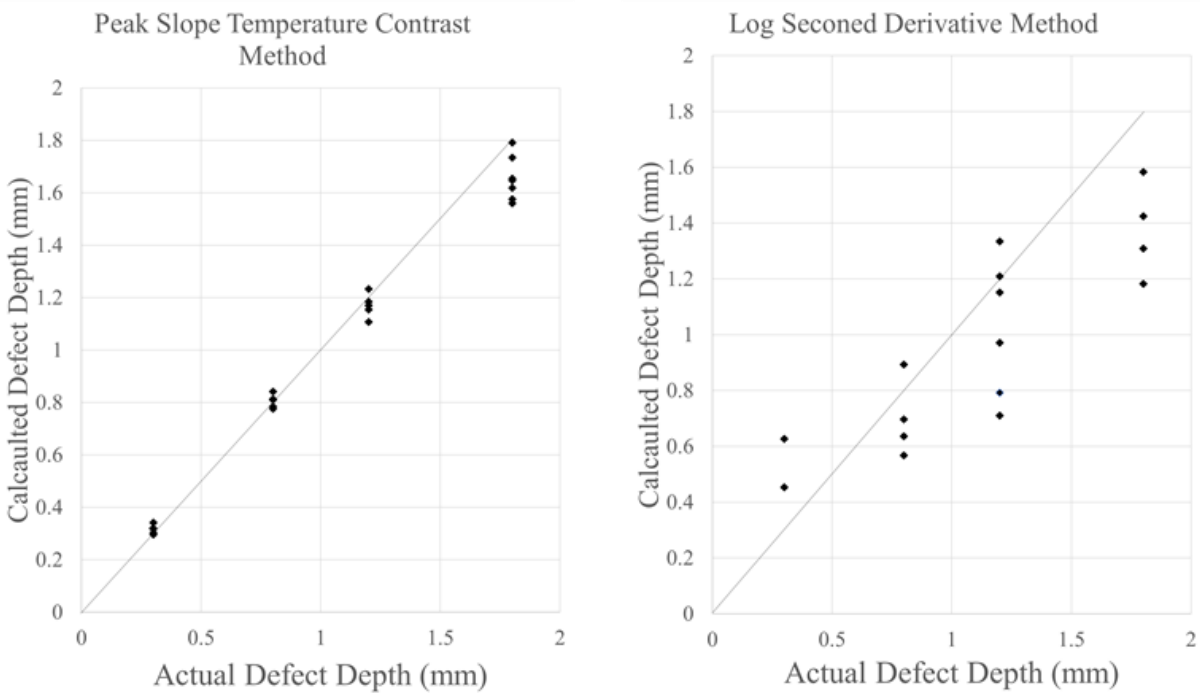

Figure 2.7 (a) Results for calculated defect depths using the peak temperature contrast derivative method. (b) Results using the log second derivative method.

2.5.2 Log Second Derivative Method

Using the log second derivative method it can be seen in Figure 2.7(b) that with this experimental setup, the depth calculations have a much larger variation. This could be attributed to the internal temperature distribution from the longer pulse or compounding noise from taking the second derivative of the small temperature rise. Thus, for low thermal diffusivity materials like ABS and the tested pulse conditions, the peak temperature contrast method gives better results. As such, based on these studies different pulse conditions, reduced measurement noise, or improved post-processing is necessary for effective defect depth calculation using the log second derivative method.

2.6 Analysis of Reflections

Even with the capability to detect sub-surface defects within a few layers, material and machine time are wasted as the defective area has already been printed over with new layers. Therefore, the most effective form of defect detection would be on the surface; monitoring each layer as it is laid. Allowing for immediate repair if a defect is detected. For this level of process monitoring, reflected light in the infrared spectrum can be used to characterize the surface and detect some types of defects before an additional layer is printed.

Quantitative analysis of Sub-surface defect depth focuses on the decay of surface temperature after the end of the pulse. The effectiveness of sub-surface defect detection via pulse thermography depends on the size of the defect and the depth. As shown from the results, depths were accurately calculated up to 1.2mm with an 8x8mm width defect. When it comes to mechanical properties however, defects much smaller than this can cause mechanical failure in the part. Anna and Selcuk [31] found that during tensile testing, some ABS parts were failing prematurely because of small imperfections/defects including microcracks in the surface. Thus, the ability to detect fine defects is critical for part performance.

With a longer pulse, there is time for the IR camera to measure IR light from the heat source reflected off the part. During the pulse, the reflected IR light dominates the radiated light. The spatial intensity of the reflected light varies based on the characteristic curvature of specific points on the surface relative to the radiant heat source. When an area of the surface creates a large enough angle from the horizontal plane towards the normal of the heat source, the infrared light will reflect into the IR camera creating a “hotspot”. The hotspot reflections of the infrared light reveal surface characteristics of the part being pulsed that are otherwise undetectable via emitted radiation alone and sometimes difficult to see with optical inspection except under high

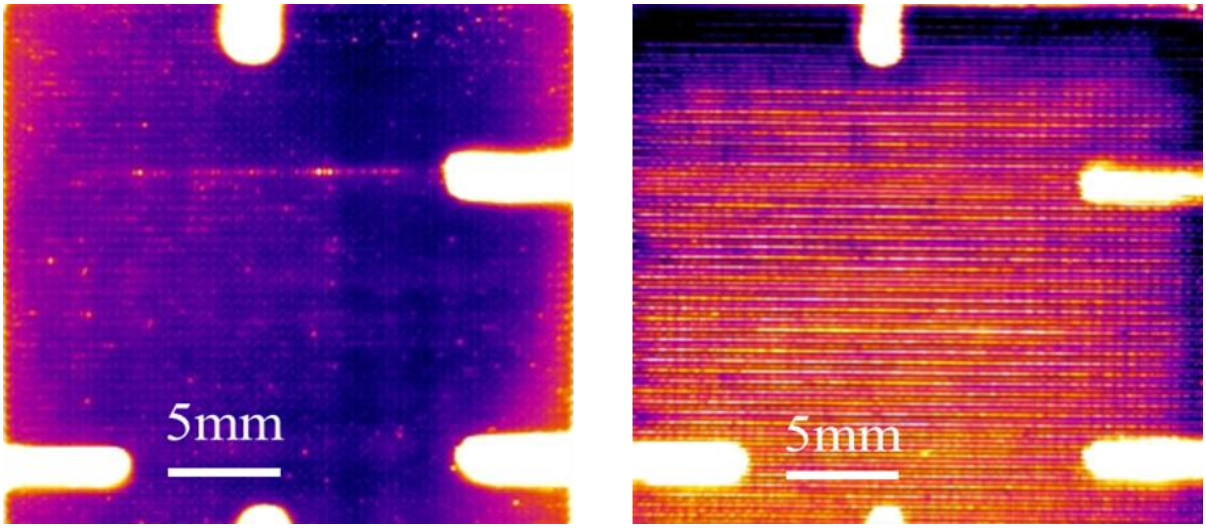

Figure 2.8 (a) IR image of an ABS printed 20x20mm part during the pulse with the road direction in line with the IR light source. (b) The same part but rotated where the road direction is perpendicular to the heat source. NOTE: the bright spots on the part in the IR image are marker lines for reference purposes only.

magnification. This can be seen in Figure 2.8 where an ABS printed 25.4x25.4mm part was flashed with a longer pulse and then after the pulse, the shutters engaged blocking the part from the heat source. The hotspot reflections of the infrared light reveal surface characteristics of the part being pulsed that are otherwise undetectable. These surface characteristics can reveal defects. Once detected, they can be repaired with minimal waste as no layers have been laid above them.

The two main aspects that affect how the light is reflected, is the road direction compared to the heat source, seen in Figure 2.9, and the high frequency surface roughness of the part, seen in Figure 2.10. When the road direction is parallel to the heat source none of the incident angles are large enough to reflect the IR light directly into the camera and create a hotspot except those caused by defects on the surface. If the heat source is perpendicular to the road direction, the large and small roughness interact in that the high frequency surface roughness compounds the large-scale angle of the surface from the road spacing allowing for the

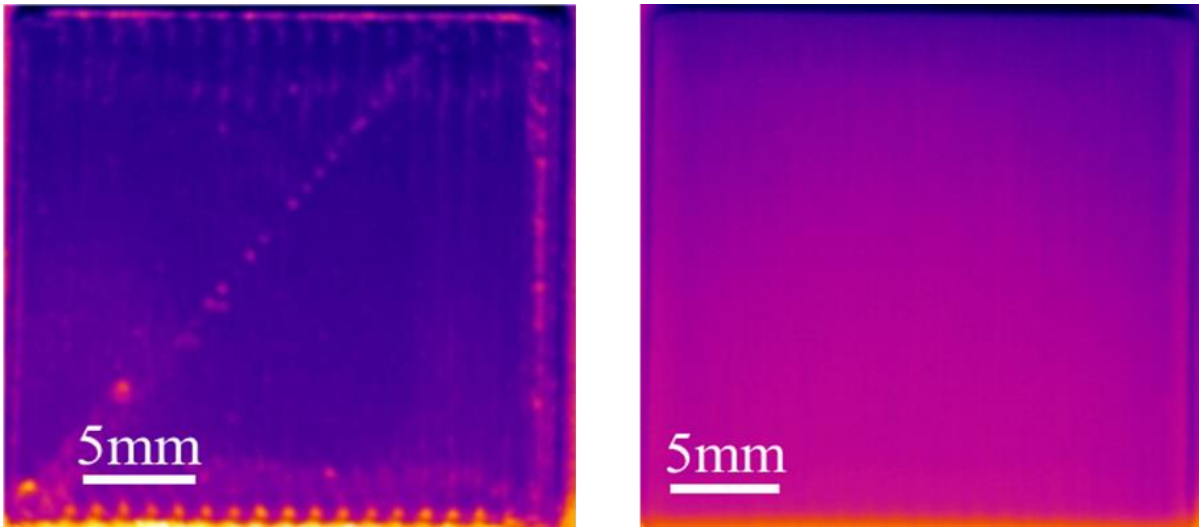

Figure 2.9 (a) IR image of an ABS printed part during the pulse heating. (b) After the pulse heating has completed and shutters are blocking the radiant heat with the heat source in line with the road direction.

light to be reflected into the IR camera at a greater intensity from the road edges. Without the high frequency surface roughness, little light is reflected into the camera. This was demonstrated by optically heating the surface of a printed part so that a thin surface layer melted. This removed the high frequency roughness but not the overall roughness of the surface. The effect is

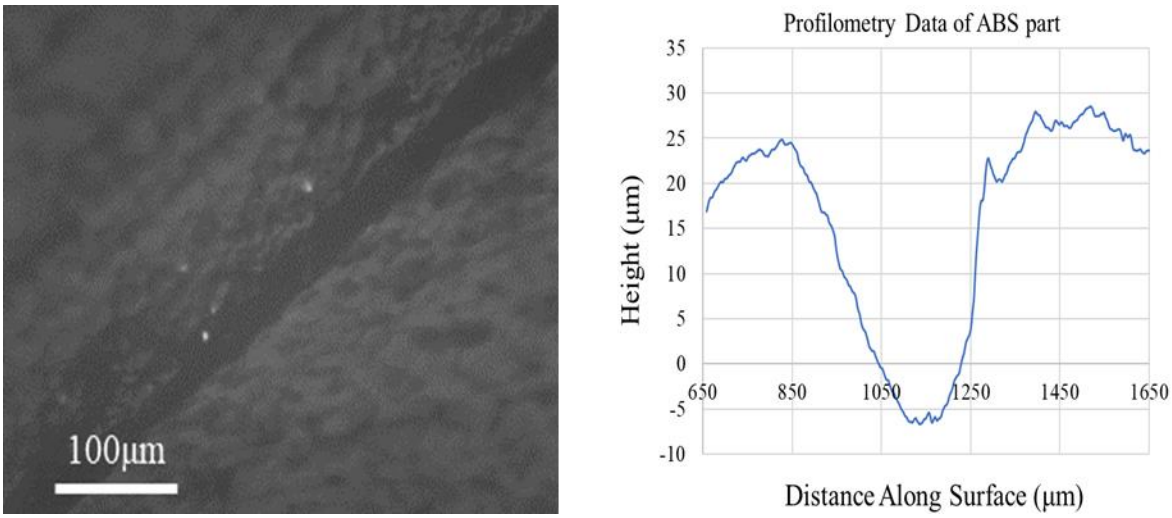

Figure 2.10 (a) Microscopic image of the surface of an ABS printed part. (b) Profilometry data showing the high frequency roughness along the surface.

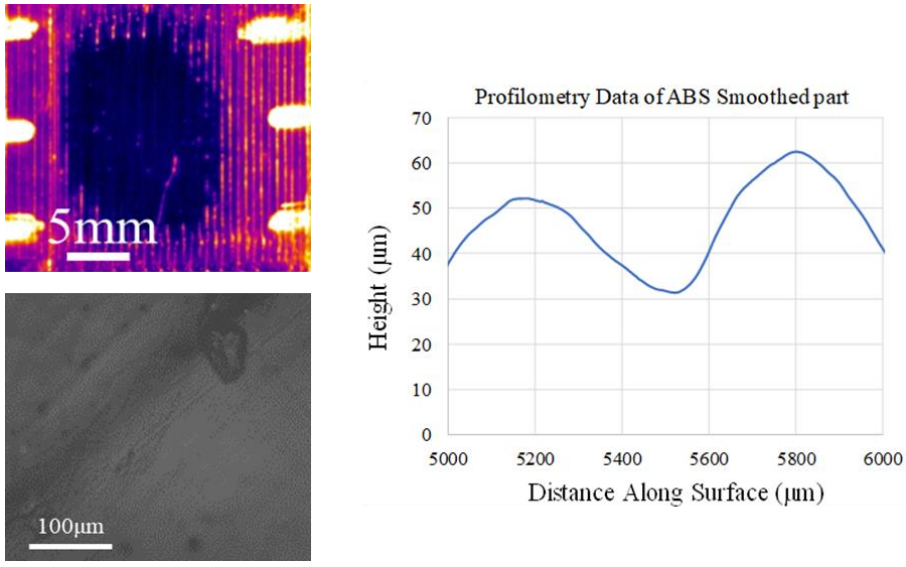

Figure 2.11 (a) IR image of ABS part that was partially thermally smoothed in the center to eliminate the high frequency roughness. (b) Profilometry data showing the transition from the surface with the high frequency roughness and the thermally smoothed area without any high frequency roughness. NOTE: the bright spots on the part in the IR image are marker lines for reference purpose only.

seen by comparing profilometry measurements with and without smoothing in Figure 2.10 and 2.11. When the IR source is perpendicular to the road direction, the thermally smoothed region reflects much less IR light and the edges of the roads are not clearly visible. Figure 2.12 shows

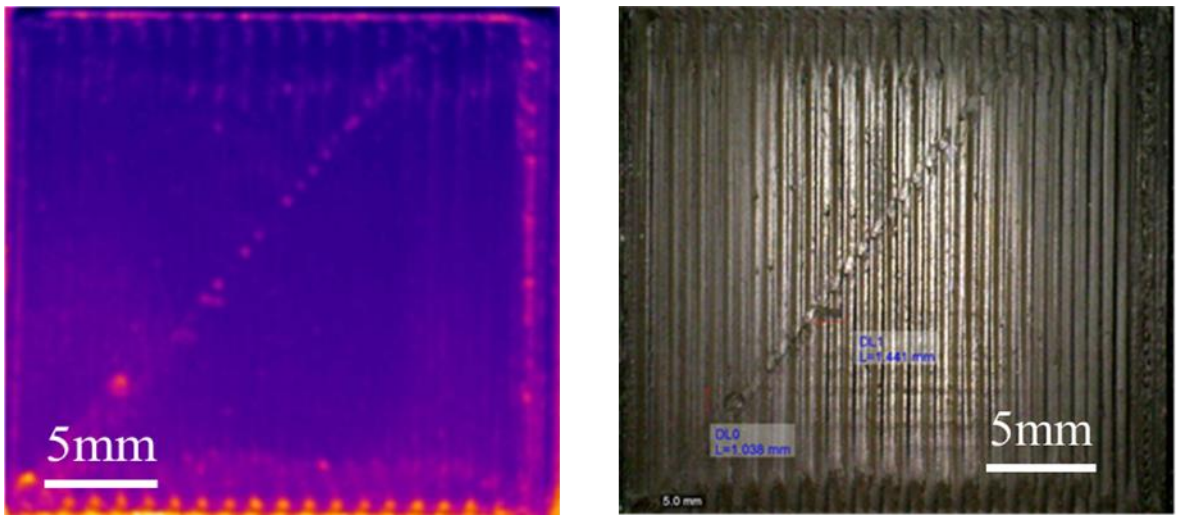

Figure 2.12 (a) IR image of ABS printed part during pulse and (b) optical image of the same ABS part.

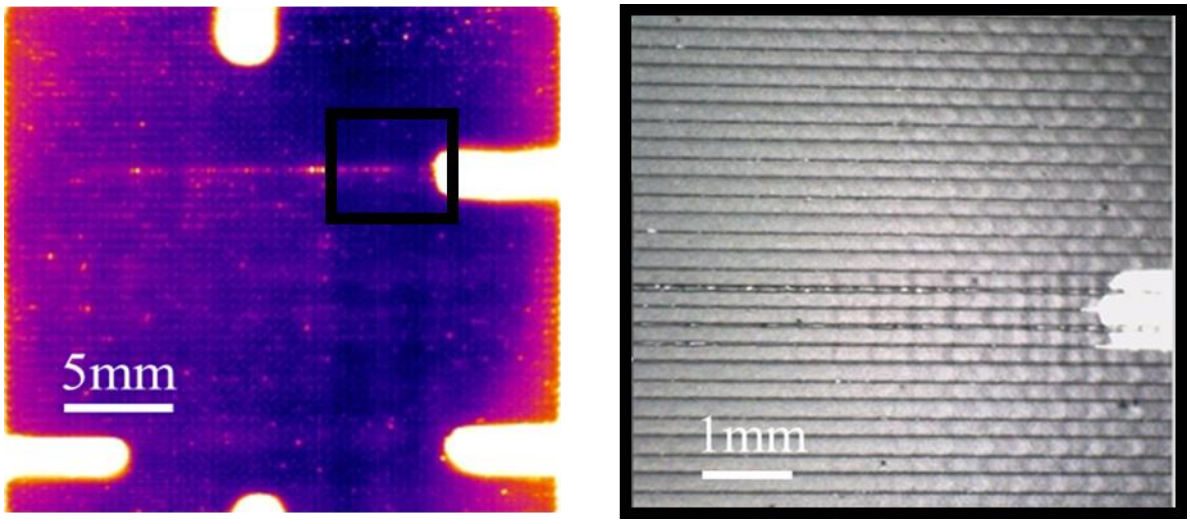

Figure 2.13 (a) IR image of ABS part showing a hot spots line across the surface and (b) Optical image of ABS part revealing the under extrusion. NOTE: the bright spots on the part in the IR image are marker lines for reference purpose only.

that during the pulse the IR image had consecutive hotspots forming a diagonal across the part and one large circular hotspot. When comparing this to the optical image it confirms that these are surface imperfections not intended in the original printing process. Figure 2.13 shows that when the road direction is in line with the heat source that the IR image will be able to detect under extrusions as well. This is because an under extrusion exposes the filament layer beneath which is perpendicular to the heat source, therefore, the infrared light is able to reflect into the IR camera off the road edges. The defects that can be detected via reflection of the infrared light are quite small compared to sub-surface defects. Analyzing the 25.4x25.4mm ABS part, surface imperfections detected via radiant reflections were as small as 150µm. With a thermal pixel resolution of approximately 75µm, that is only 4 pixels for defect detection. With sufficient lighting intensity and low ambient IR light, it may also be possible to detect defects smaller than a single pixel.

2.7 Conclusion

This work shows that using a longer pulse of greater than 100ms in pulse thermography is still an effective method of determining defect up to 1.2mm deep in ABS polymer. At greater depths (1.8mm), the defects could be detected, but the actual defect depth was below the calculated depth. This is most likely attributed to the width of the defect being too small for accurate depth calculation with the low thermal diffusivity material of ABS. It may also be related to the limits of the temperature/depth models used. However, this depth is not of the greatest interest in AM for online process monitoring and can be viewed more as a qualitative depth detection. As the goal for sub-surface defect depth detection in AM is the capability of early detection for possible repair or scrap with minimal waste. The log second derivative method was not as consistent in defect depth detection as the peak temperature contrast slope method with a longer pulse and this is most likely attributed to the magnified error with the second derivative and the low temperature gradients from the energy input by the setup. Future work will look at a more refined model to further determine the effectiveness of this method with longer pulses. With a longer pulse this study also shows that the reflected infrared light can be used for defect detection on the surface of printed ABS parts. Defects such as under extrusions, cracks in the roads, and other nonconformities as small as 4 thermal pixels can be seen. Thus, with a longer pulse, the surface of each layer can be monitored via reflected infrared light while sub-surface defects within previous layers can be detected and quantified to maximize quality control information in the AM part.

CHAPTER 3: LONGER PULSE CAPABILITY

In Chapter 2, it was shown that defects within a 3D printed ABS part can be detected with a pulse that is longer than 2ms; more specifically greater than 100ms. Increasing the pulse length allows for more energy input into the part, creating a larger temperature contrast. Thus, minimizing the possibility of error in defect depth quantification. It also creates the opportunity for surface characterization via infrared reflections off the surface which will be further discussed in Chapter 4. The goal of this chapter however, is to answer the question and understand: What are the limitations of increasing the pulse length based on the material properties of the part? To answer this, simulation analysis of varying pulse lengths for four different materials with different defect depths will be conducted. And a conclusion will be made for the limitations of increasing pulse length.

3.1 Introduction

Pulse Thermography (PT) is a form of infrared thermography for quantification of sub-surface defects in materials. This method utilizes flash heating on the surface of a part and measuring the temperature decay of that same surface via an infrared (IR) camera. When a part is flash heated with thermal energy, the surface of the material is heated and then 1-dimensional (1D) conduction begins into the part. Thus, the surface temperature will begin to decay immediately following the flash of thermal energy. The decay of the surface temperature also shown in Chapter 2 follows the equation:

$$T(t) = \frac{Q}{\rho C L}\left[1 + 2\sum_{n=1}^{\infty} exp\left(-\frac{n^2\pi^2}{L^2}\alpha t\right)\right] \quad (5)$$

derived by Parker et al. where Q is the total input energy, C is the specific heat capacity of the material, ρ is the density of the part, and α is the thermal diffusivity [27]. The equation was derived with three major assumptions: no heat loss from the surfaces of the part, the thermal input is an instantaneous pulse (Dirac Pulse), and thus, there is a finite negligible internal temperature distribution.

To ensure negligible internal temperature distribution previous work utilizing this method [21-24,28,29] have used flash lamps to thermally excite the surface of the specimens they were testing. Pulse lengths from the flash lamps are typically 2-10ms, though most of the research conducted in PT aims for the shorter flashes. Where a defect such as foreign material or a void such as a delamination is present within the part, the effective thermal resistance is much higher than over the sound area of the part. This slows down the heat transfer within the part directly above the defective region, thus producing a thermal contrast on the surface in comparison to sound areas of the part. There are many methods that have been found to quantify the defect depth based on this thermal contrast on the surface, but the two most common methods previously discussed in Chapter 2 are the peak temperature contrast method and log second derivative method [28,29].

The questions become, what defines negligible internal temperature distribution? With a wide range of materials, and thus a wide range of thermal properties. A negligible internal temperature distribution does not require the same pulse length for 316 stainless steel, with a thermal diffusivity approximately 50 times larger than ABS P400. However, the pulse length

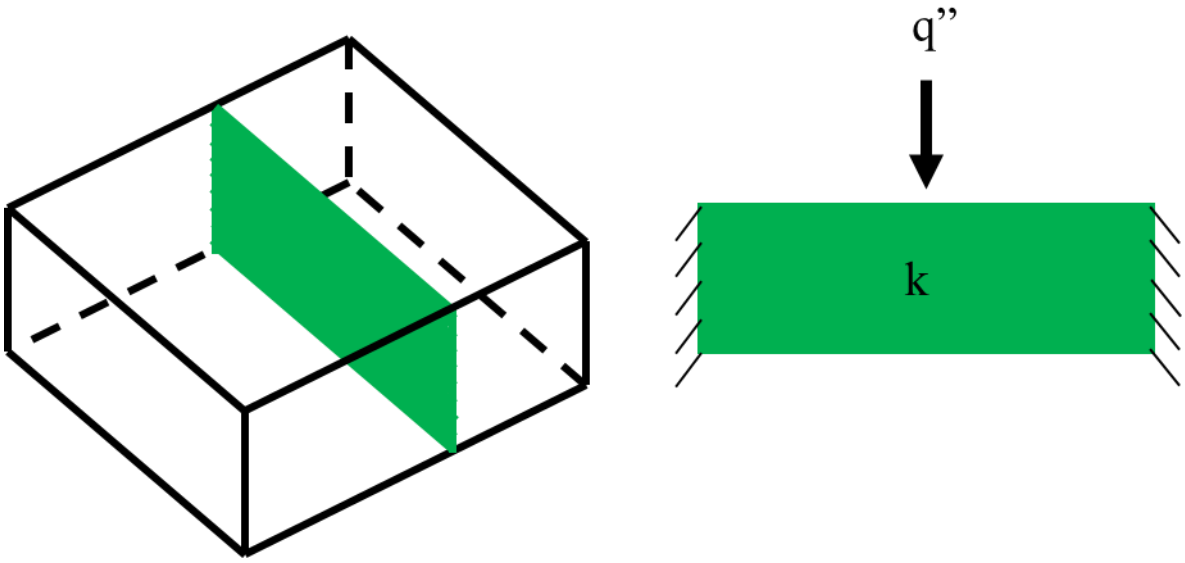

Figure 3.1 Schematic representation of the 1D boundary conditions for PT.

requirements and their dependence on the material properties of the sample have not been characterized. Thus, the next sections will discuss the benefits of using a longer pulse and analyze how the material properties of the sample effect the internal temperature distribution and limitation of pulse length. In turn, answering the question of how long is too long for accurate depth calculation.

3.2 Benefit of Longer Pulse

Two flash lamps of 2000 watts (W) flashed for a range between 2-10ms produces a range of 8-40 joules (J) of energy that is projected onto the surface of the part being thermally excited. By simply increasing the flash duration form 2 to 10ms (5x), the energy input increases as well 5x. To be able to increase the amount of the energy even more would require a larger capacitor to store more energy. However, by using a steady continuous voltage supply for longer pulses, the same energy input of 32J can be produced with two 500W halogen bulbs flashed for 40ms. And halogen bulbs can be flashed for much longer time, increasing the energy even more.

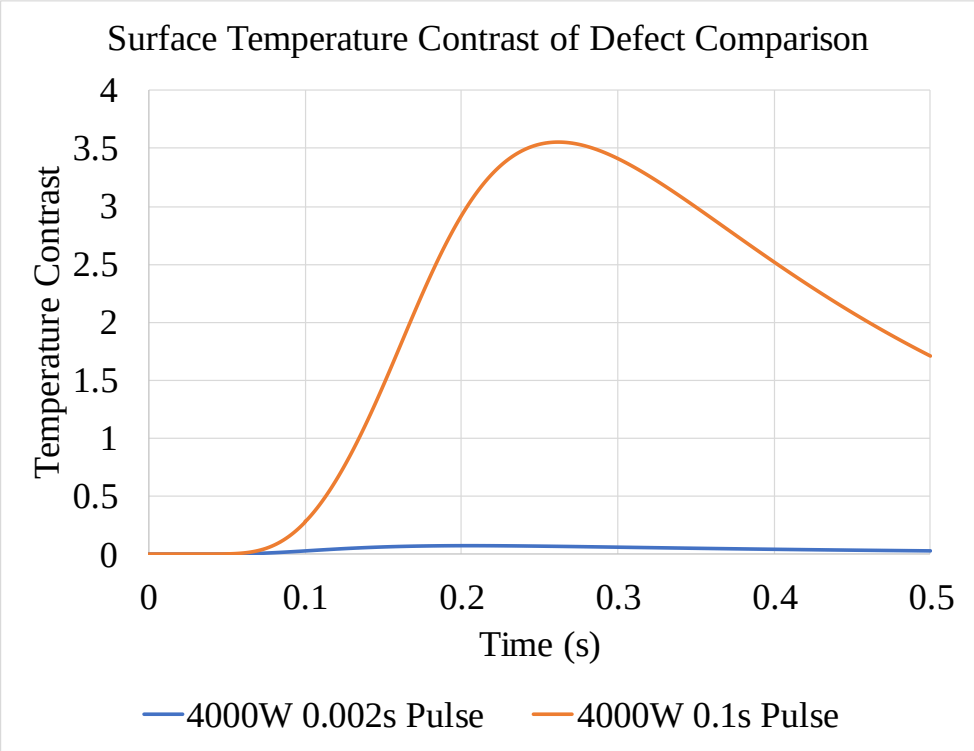

Figure 3.2 Temperature contrast comparison between a 2ms pulse and a 100ms pulse with the same power of 4000W

The longer pulse capability would allow for the possibility to increase the energy input, without having to change the power source to maximize the power. This can be seen in Figure 3.2, showing the temperature contrast difference between 4000W power source flashed for 2ms compared to the same power flashed for 100ms. For materials with large thermal diffusivities or shallow defects this may not be as critical as the temperature signal is large enough to overcome thermal noise. However, for materials with small thermal diffusivities and when analyzing deeper defects, the ability to simply adjust the pulse time to increase the energy allowing for a larger temperature signal is quite appealing.

This ability to use a longer pulse is especially attractive in the Additive Manufacturing (AM) of metal components via powder processes. As shown by Masamune and Smith [32], thermal conductivity of powder beds is significantly smaller than the thermal conductivity of

their bulk material counterpart. Thus, the thermal diffusivities are significantly smaller as well. Therefore, the longer pulse would be required for defect detection to get a large enough thermal contrast for accurate quantification purposes. The longer pulse would allow for the capability to expand PT into the AM industry as a viable nondestructive testing method.

Previous studies have already begun to look at the benefits of longer pulses up to the extent of what could be considered continuous heating for defect detection. Kim et al [33] looked at using active thermography with a heating duration of 150s to detect wall thinning in nuclear pipe components. The focus of the study was not to quantify the depths however to simply determine if the method was effective in detecting the defects, which it was. Recently Almond et al [34] studied a new method of analytical quantification of defect depths using pulse lengths of 5s on 4 different materials based on the thermal contrast of the defective region produced from a specific heat flux. Based on the estimated heat flux applied to the surface above a defective region, they could compare the experimental temperature contrast to predicted contrast and correlate that to a prescribed defect depth. It was shown that for materials with lower thermal conductivity the method proved effective in determining defect depths, though it was mentioned that deeper defects were more accurately predicted. From an online monitoring standpoint for AM however, these methods would be less effective as the pulse lengths required would drastically increase build times and shallower defects would be more difficult to quantify.

The research in this chapter however, analyzes the capability of using longer pulse lengths while still utilizing the depth/time correlation based on the assumption of negligible internal temperature distribution derived by Parker et al. With this approach, multiple quantification methods can still be utilized for defect detection, including defects within a layer

or two of the surface. This method of longer pulse could allow for possible implementation into online quality monitoring for additive manufacturing processes.

3.3 Analysis of Internal Temperature Distribution

Reviewing the typical case of two 1600W flash lamps flashed for 2ms. If all that energy was absorbed by a 316 L grade stainless steel (SS) part, with a thermal diffusivity of 4.055×10^{-6} ($m^2\ s^{-1}$) that had a surface area of 10,000mm^2, then the overall heat flux onto that part would be 320,000 ($W\ m^{-2}$). The internal temperature distribution equation given for a constant heat flux of a semi-infinite body is:

$$T(x,t) = \frac{2q^{"}}{k}\left[\left(\frac{\alpha t}{\pi}\right)^{\frac{1}{2}} e^{\frac{-x^2}{4\alpha t}} - \frac{x}{2} erfc\left(\frac{x}{\sqrt{4\alpha t}}\right)\right] \quad (6)$$

and when analyzed after the idealized 2ms pulse, an internal temperature distribution can be seen in Figure 3.3(a) [35]. With a 2ms pulse, there is approximately 2 degrees of temperature increase experienced on the surface of the part. Internally, down to 0.1mm the temperature increased by 0.5 degrees. Not until approximately 0.3mm beneath the surface of the part is there a negligible temperature effect from the flash heating. In comparison, Figure 3.3(b) shows the internal temperature distribution of ABS P400, which has a thermal diffusivity of 8.104×10^{-8} ($m^2\ s^{-1}$) [36]. After the 2ms pulse the temperature increase on the surface reaches upwards of 25 degrees. Yet because the thermal diffusivity is so low that beyond 0.05mm the internal temperature has not been affected.

ABS P400 is much closer to the assumption of negligible internal temperature distribution under the same pulse. Yet the 316 L grade SS has been experimentally proven to work for quantification of defect depths using PT [22]. Increasing the pulse length subjected to

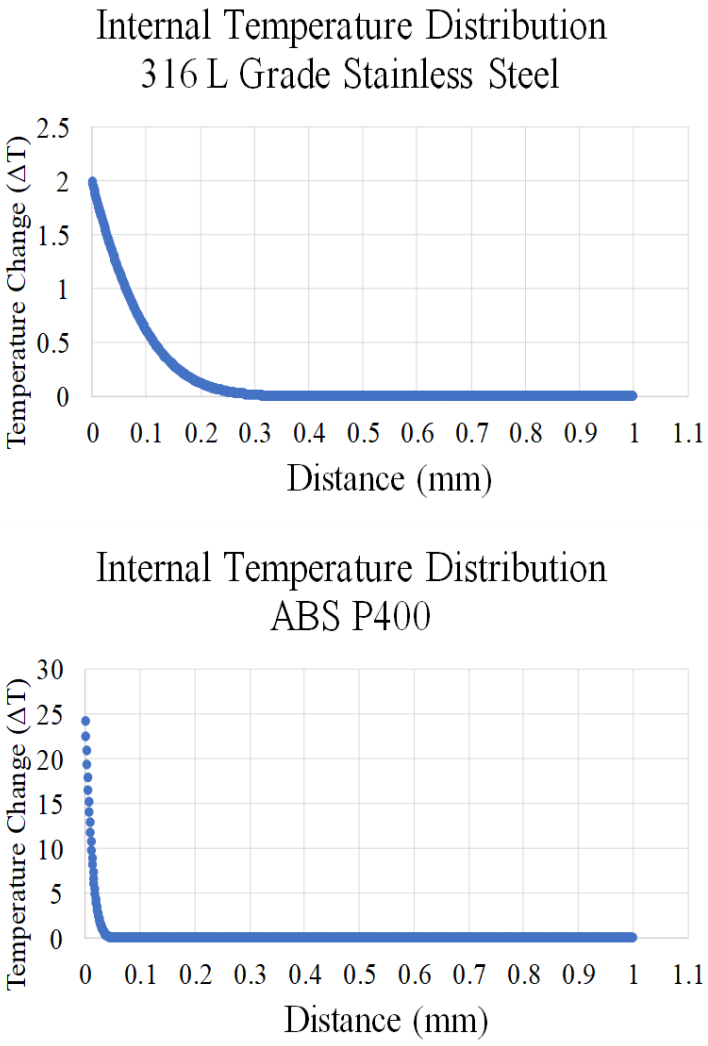

Figure 3.3 Internal temperature distribution of 316 L grade SS after 2ms pulse (a) and internal temperature distribution of ABS P400 after 2ms pulse (b).

ABS P400 up to 100ms produces the same internal temperature distribution as a 2ms pulse produces in 316 L grade SS. Now, at what point does a longer pulse become too long for the given material of the specimen to where the actual assumption truly breakdowns? As discussed in Chapter 2, numerical simulation suggested that much longer pulses could be used successfully with the temperature contrast slope method as long as the start time was taken as the middle of the pulse. To understand the limitations of the longer pulse for a given material a continued

analysis of numerical simulations will be analyzed for multiple materials with a wide range of thermal diffusivities. The start time for the simulations will be at the halfway point of the pulse.

3.4 1D Study of Pulse Length Limitation for Accurate Defect Detection

3.4.1 Simulation Model

As previously discussed in the chapter, the method of Pulse Thermography (PT) is based on 1D heat conduction into the part from the surface. Therefore, as seen in Figure 3.4, the simulation will look at two finite cross-sectioned portions of the part for the defective and sound region. The numerical approximation method that will be utilized for temperature analysis of each section is the Forward Time Center Space (FTCS) method. The FTCS is an approximation method derived from the 1D heat equation:

$$\frac{\partial T}{\partial t} = \alpha \frac{\partial^2 T}{\partial t^2}, \qquad 0 < x < L, \quad t \geq 0 \tag{7}$$

where α is the thermal diffusivity of the material and L is the thickness of the part. For derivation of the spatial and time approximation for the FTCS method see [37].

It is important to note that the FTCS method is not unconditionally stable. This means that if the time step is set to large based on the spatial discretization and material property of the part, then the solution becomes unstable. For a stable solution, the value of r:

$$r = \frac{\alpha \Delta t}{\Delta x^2} < \frac{1}{2} \tag{8}$$

must be less than the constant 0.5. For proof of why keeping r below 0.5 produces a stable solution with the FTCS method refer to [38]. Thus, for the simulations, the time discretization was varied based on the material being simulated.

Figure 3.4 Schematic representation of the simulation model used for PT

The software used to run the simulation is MATLAB. The code for both the log second derivative method and the peak temperature contrast method can be seen in the appendix. To confirm the simulation is accurately calculating the temperature distribution within the part and on the surface, a comparison was made to the calculated surface temperature by Solidworks simulation with the same boundary conditions. The boundary conditions will be further discussed in the next section. Figure 3.5 shows the surface temperature comparison between the two simulations. Under the same boundary conditions, the MATLAB simulation is very similar to the Solidworks simulation. Though with minor differences, mostly due to the fact the MATLAB program is ran with a much finer spatial discretization, the time where the defect temperature and sound temperature separate is the same. Confirming the MATLAB simulation will produce accurate results.

3.4.2 Simulation Model Parameters

The 1D heat equation derived by Parker et al [27] utilizes the assumption that there are no heat losses. The assumption is suggested to be met because the measurements are taken in a short time period, thus very little cooling takes place. However, with deeper defects or small thermal diffusivities, the peak times occur much further from the end of the pulse. As the cooling time

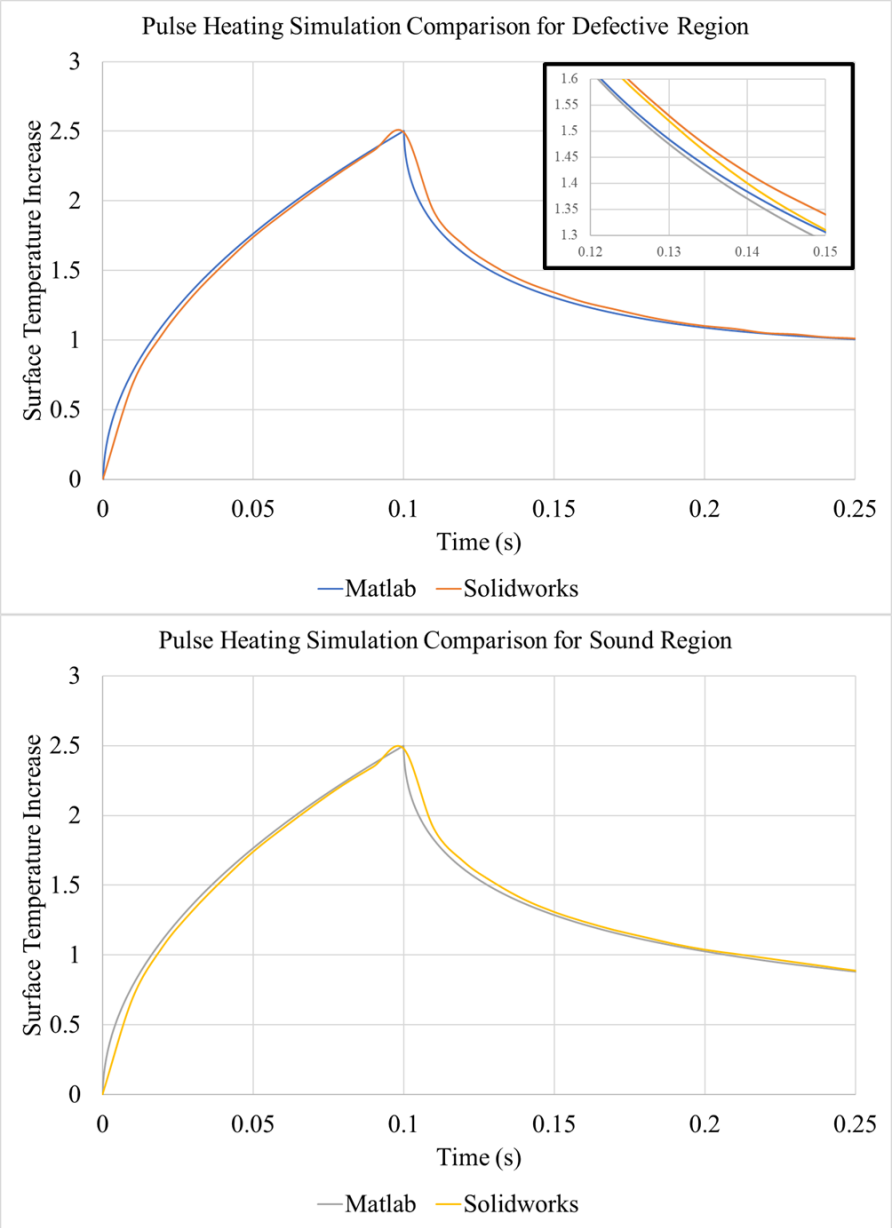

Figure 3.5 Surface temperature comparison after 100ms pulse heating between Solidworks simulation and MATLAB simulation

increases, there is an increased possibility for the thermal losses to affect the measurements. To understand the effect heat losses has on the defect depth calculation, simulations were ran with and without heat losses. The boundary conditions and heat losses applied can be seen Table . The emissivity value of 0.9 was chosen to increase the effect of radiative heat loss as well as to better represent practical experimentation cases as most low emissivity materials are coated with a thin

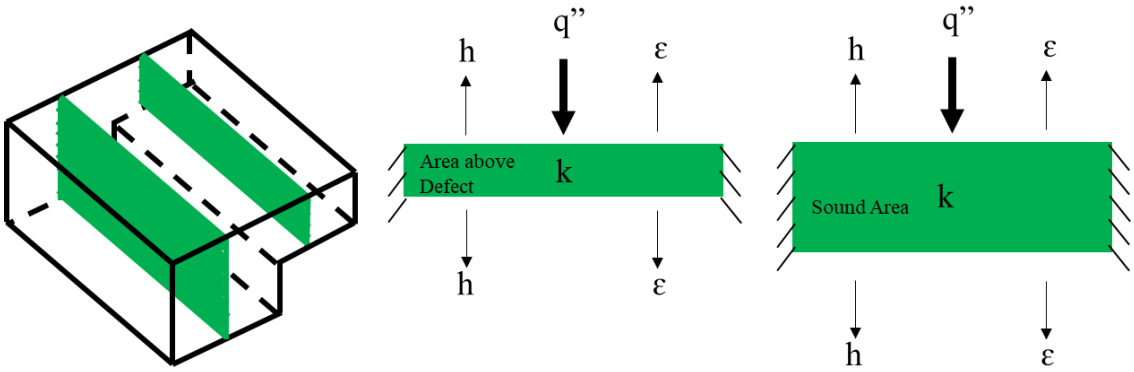

Figure 3.6 Schematic representation of the boundary conditions used for the simulation

layer of black paint. Based on the simulation results, with no heat loss the defect depth calculation for both the log second derivative and peak slop contrast method were insignificant compared to the calculated defect depths with heat loss as seen in Figure 3.7. It should be noted however, that the sensitivity to the heat loss is material dependent causing more variation with heat losses in Figure 3.7. This variation though, would be less significant than the possible variation and error from noise and fitting of the temperature data. While there was negligible difference between the calculated defect depths with and without heat loss under the comparison conditions, the simulations were continued assuming heat loss for more accurate practical representation as the assumption may be less accurate for all materials studied.

The overall boundary conditions can be seen in Figure 3.6. Convective and radiated heat losses are applied to the surface of the part and the back surface of the defect. The constants used for each boundary condition can be seen in Table . The sides are set as insulated boundary conditions based on the 1D conduction analysis and the heat power is a unit step function varying with pulse length. The use of a unit step function for the thermal excitation is explained is further explained in the appendix. The power applied during each pulse length was set at 4000W.

Table 3.1 Simulation boundary condition

Boundary Conditions		
Insulated	All 4 sides and bottom to promote 1D conduction	
Radiation	Emissivity = 0.9	Atm. and Initial Temp. 298 K
Convection	Coef. for Air 10	Atm. and Initial Temp. 298 K
Heat Power	4000W step function with variable pulse lengths	

3.4.3 Simulation Results and Discussion

Defect depths were calculated using both the log second derivative and the peak slope temperature contrast method as seen in Figure 3.7. Four materials with a range of thermal properties as seen in Table 3.2 were analyzed for defect depth quantification. The results of the simulation were analyzed based on the percent error from the actual defect depth. The data was normalized for the different materials based on pulse length, nullifying the affects that different material thermal properties have on the allowable pulse length. The normalization parameter used is (t_p/t_d). The variable t_p, is the time of the pulse length in seconds used for thermal excitation of the material and t_d is the actual calculated time for each defect depth based on the

Table 3.2 Material properties of the four materials used in the defect depth simulation

Material	Thermal Conductivity, K ($Wm^{-1}K^{-1}$)	Specific Heat Capacity, C ($Jkg^{-1}K^{-1}$)	Density, ρ ($kg\ m^{-3}$)	Thermal Diffusivity, α (m^2s^{-1})
ABS	0.2256	1386	1020	$1.5958x10^{-7}$
316 L grade SS	16.2	500	7990	$4.0551x10^{-6}$
PLA	0.13	1800	1300	$5.5556x10^{-8}$
Copper	400	398	8912	$1.1277x10^{-4}$

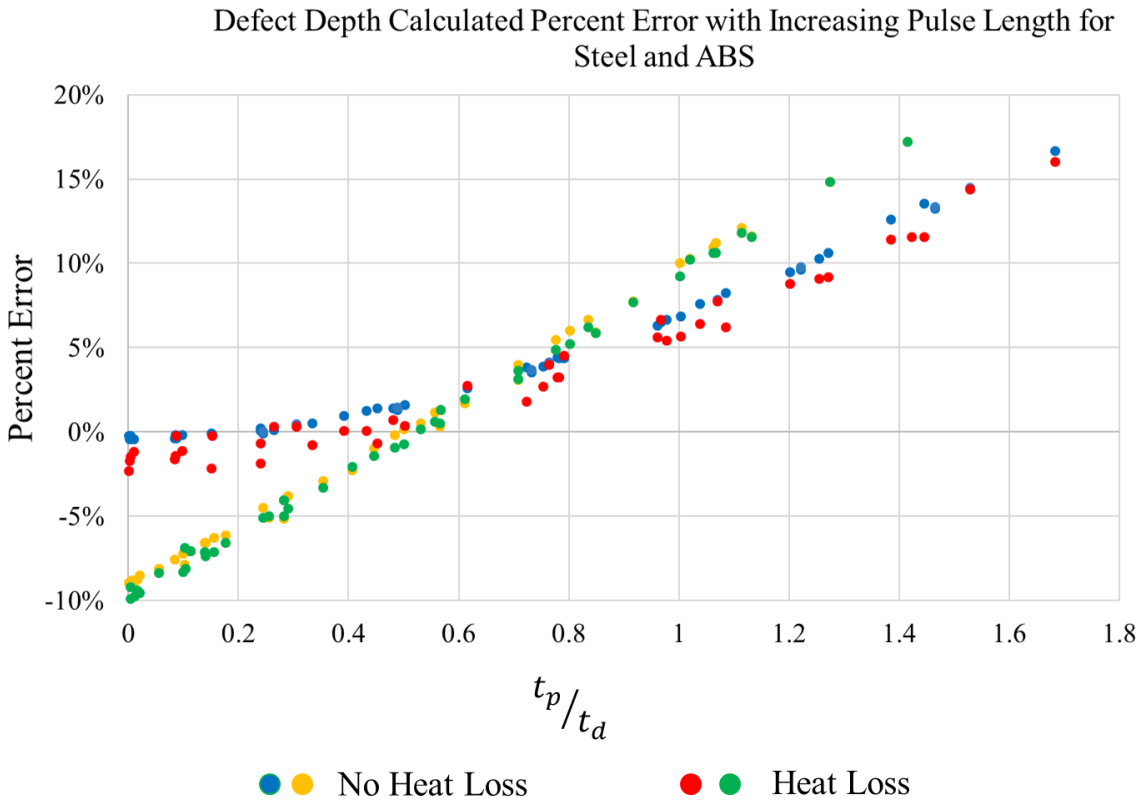

Figure 3.7 Defect depth calculation using the Peak slope temperature contrast method (blue and red) and the Log second derivative method (gold and green)

method used. The reason the log second derivative calculated depths show a linear trend whereas the peak slope contrast method shows a parabolic is because the peak times for the log method is found in the log scale. In the log scale, half of the pulse length, (ln(x) – ln(x/2)), is the same value (ln(2)) whether the pulse is 2ms or 500ms.

Figure 3.7 shows that for any given defect depth, the pulse length cannot exceed approximately 80% of the actual peak slope contrast time for that defect to stay within 5% error for defect depth calculation. For example, ABS with a 0.5mm sub-surface defect, has a peak slope contrast time of 577ms. Thus, the maximum pulse length to accurately calculate this defect within 5% error is approximately 462ms. Because of the varying thermal properties of different

materials, this maximum pulse length will vary as well. Table 3.3 shows for a given set of defect depths the maximum pulse length to obtain accurate defect detection within 5% error.

Table 3.3 Predicted maximum pulse lengths varying materials and defect depths

Defect Depth (mm)	ABS		316 L grade SS		PLA		Copper	
	Log Method	Peak Slope	Log Method	Peak Slope	Log Method	Peak Slope	Log Method	Peak Slope
0.3	0.144s	0.166s	0.0057s	0.0065s	0.413s	0.478s	0.0002s	0.0002s
0.5	0.399s	0.462s	0.0157s	0.0182s	1.15s	1.33s	0.0006s	0.0007s
1.0	1.6s	1.85s	0.0628s	0.0728s	4.58s	5.31s	0.0023s	0.0026s
2.0	6.38s	7.40s	0.251s	0.291s	18.33s	21.24s	0.009s	0.0105s

The standard pulse length for PT is 2-10ms, for copper this would mean the shallowest defect that could be quantified would be 1mm. Yet for PLA, even at 0.3mm the max peak using the log second derivative method is 412ms.

The ability to characterize the maximum allowable pulse length for accurate defect detection is a crucial benefit in analyzing a specific part. For the FDM process for example, the two most common materials used are PLA and ABS. Yet for defect detection, if the current experimental setup is set to pulse the maximum pulse lengths for ABS, the temperature contrast might not be sufficient to differentiate from the noise if the material was switched to PLA. Thus, the pulse times would need to be modified. Modifying the pulse length based on the material being tested is very beneficial for signal to noise ratio and will be further discussed in the next section.

3.4.4 Energy Input Effect on Signal to Noise

The amount of energy that is projected onto the part to thermally excite the surface is critical in getting accurate results. The smaller the signal the more the noise begins to overtake

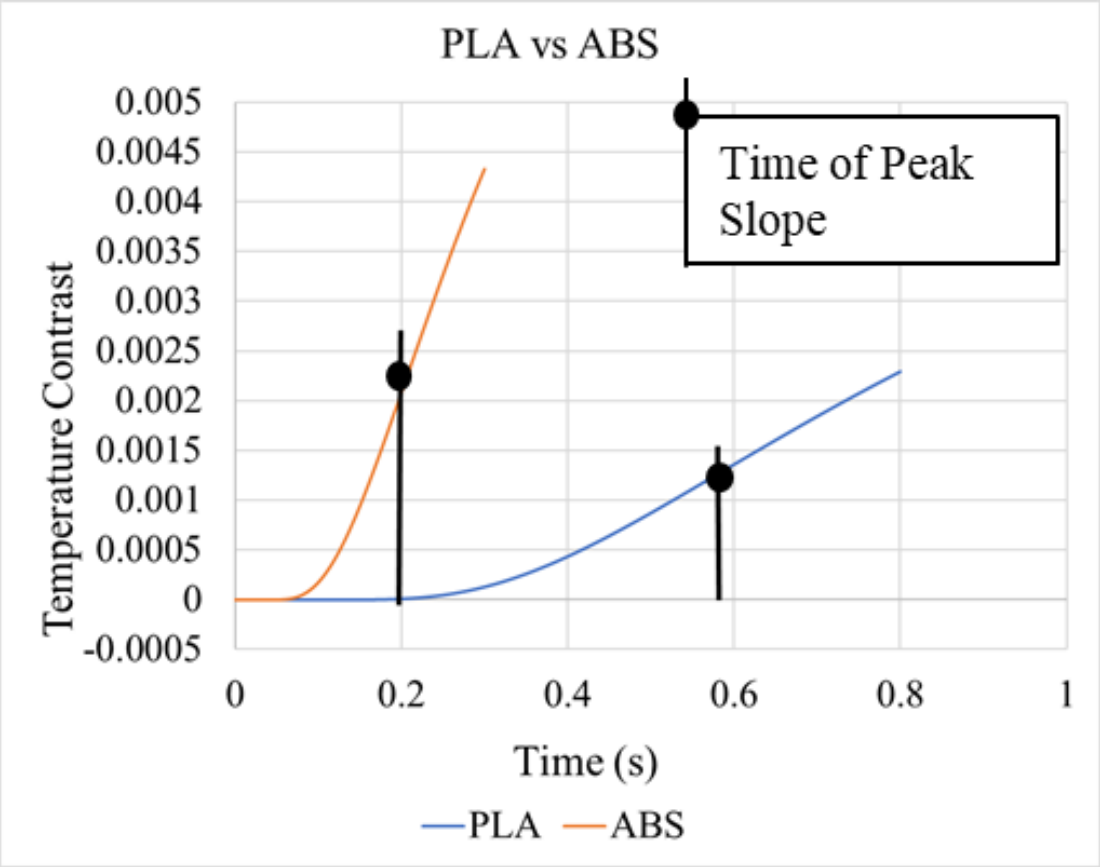

Figure 3.8 Temperature contrast comparison after 4000W pulsed 2ms thermal excitation for PLA and ABS

the desired data. Reviewing the case of PLA versus ABS, two materials most commonly used for FDM printing, the thermal properties are significantly different. As can be seen in Figure 3.8, at 4000W power and a 2ms pulse the thermal contrast at the point of peak slope for ABS is 68% larger than that for PLA. In the simulation data, this effect is not significant as there is no noise, however, experimentally the larger temperature contrast proves to be very significant in getting accurate results. It should be noted as well that from a practical standpoint, neither of these temperature contrasts would be distinguishable from noise in a practical case. Thus, a longer pulse or larger energy input would be required to determine defect depth.

With the same FDM printed ABS part used in Chapter 2, three pulse lengths were used to find the temperature contrast of the 1.2mm defect for defect detection. The three pulse lengths

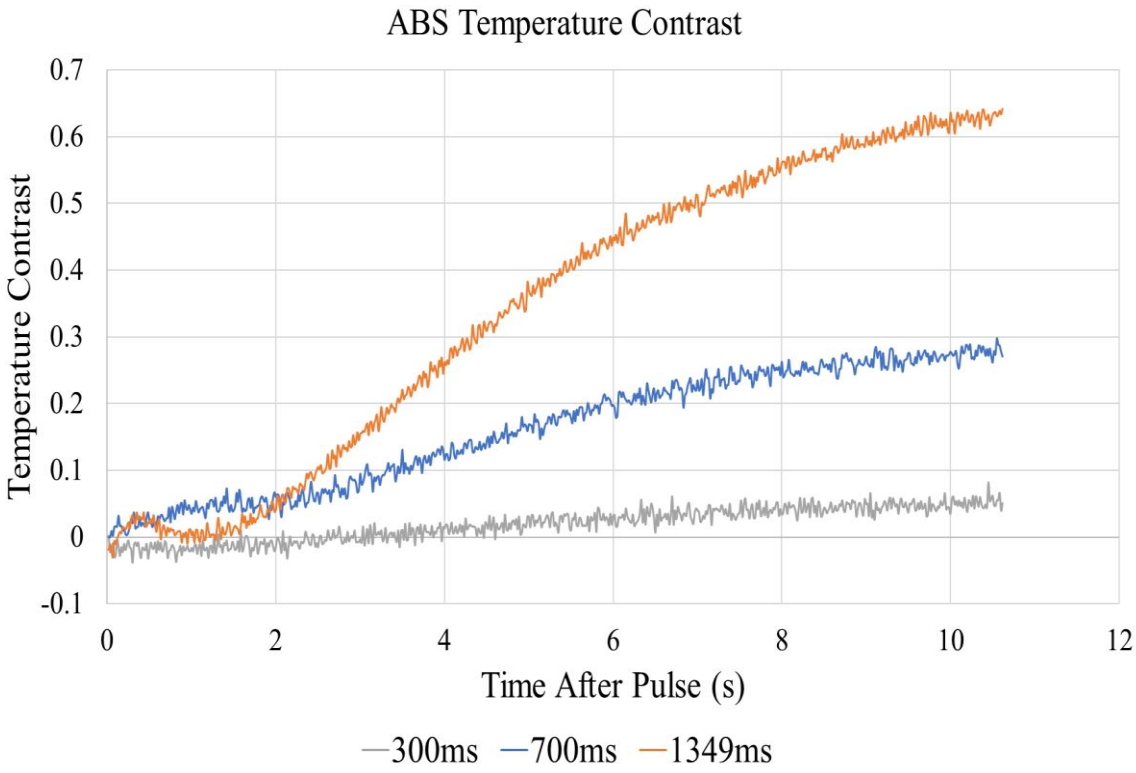

Figure 3.9 Temperature contrast comparison between three different pulse lengths for a 1.2mm sub-surface defect in FDM printed ABS

were 300ms, 700ms, and 1349ms. Figure 3.9 shows the temperature contrast produced by the 1.2mm defect from all three pulses. The temperature contrast results were calculated based on an average temperature of the defective region (8x8mm) and the average temperature of the same area for a sound region closest to the defect. As the pulse length increases the signal to noise ratio continues to increase as well. The noise from all three measurements is the same at approximately 0.007 ˚C, however the temperature contrast from the 1349ms pulse is significantly larger compared to that of the 300ms. For a clearer understanding of the effect this has on the accuracy, Figure 3.10 shows the actual signal to noise comparison between the 300 and 1349ms pulse. With the 300ms pulse, an increase in the temperature between the sound and defective region can be seen, however, the overall signal to noise ratio is only 9. Whereas with the 1349ms pulse the signal to noise ratio is 87, over an 850% increase.

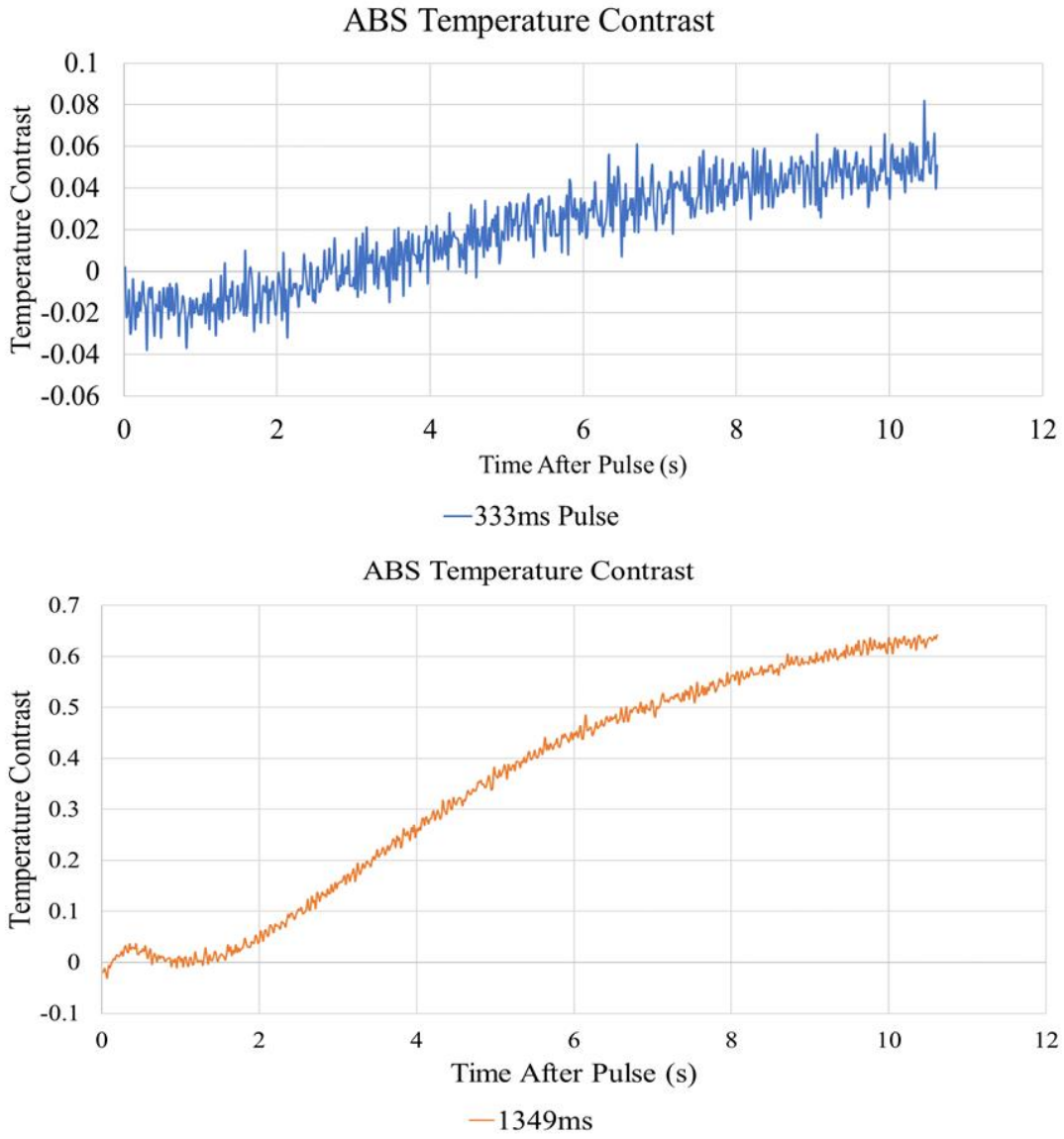

Figure 3.10 Signal to noise comparison between 300ms pulse and 1349ms pulse for a 1.2mm defect in FDM printed ABS part

It is important to note that both these measurements were taken with longer pulses. In fact, even the 300ms pulse with a signal to noise ratio of 9, inputs 150 times more energy into the part than a typical case of a 2ms pulse with the same overall power. To achieve the same temperature contrast with a 2ms pulse as a 320ms pulse for a 0.3mm defect in ABS, the overall power would have to be 200,000W, as seen in Figure 3.11. Figure 3.11 shows the surface temperature decay curve produced by different powers of heat required to generate the same

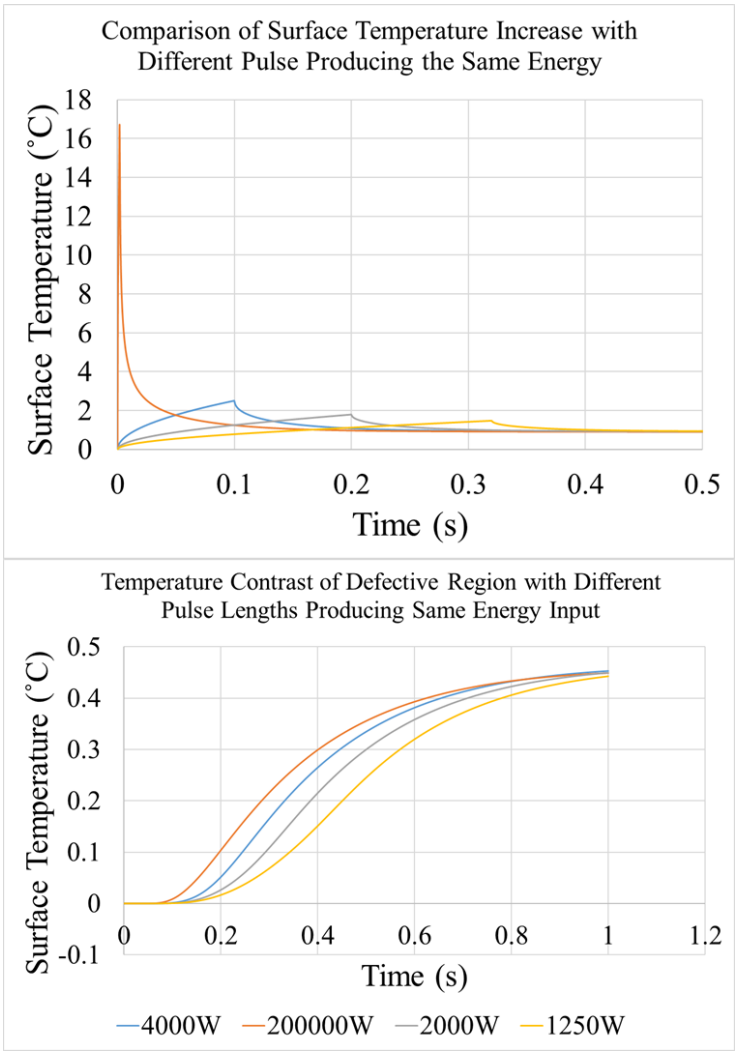

Figure 3.11 Comparison of the surface temperature increase with varying pulse lengths producing the same amount of energy and the temperature contrast produced by a 0.3mm defect in ABS

thermal contrast from a 0.3mm defect in ABS. Four different pulse lengths were compared with their respective required heat power inputs to produce a desired energy input of 400J. With the longer pulses minimal surface temperature increaser is experienced, however the thermal contrast of the 0.3mm defect region to the sound area reaches the same level as a 2ms pulse. It can also be noted for the case of the 2ms pulse, this level of temperature increase could introduce more error due to possible phase changes and significantly added radiative heat losses.

Furthermore, knowing the value of the noise and based on the simulation data seen in Figure 3.8, the temperature contrast for a 0.3mm defect would be indistinguishable if done experimentally. This becomes even more important with the deeper defects such as the 1.2mm studied in Chapter 2, which can be detected with the long but would be lost in the noise of a shorter pulse at the same power.

3.5 Conclusion

By using a longer pulse, accurate defect detection becomes possible with various pulse lengths. Thus, allowing for the capability of increasing the pulse length to increase the energy input into the part. By utilizing the maximum allowable pulse length for accurate defect detection, the energy input can be significantly increased creating larger thermal contrasts on the surface. This in turn minimizes the possible error from the signal to noise ratio. It also allows for defect depth measurements of a much wider range of defect depths as well as a much wider range of parts with various thermal properties. There is also another important benefit of longer pulse analysis, and that is the use of the infrared reflections emitted off the part during the pulse. Depending on the surface characteristics such as defects, the reflections will vary into the IR camera off the surface. An in-depth analysis and discussion will continue in the next chapter.

CHAPTER 4: REFLECTIVE THERMOGRAPHY FROM LONGER PULSE TESTING

Defect detection and quantification is a vital part of industrial manufacturing. Online process monitoring, and defect detection is especially beneficial as it allows for possible in process defect repair. This chapter will discuss the use of a Nondestructive evaluation (NDE) method known as Pulsed Thermography (PT) to detect surface characteristics and defects on a 3D printed part made from a thermoplastic, ABS. In PT, the surface is heated, and the surface temperature is monitored over time. In particular, this chapter examines the use of reflected infrared light to reveal surface characteristics and defects. Due to the process speed and surface sensitivity, PT could be integrated into a 3D printing system to permit layer by layer inspection without drastically increasing overall build times. Integration would allow for online process monitoring of each layer, therefore adding the ability to log defects and make printing corrections in-situ. This additional process control can ultimately minimize the number of defects within a final structure and improve the quality and reliability of printed parts.

4.1 Introduction

In Rapid Prototyping, the production of the final geometry has been the main topic of interest. Originally used as a quick way to build prototypes, the growth of technology has allowed for tighter tolerances producing more precise components, leading to the capability of 3D printed parts meeting the design requirements and being used as final products. This has opened the door to the use of these processes for direct manufacturing as represented in the new terminology of Additive Manufacturing (AM). However, for AM to continue to grow, process monitoring, process control, and quality assessment methods that are tailored for these processes

are needed in order to achieve higher quality levels while maintaining the strengths of AM in geometric complexity and low volume production`. Processes such as the ability to monitor polymer welding zone temperatures enabling a better understanding and control of weld strength in a component [6].

The goal of this chapter is to investigate the suitability of layer-by-layer surface quality assessment of Fused Deposition Modeling (FDM) components. FDM is an extrusion-based 3D printing process where a molten material such as thermoplastics, are liquified in a chamber and then extruded through a nozzle [2]. The extruded material is laid on a horizontal plane in paths commonly called "roads." The roads for a single layer create a layer. After each layer is sequentially laid in the vertical direction, a 3D part is formed [2]. There have been extensive studies on the input parameters that control the build quality in FDM, such as the machine parameters and specification, properties of the material and geometry of the product which all affect the quality of the 3D printed part [39]. Galantucci et al [40] showed that the layer height and the filament width are important parameters for the surface roughness of a 3D printed FDM part. These parameters control the inputs that go into building the part, however, there are uncontrolled variables that can affect the build of the part as well.

Uncontrolled variables are inevitably part of any manufacturing environment. In the case of FDM, uneven temperatures within the part can create cracks, holes or delamination. Foreign debris within the stock material can be printed into the product. Variation in extruder nozzle speed laying the filament and filament extrusion diameter can create an under extrusion between filaments. As the part continues to print, these defects will be covered—potentially hiding any issue that may lead to failure after the product is completely built. Due to the unique nature of AM to print low volume unique products, destructive tests would not be cost-effective. And there

would be no guarantee that the next part would not have the same or different defect in it as well. Thus, methods for nondestructive testing and online process monitoring are needed to assure product quality. This chapter is looking at the ability of pulsed thermography to detect some common surface features.

4.2 Infrared Reflective Thermography

Pulsed Thermography (PT) is a process where the surface of a part is heated via a pulse of energy and then the surface temperature is monitored over time with an infrared (IR) camera. The equation of this surface temperature distribution over time with an instantaneous pulse was determined by Parker et al [27]. Where there is a defect within the part, a hotspot will appear on the surface after a certain period. This is because where there is a defect the 1D conduction heat transfer within the part breaks down and the process of 3D conduction begins around the defect. This in turn slows down the conduction of heat above the defect producing a hotspot on the surface in the shape of the defect as 1D conduction continues everywhere without a defect. Once a defect is identified with PT you can quantify the depth of the defect as well as the size based on the time it takes for the hotspot to appear on the surface. Some methods for quantifying defect depth include peak slop derivative time first introduced by Ringermacher et al [28], log second derivative proposed by Shephard et al [29], least-squares fitting method first proposed by Sun et al [23]. The focus of these methods for defect detection and quantification is after the part is built or multiple layers have been laid. In contrast to these prior works focused on subsurface defects, this chapter focuses on a preliminary investigation of an online integration method that can monitor the surface of a part while it is being printed allowing for possible repair if necessary.

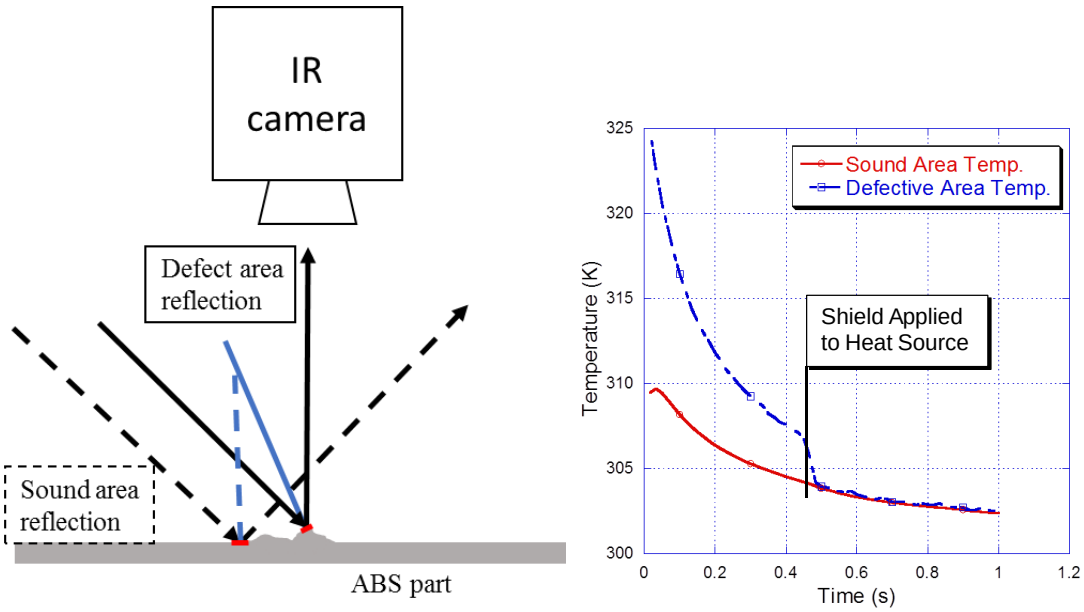

Figure 4.1 (a) Illustration of specular reflections off a sound area compared to specular reflections from a surface defect showing why surface defect reflections show up as hotspots in the IR image. (b) Comparison between the surface temperature of sound areas to that of a defective area during and after pulse heating of the ABS part.

Distinguishing surface defects with an IR camera requires the defects to be heated differently than the surrounding sound (defect free) areas of the part. The surface roughness of 3D printed parts however, are very small compared to the distance of the heat source. Therefore, even large surface defects have uniform temperature with the surrounding area. However, when using a modified PT method with significant illumination in the infrared wavelengths measured by the camera and imaging during the illumination period, it has been found that while the bulb is heating the part, the radiant heat can reflect off surface features into the IR camera to create an immediate hotspot on the surface. The highlighted defects are dependent on the relative orientation of the source, defect edges, and camera.

There are two types of reflections that can occur from a surface from the radiant heat; specular and diffuse. Specular reflections occur when the angle of the incoming radiant heat source reflects off the face of the part at the same angle of incidence and follows Fresnel

equations [41]. Diffuse reflections occur not on the same angle of incidence but in a spherical angular distribution from the plane of interference following Lambert's cosine law [42]. Because no surface is perfectly smooth there will always be diffuse reflections occurring from the surface of a part. The diffuse reflections have a lower intensity than the specular reflections and can be ignored for the analysis of surface defect reflections seen in the IR image. This can be seen in Figure 4.1 as temperatures in sound areas produce only diffuse reflections in the IR image and show no significant drop in temperature once the radiant heat source is shielded from the part. Defective areas in comparison, producing specular reflections into the IR image, show a significant temperature difference until a shutter is placed in front of the heat source after the pulse blocking all radiant heat.

Immediately following the blocking of the radiant heat source, the defective area temperature drops down to the surrounding sound areas. Figure 4.2(a) shows the IR image of the ABS 25x25x8mm part during pulse heating of the part. The 3D printed part was pulse heated for 400ms and after the completion of the pulse shutters were placed in front of the heat source to block any radiant heat emitting form the bulbs during cooling as seen in Figure 4.2(b). The area

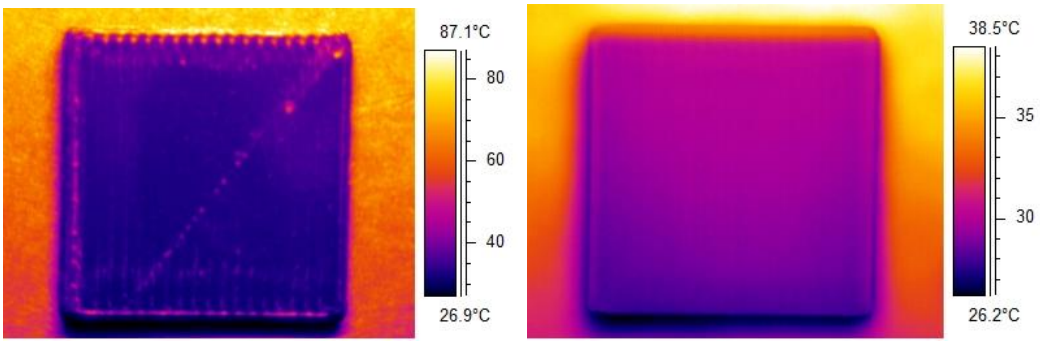

Figure 4.2 Comparison of an ABS part after being pulse heated. Image (a) shows the surface reflections and emission of the part during the pulse and image (b) shows the surface temperature emission after the pulse has completed heating the part and the source shutter is closed to eliminate reflected IR light.

of the appearing hotspots is not physically hotter after the 400ms pulse than the surrounding area as shown in Figure 4.1 but because it has a different surface profile than the surrounding area it allows for a specular reflection of the radiant heat to be directed into the IR camera. Therefore, they are reflective spots and by using the PT method with a longer pulse a picture of the surface profile can be visually analyzed.

4.3 Experimental Setup

For the analysis of the surface defects on an ABS 3D printed part in Figure 4.3(a), Figure 4.3(b) shows the setup and two 110V 500-watt Halogen lamps were used. The part was a 25mm by 25mm and 8mm thick square made of thermoplastic, ABS, and printed on a MakerFarm 8" Prusa I3v printer. The nozzle diameter was 0.4mm and a layer height of 0.2mm was selected. The part was rotated 90 degrees so that the heat source was perpendicular and parallel to the filament. The camera was set at an angle of 90 degrees from the surface to minimize any specular reflections from a sound area and the bulb was set at 45 degrees from the surface of the

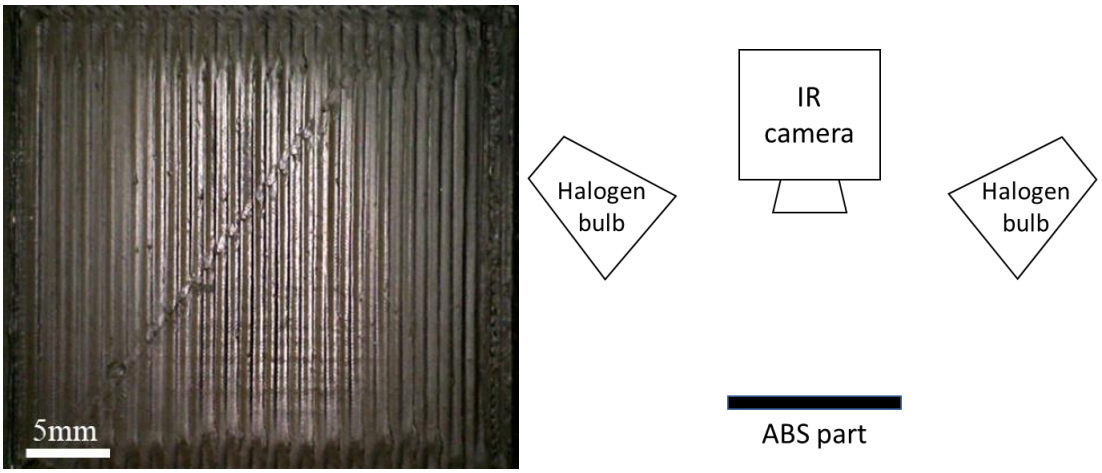

Figure 4.3 (a) ABS printed Makerfarm part being analyzed for surface defects and (b) Illustration of the setup for the analysis of the surface reflections from the PT method.

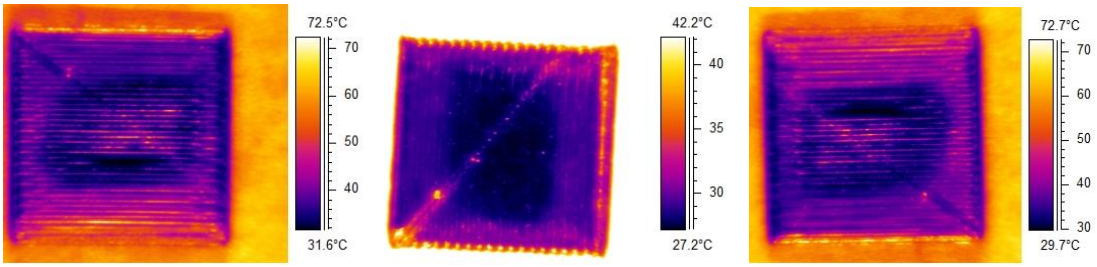

Figure 4.4 (a) IR image of a 3D printed part at zero degrees starting point roads perpendicular to the heat source. (b) IR image of part at 90 degrees, roads are parallel with heat source. (c) IR image of part at 180 degrees rotation with roads perpendicular in opposite direction as starting point.

part. The halogen bulbs were pulsed for 400 milliseconds and then shut off to allow time for analysis of the surface reflections. After completion of the pulse heating, shutters were rotated in front of the halogen bulbs to block all radiant heat emitted by the bulbs during cooling eliminating the reflections seen during the pulse.

4.4 Results and Discussion

With a specular reflection, the reflected angle always equals the incident angle [11]. Because of this the IR camera cannot be setup at the same angle as the heat source to the component. That way the IR camera does not pick up the specular reflections from flat planar surfaces. For the camera to pick up a specular reflection of radiant heat, the surface face must create a plane of incidence between the heat source and the IR camera that allows the reflected heat to be seen. This includes defects and road edges, as well as the faces of the roads. Figure 4.4 shows the effect of rotating part 180 degrees, allowing the heat source to reflect off the surface and the roads at difference angles. When the source of the heat is perpendicular to the road direction, the radiant heat reflects off the curved faces of each road. This creates more reflective lines on the surface, masking smaller defects. It does, however, give an approximate representation of the road profiles and the relation to adjacent roads. Depending on the surface profile of a road, it will reflect differently into the IR camera. If the road has a more convex

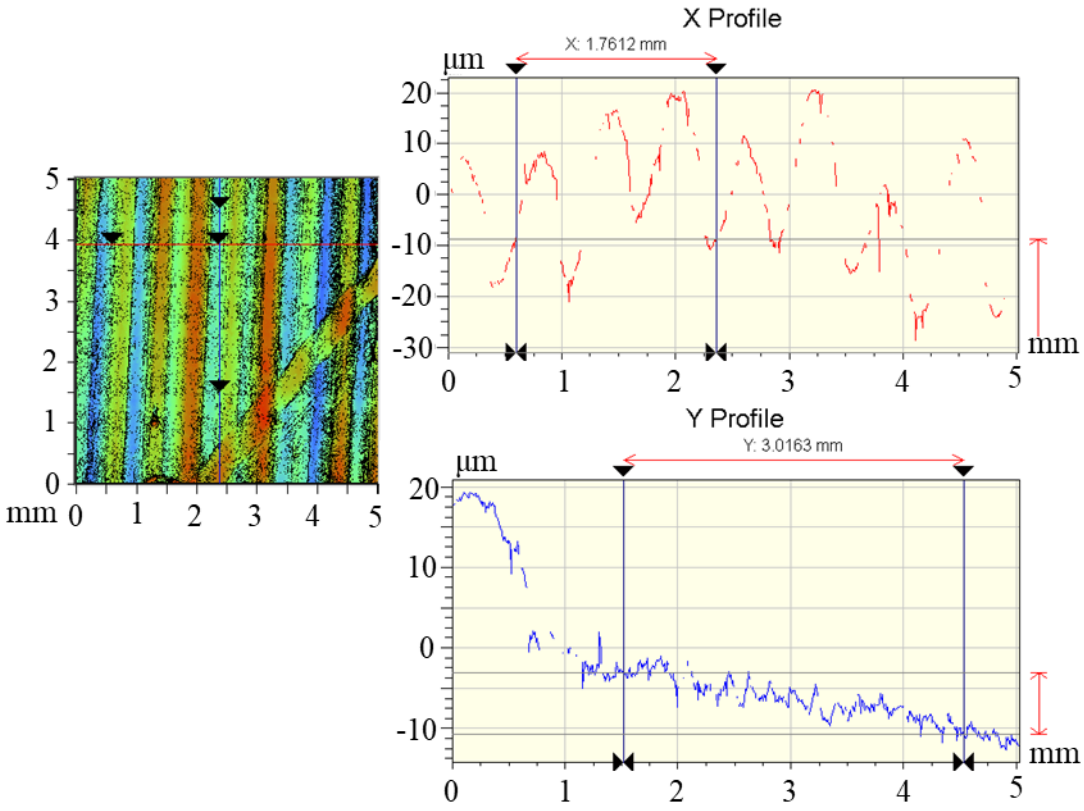

Figure 4.5 Optical profilometry data of a portion of the surface of the 3D printed part comparing surface roughness parallel with the roads and perpendicular with the roads.

curved profile it increases the possibility of creating an angle of incidence into the IR camera.

Figure 4.5 shows optical profilometry data comparing the surface roughness in microns between traveling perpendicular to the road direction and parallel. The road heights vary approximately 20 microns and have a curved profile, correlating with the reflective lines that appear in the IR image when the heat source is perpendicular to the roads. When the heat source is parallel to the filament direction most of the road reflections will not be seen by the IR camera unless there is a defect or if a portion of the surface of the part is not flat. The profilometry correlates to this theory as the roughness along the roads is less than 5 microns with no significantly curved profile thus producing only diffuse reflections into the IR camera.

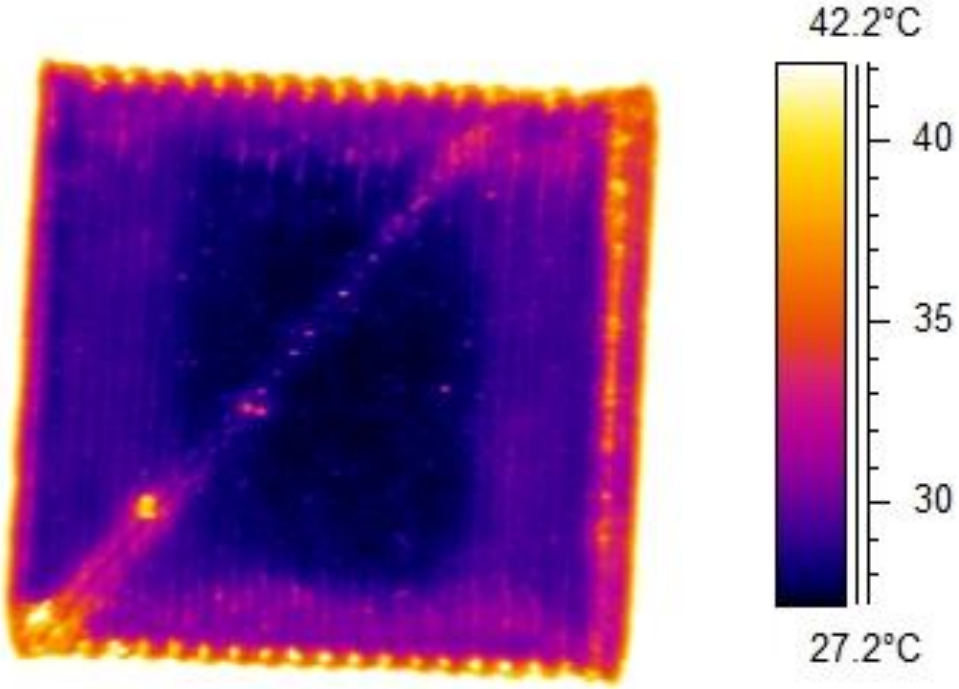

Figure 4.6 Shows the thermal image with reflections during the initial pulse of the ABS part.

4.4.1 Holes and High Spot Defects

Thermal images were analyzed during the flash as seen in Figure 4.6 with the road direction parallel to the heat source. There are many surface reflections that appear on the surface during the pulse. Most of them following a diagonal line from the bottom corner of the part going up to the top right of the part. This diagonal line appears to be from the extruder tip being too close to the surface of the part when it changes position from that spot pushing the edges of the filament creating a line of ABS. There are also a few small reflective spots scattered throughout the surface of the part. The biggest reflection is in the lower left portion of the part and near the diagonal line.

When analyzed using a magnifying camera the reflective zone is a surface hole defect approximately 1mm in diameter as well as noticeable holes forming a line perpendicular to the

filament direction measuring approximately 1.5mm as seen in Figure 4.7(a). Figure 4.7(b) is a focused view of the area with both defects measured in Figure 4.7(a) and showing defects that can be seen in the IR reflected image as small as 181μm. The size of the defect that can be seen from the reflected radiation into the IR camera depends on the overall quality of the part surface. Figure 4.8 Shows a comparison between a zoomed in IR image of a portion of the 3D printed

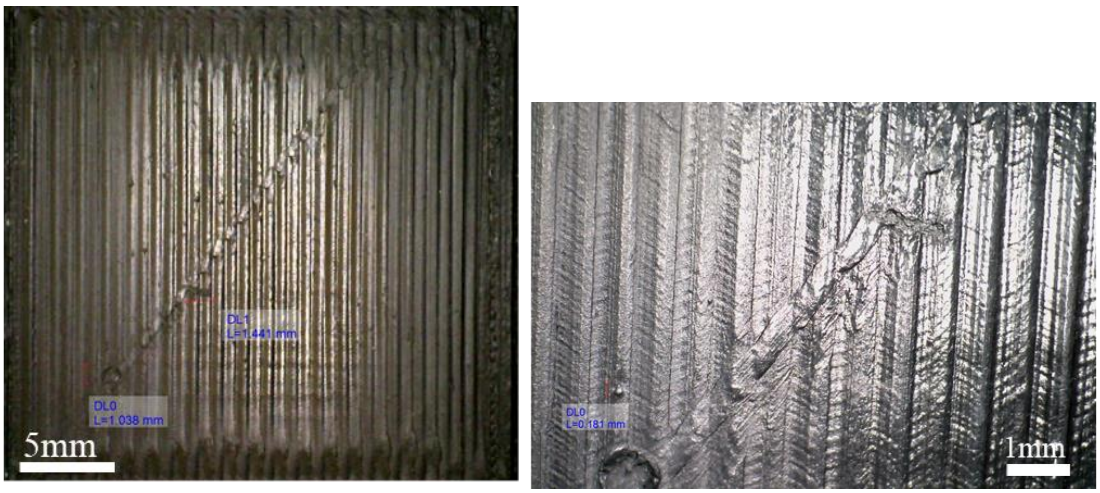

Figure 4.7 (a) Full size image of the ABS printed part with measured surface defects. (b) Magnified 44x picture of a portion of the ABS printed part with smaller measured defect size for comparison.

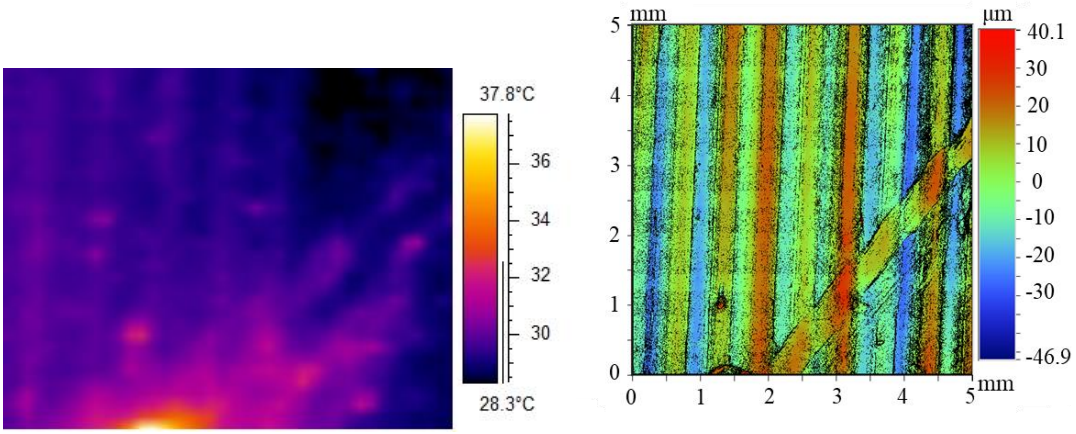

Figure 4.8 (a) Zoomed in IR image of the 3D printed part matching the dimensions of (b) the optical profilometry data of the surface of the 3D printed part.

part compared to the optical profilometry data for that section. The profilometry image and the IR image are similar showing defects microns in diameter.

4.4.2 Under Extrusion Defects

The focus so far of reflective lines has been on hole or high spot defects as well as the effect of road direction to the heat source. There is another defect that can occur during printing and that is under extrusion. Under extrusion occurs when the filament is stretched from the nozzle producing a road diameter that is smaller than the surrounding roads thus leaving a gap between roads. The 3D printed part that has been analyzed for hole defects did not have any under extrusions between the roads, therefore, we analyzed a part produced on a 3Dn-Tabletop nScrypt system. It was printed with a nozzle diameter of 0.2mm and a layer height of 0.1mm.

The ABS part was thermally pulsed with the same experimental setup as the other part and Figure 4.9 shows the IR image of the new 3D printed part. The part was pulsed with the heat

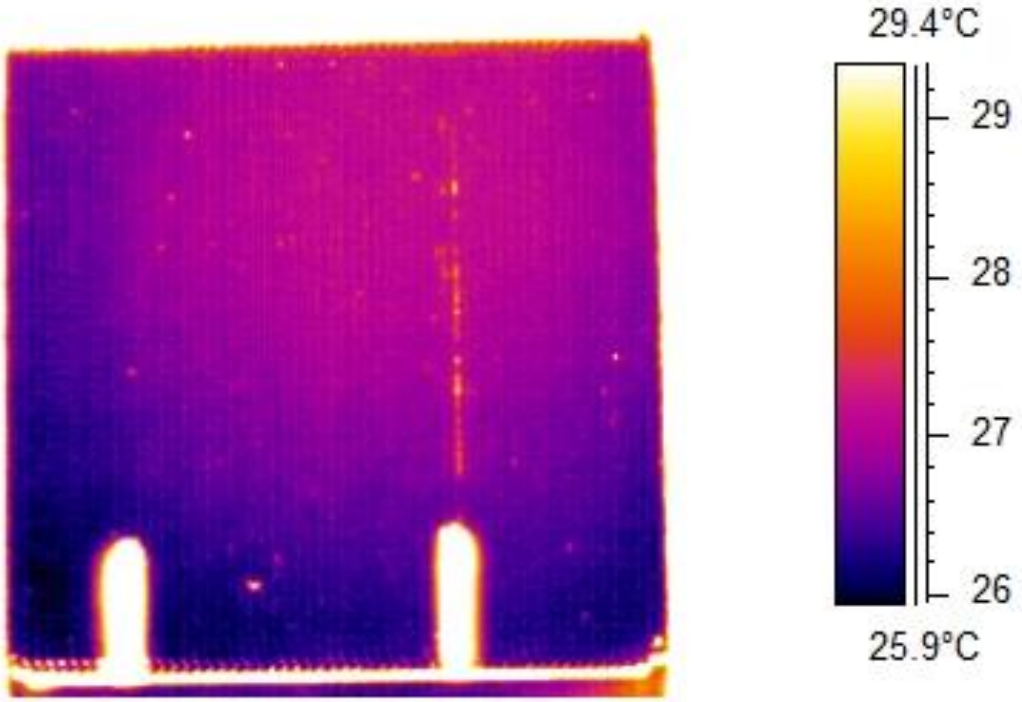

Figure 4.9 IR image of nScrypt 3D printed part

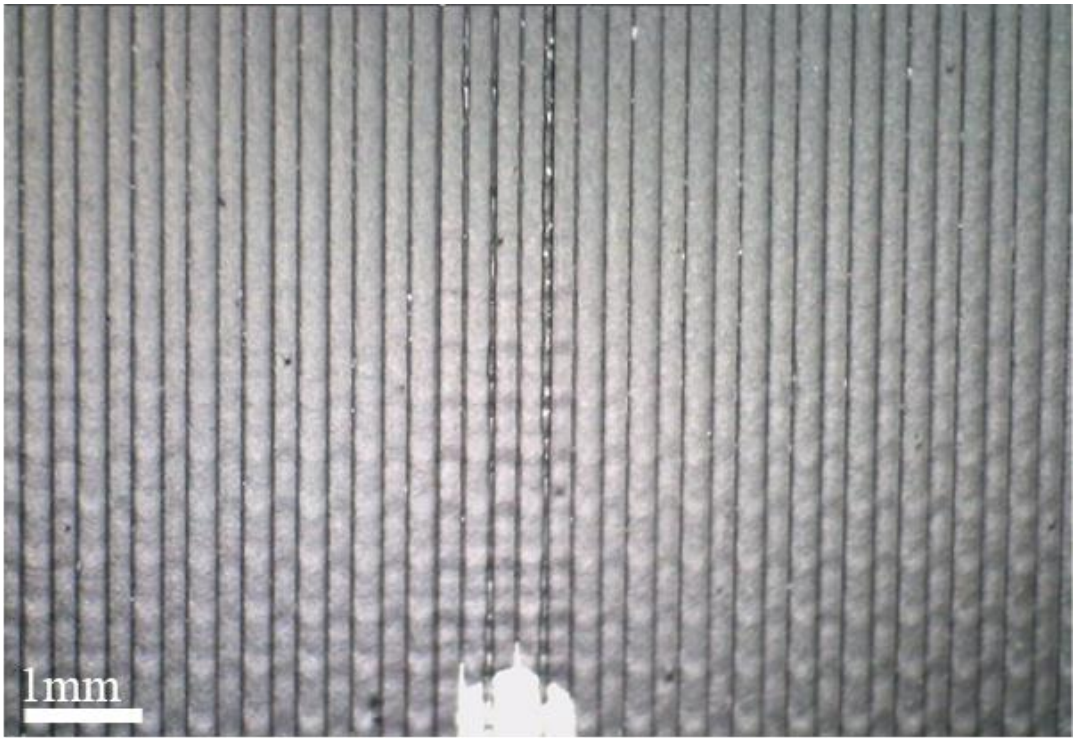

Figure 4.10 Optical image of the nScrypt 3D printed part showing an under extrusion between roads exposing the previous layer.

source parallel with the roads and in the IR image a clear vertical reflective line is visible as well as other reflective spots throughout the surface. The two larger hotspots in the bottom of the part are marker lines and not actual defects from printing of the part.

The bright spots related to the under extrusion are reflections from the previous laid layer. As noted earlier when the road direction is perpendicular to the heat source the curved profile of the road's surface will reflect the radiant heat into the IR image. Since there is an under extrusion, this leaves the previous layer's roads exposed allowing for them to reflect the radiant heat exposing the under extrusion. Figure 4.10 shows a magnified optical image of the part containing the under extrusion. As you can see the roads form the previous layer are visible and capable of reflecting radiant heat into the IR camera. There is also a smaller under extrusion two

roads over to the left appearing in the optical image, but it is not as extreme an under extrusion with portion of the adjacent roads connecting.

4.5 Conclusion

Using Pulsed Thermography to be able to identify defects within a part after the product has been built or multiple layers have been laid is a step in the right direction for quality control in the field of AM. For online integration of a monitoring system being able to use this new form of reflective thermography from a longer pulse time to allow the radiant heat to reflect from the heat source to the IR camera takes the capability for quality control a step further. Defects such as indentations, drag marks from the extruder nozzle, and under extrusions all can be seen from the reflections they produce in comparison to the sound areas surrounding them. When the heat source is perpendicular to the road direction an approximation of the road profiles can be made as well as the overall roughness of the part.

Future work could look at quantitative analysis methods between the surface roughness and the reflection from the roads in the IR image. Currently, the profilometry data is only being used as visual comparison analysis. It is important to note that the sensitivity of this method as a detection method of defects depends on the overall quality of the surface; the more larger defects the part has on the surface the less sensitive the inspection is of smaller defects. Coupling the capability to monitor the surface profile with the ability for defect detection and quantification in sublayers using the PT method with a longer pulse creates multiple layers of online quality inspection.

For effective implementation of both methods, the thermal source would need to be parallel with the road direction during the build. Therefore, for the reflective thermography, either multiple bulbs surrounding the part with individual control or the ability for the thermal

source to move would be the required setup. For analysis, both could be accomplished. The reflective thermography analyzed during the pulse simultaneously and then sub-surface defects after the pulse with allowable time for the peak contrast slopes to occur. Ultimately this will greatly minimize the chances for defects to arise in final products after completion of the build.

CHAPTER 5: THERMAL PROPERTY ANALYSIS OF BINDER JETTED PARTS

It was shown in Chapter 2, that the quantification methods of Pulse Thermography (PT) are still applicable and effective in determining defect depth in FDM printed thermoplastics when using a longer pulse for thermal excitation. In fact, a wide range of pulse lengths depending on the material properties can be used for accurate defect detection as shown in Chapter 3. This is vital for being able to provide enough energy input to get the necessary thermal contrast and overcome thermal losses for materials with very low thermal diffusivities. Another benefit of the longer pulse discussed in Chapter 4 is the ability to analyze radiant reflections for surface characterization and defect detection of printed parts. Thus, with known approximate thermal properties, defects can be detected.

In Chapter 5, the latter aspect of PT will be analyzed for powder processes with longer pulses, specifically Binder Jetting. Binder jetting creates parts from powder and the quality of the parts is dependent on the packing of the powder. Thermal diffusivity will be measured using PT to see the effect of density, binder presence, and curing temperature of green parts to see if there is a strong correlation between these important variables and the thermal diffusivity that could be used for online process monitoring.

5.1 Introduction

With Additive Manufacturing (AM) continuing to grow, a plethora of products are being considered and studied for production [43]. The reason AM is so attractive is, as previously stated, its exceptional ability to produce low-volume and complex shape parts. As more

manufacturers look to AM for optimized building methods of complex products, more and more research is being conducted to understand the properties of AM parts.

Specifically, with the Binder Jetting (BJ) explained in the Chapter 1, there are many variables that can alter both the mechanical and thermal properties of a product. The powder size distribution can affect overall density of the part [44,45]. Which can have a major impact on green part strength, sintering shrinkage and thermal properties. The layer thickness and part orientation [46]. Because the binder is dropped from an inkjet head onto the part, the printing speed has mechanical effects on the final part [47]. Binder saturation levels can affect mechanical strength, thermal diffusivity and even dimensional accuracy depending on the saturation levels [48-50].

The focus of most research among these printing parameters however, have mainly been on the improvement of mechanical properties and density [51-55]. There has been little research on the thermal affects these parameters have on BJ parts, specifically binder saturation and curing temperatures. The ability to monitor and understand thermal properties, specifically thermal diffusivity, during the build could help in improving process parameters such as the pre-binder heating process (which is done to help cure some of the binder before next layer of powder is laid). Another important aspect is once an approximate thermal diffusivity is known based on specific parameters, then future parts with the same parameters can be monitored to locate defects and quantify their depth. Thus, the focus of this chapter is to provide a preliminary understanding of the capabilities of using the longer pulse method of PT to compare how the curing temperature and density affect the thermal diffusivity of BJ parts and raw, 30μm diameter 420 SS, powder.

5.2 Calculation of Thermal Diffusivity With PT

Using the method of PT, defects can be quantified based on the time response of the surface temperature to a specific depth. The capability of this however, is limited to the knowledge of the thermal diffusivity of the material being tested. Because the binder saturation percentage and density can vary with different parameters in BJ, the thermal diffusivity of the part being built is an unknown variable. However, if there is a known "defect" depth, the method of PT can then be used to determine the thermal diffusivity. This can be done by rearranging the defect depth quantification equations 2 and 4 discussed in Chapter 2 to give thermal diffusivity:

$$\alpha = \frac{3.64L^2}{t_s\pi^2} \tag{9}$$

$$\alpha = \frac{L^2}{t_2\pi} \tag{10}$$

with L being the known "defect" depth, t_s the peak slop contrast time in equation 8 and t_2 the log second derivative peak slop time in equation 9. Either method can be used to determine the defect depth, however, it is important to note that each equation is specific to the method it is defined for. For the purposes of this preliminary study, the peak temperature contrast method will be used for all the thermal diffusivity measurements. The reason for this was explained in Chapter 2 as a more refined model is needed to utilize the log second derivative method.

5.3 Experimental Setup

5.3.1 Density Measurement of Raw Powder

To measure and compare the difference between apparent and tapped density of 30μm 420 SS powder, a fixture was made with a hollowed cylinder in the center to capture the powder

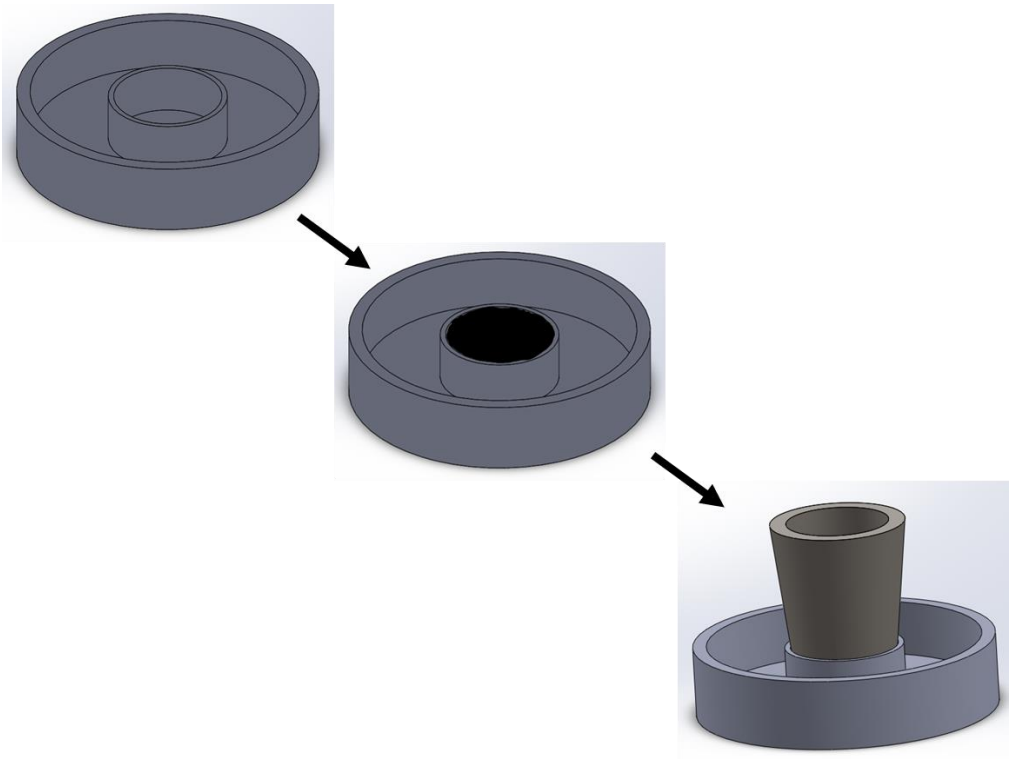

Figure 5.1 Schematic representation of the measurement process for density of raw powder

as seen in Figure 5.1. The cylinder in the center has an inner diameter of 19.5mm and a height of 9mm. For the apparent density, the powder was poured into the container until it filled the top of the cylinder and then a blade was used level off the surface. A metal tube was then inserted into the cylinder to separate the powder used for density measurement form the extra powder that spilled over during filling. The powder inside the center region was weighted with an Adventurer SL AS214 scale with a resolution of 0.0001g. To calculate the powder density, the powder volume was calculated from the cylinder diameter and height.

For the tapped density, the same process was used for the weight of the powder. However, as the powder was poured into the fixture, the fixture was vibrated by hand, back and forth steadily allowing for the powder to settle. This is different than the proposed method of obtaining a tap density by tapping a cylinder 1000 to 3000 cycles at approximately 284 cycles

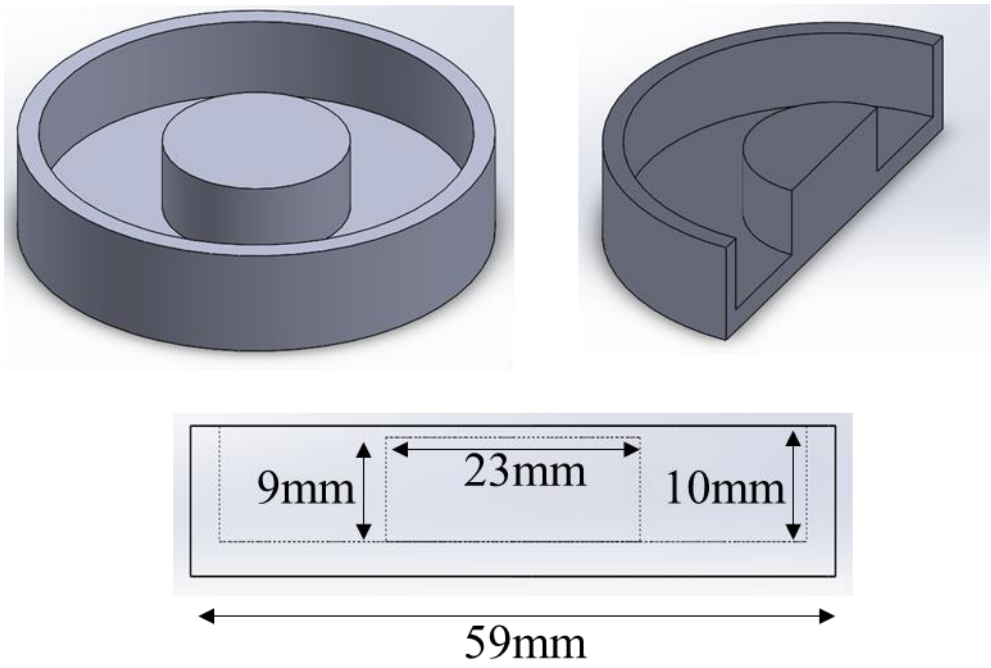

Figure 5.2 PLA fixture used to measure the thermal diffusivity of raw powder

per minute [56]. However, for the purposes of preliminary investigation on the affects density has on thermal diffusivity this vibrational method will suffice.

5.3.2 Thermal Diffusivity Measurement of Raw Powder

To determine the thermal diffusivity of a material using PT, there must be a known defect depth to slow down the heat conduction process and produce a thermal contrast on the surface. With raw powder however, this is especially difficult because normally, the defects that have been used were voids. For the case of raw powder, this defect is not possible as the powder would simply fill the void space as there is no mechanical structure to the powder. Therefore, to measure the thermal diffusivity, a fixture was made that could support the powder and simulate the defect as seen in Figure 5.2.

The fixture was FDM printed Polylactic acid (PLA), the other most common material printed with the FDM process next to ABS. The benefit of using PLA as the fixture (and known

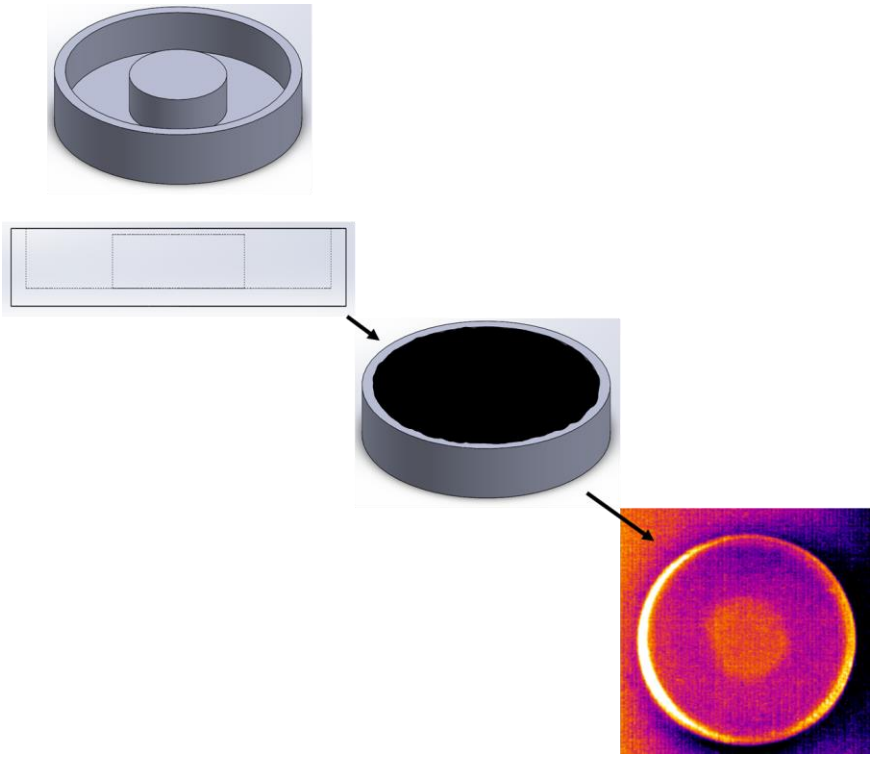

Figure 5.3 Schematic representation of thermal diffusivity measurement process

defect depth) is that the material has a very low thermal diffusivity of 5.556 x 10^{-8} (m^2 s^{-1}). The benefit of having a very small thermal diffusivity material as the fixture and known defect depth is that it increases the possibility of a thermal contrast after the pulse. If the thermal diffusivity of two materials are similar than the heat transfer rate doesn't slow down, and no thermal contrast is produced on the surface. Thus, the larger the difference between in thermal diffusivities between material and defect, the larger the thermal contrast.

For thermal diffusivity measurement, the same process is used to create the apparent and tapped density. However, this time the powder is leveled off at the top of the fixture as seen in Figure 5.3, creating the defect in the center. To maximize the thermal contrast even further and ensure no powder falls between the roads of the FDM printed part a piece of clear tape was placed over the defect. The thickness of the tape was 0.045mm therefore, for the thermal diffusivity calculations, 0.955mm was the actual defect used in equation 8.

5.3.3 Thermal Diffusivity Measurement of Binder Jet Parts

To understand the affect curing temperature has on the thermal diffusivity of a BJ green part, two parts made of 420SS with dimensions as seen in Figure 5.4 were built on an ExOne Innovent 3D printer. The same parameters were used for each part to ensure the only variable was the post process curing temperature. The parameters can be seen in Table 5.1.

Table 5.1 Build parameters for thermal diffusivity testing of Binder Jet parts

Drying Time (s)	12	
Emitter Output (%)	100	
Target Bed Temp. (˚C)	40	
Recoat Speed (mm/s)	90	
Oscillator Speed (rpm)	2200	
Roller Traverse Speed (mm/s)	5	
Roller Rotation Speed (rpm)	300	
Desired Saturation (%)	60	
Layer Thickness (μm)	100	
Curing Temperature (˚C)	165	185
Curing time (hours)	4	

The known 8x8mm defect depths of each part ranged from a depth of 0.5-1.0mm and each defect was used to calculate thermal diffusivity. Multiple defect depths were used to

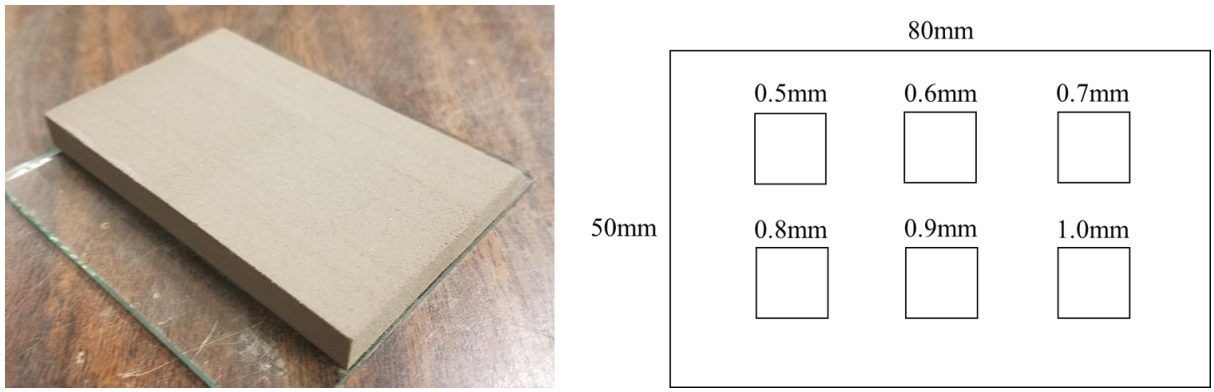

Figure 5.4 Binder Jet part to be used for thermal diffusivity testing of the material with different curing temperatures

understand if there was any effect on the calculated diffusivity with increased layers as each depth is separated by one-layer thickness. To ensure accurate calculated thermal diffusivities, the deeper defects (0.9-1.0mm) were used to calculate the thermal diffusivity first, than the maximum allowable pulse lengths were calculated for the rest of the defect depths. With the known maximum allowable pulse lengths for each depth, thermal diffusivities were calculated.

5.4 Raw Powder Results and Discussion

5.4.1 Density Measurements

The density measurement results can be seen in Figure 5.5. The apparent fractional packing density averaged approximately 55% of the overall density for 420 SS of 7740 (kg m^{-3}). In comparison the tapped fractional packing density averaged 59% of the overall density. This is in close relation to the tap density for monosized spherical powder of 60-64% obtained using the

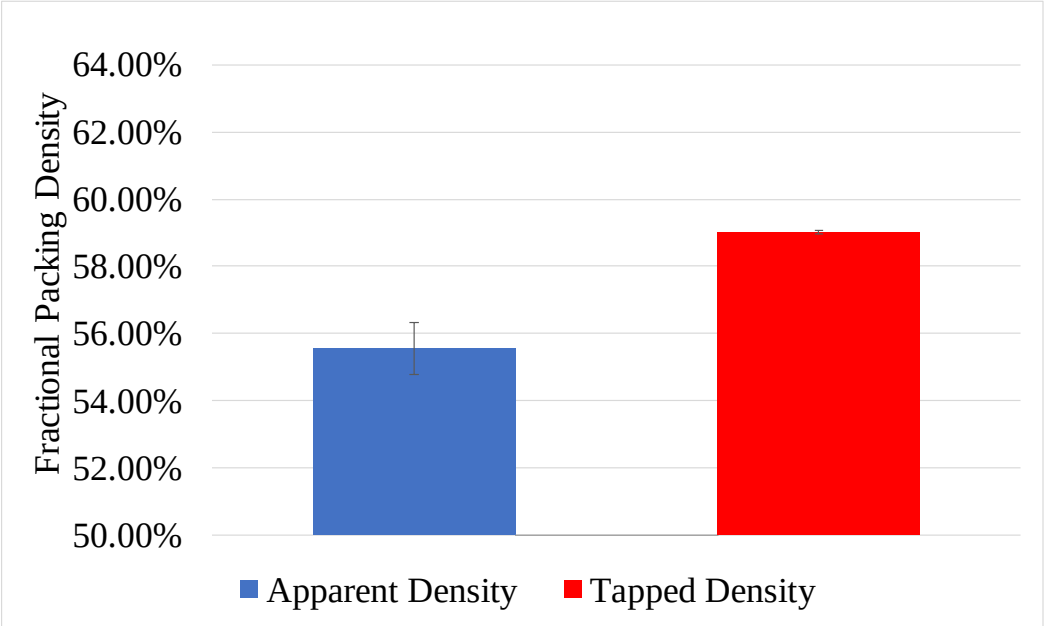

Figure 5.5 Fractional packing density comparison between apparent and tapped density of 420 SS powder

other method [56]. If the other method had been used an increase in tap density may have been seen, however, this 4% difference is sufficient for thermal diffusivity comparison purposes.

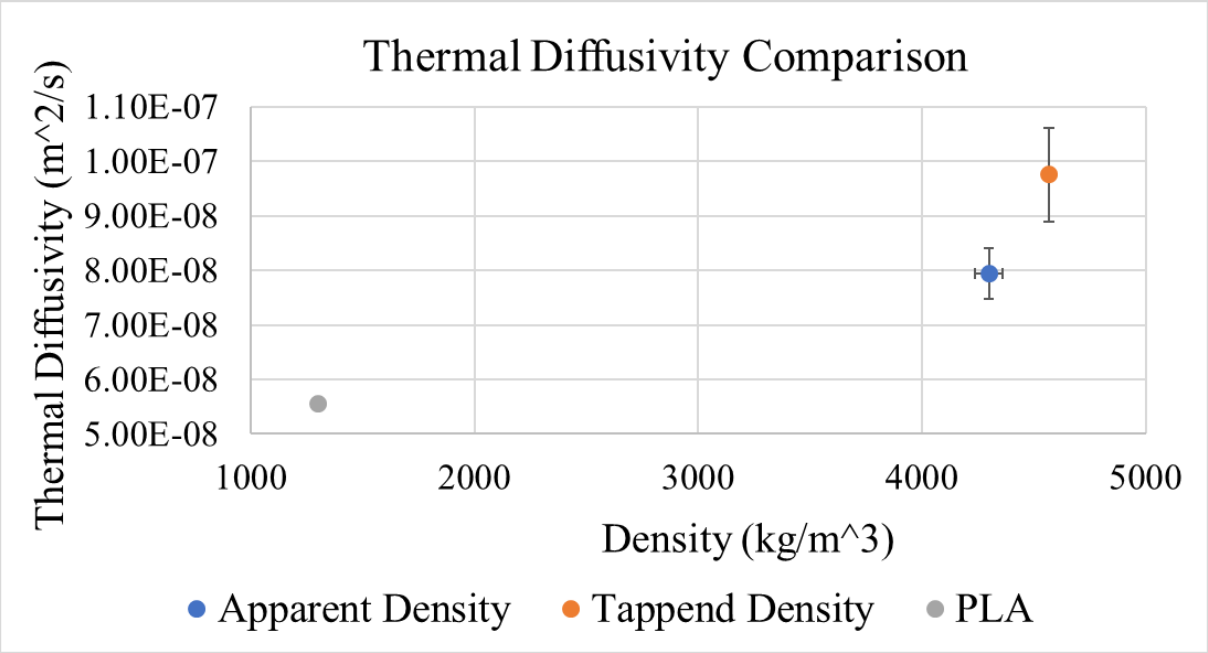

Figure 5.6 Thermal diffusivity comparison between apparent and tap density of raw 420 SS powder

5.4.2 Thermal Diffusivity Measurements

It can be seen from Figure 5.6 that the tapped density of raw 420 SS powder has a larger thermal diffusivity. The density increase was approximately 4%, however, from apparent to tap density the average thermal diffusivity increases approximately 23%. With specific heat remaining constant, this means the thermal conductivity increased over 30% between the two densities. The significant increase in thermal conductivity and diffusivity is because with the tap density, the interstitial void spaces between the powder particles is minimized. Thus, increasing the contact area between particles. The increase in contact area allows for a faster conductive heat transfer rate through the powder down to the defect depth. This was also shown by Alkahari et al [57] where the thermal conductivity of SUS 316L powder was compared to the bulk density. When the SUS 316L powder was compressed, the thermal conductivity increased with bulk density.

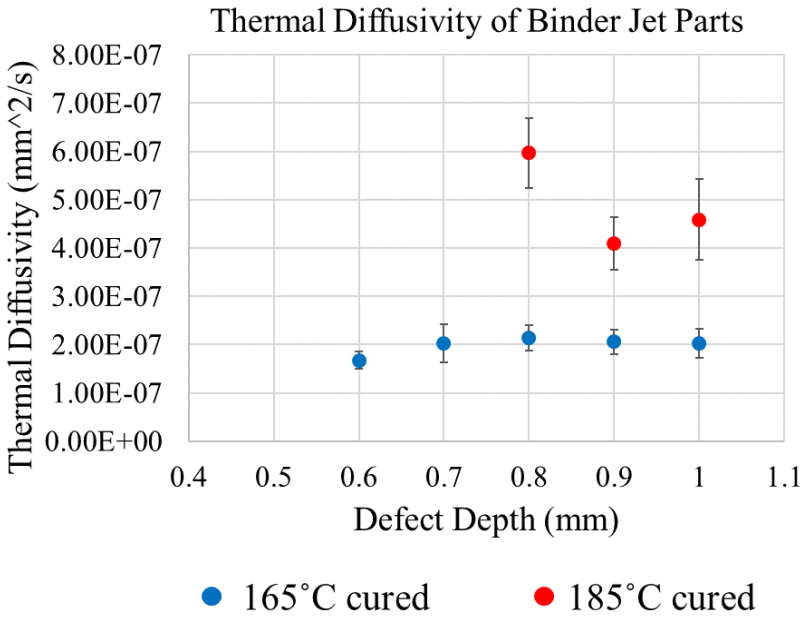

Figure 5.7 Thermal diffusivity comparison between two binder jet parts, one cured at 165˚C and the other at 185˚C

5.5 Binder Jet Results and Discussion

Pulse flashes ranging from 0.6 to 1.0s were used to thermally excite each part. Once an average thermal diffusivity was calculated for the deeper defects, the maximum allowable pulse length was used for each of the shallower defects to calculate thermal diffusivity. The results can be seen in Figure 5.7. For the 165˚C cured part, the thermal diffusivity was small enough that all the defect depths except for 0.5mm were able to be accurately calculated within the range of pulse lengths. However, the significant increase in thermal diffusivity from curing the part at 185˚C only allowed for the 0.8-1.0mm defects to be used for thermal diffusivity calculation. To measure the shallower defects due to the increase in thermal diffusivity, shorter pulse lengths must be used as not to exceed the maximum allowable pulse length. The reason for the increase in thermal diffusivity when curing at 185˚C is believed to be because the increase in temperature is needed for the binder to fully set among the powder particles in the part. At 185˚C, the fully

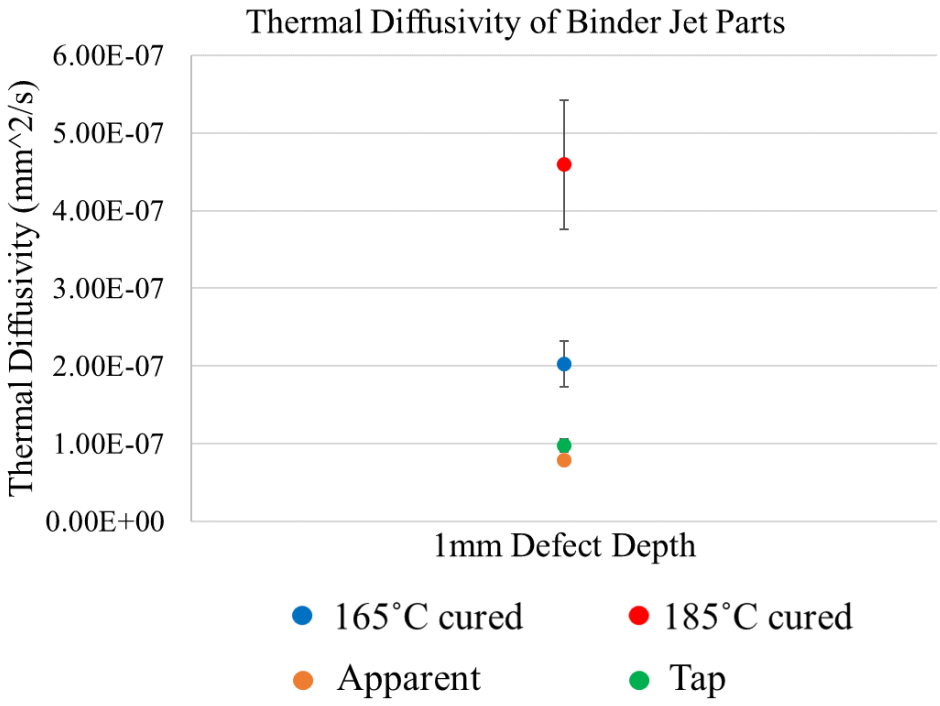

Figure 5.8 Comparison of thermal diffusivity between raw powder and cured green parts

set binder becomes crosslinked between the powder particles thus minimizing the surface contact heat resistance that occurs between powders simply touching. In turn, increasing the heat conduction mechanism within the part.

The overall average thermal diffusivity of the 185˚C cured part is approximately 1.5 times larger (150%) than the thermal diffusivity of the part cured at 165˚C. In comparison, the density only increased the thermal diffusivity of raw powder by 22%. Figure 5.8 shows how critical the curing temperature is to thermal diffusivity as the increase due to temperature difference is more than the increase from raw powder to the 165˚C cured part.

5.6 Conclusion

Based on the results, using the longer pulse method of PT, thermal diffusivity values of BJ parts can be calculated based on a known defect depth. It is important to ensure that when using the longer pulse method, that the pulse length does not exceed the maximum allowable

pulse length. Thus, for quantification of thermal diffusivity, deeper defects are ideal as the pulse times have a much larger range. The 4% increase between apparent and tapped density had a 22% increase in thermal diffusivity due to the increased contact points between the powder particles. Yet the curing temperature had the biggest impact on thermal diffusivity. Causing an increase in thermal diffusivity of approximately 150% between 165˚C curing temperature and 185˚C. Understanding how the BJ process parameters effect the thermal diffusivity of the green part could have significant quality benefits. Defects can be monitored and quantified during the build. Parameters such as drying time or bed temperature can be optimized, or even close loop controlled to increase build times and minimize energy use.

CHAPTER 6: CONCLUSION

The objective of this thesis was to understand the capability of using a modified form of Pulse Thermography (PT) for surface and sub-surface defect detection in additively manufactured parts. The primary modification made to the PT method is that of a longer pulse. The original assumption is that there is negligible internal temperature distribution for the method to accurately quantify sub-surface defects. This thesis looked at a comparative analysis to determine that the level of internal temperature distribution within a part is material specific. And in fact, based on the material's thermal properties and the defect depth a wide of pulse lengths can be used to accurately quantify defects within 5% error. Also, the added benefit of the longer pulse allows for surface characterization and defect detection via infrared reflections in the same test as subsurface defect detection. The following sections will highlight the key conclusions of the thesis as well as provide an insight into future work to further understand the capabilities of using a longer pulse with PT in AM.

6.1 Key Conclusions

6.1.1 Sub-Surface Defect Detection

One of the main driving assumptions with PT is that there is negligible internal temperature distribution following initial pulse heating of the surface of the part being tested. Therefore, previous work utilizing this method for sub-surface defect detection used flash bulbs with an average pulse range of 2-10ms to thermally excite the surface. With this pulse range, accurate defect detection was capable in numerous materials. However, the average thermal diffusivity of the materials tested using this method are significantly larger than the thermal

diffusivities from additively manufactured parts, specifically FDM and green BJ parts. It was noticed that depending on the thermal properties of the material being tested, different internal temperature distributions can exist with the same pulse length. Thus, the goal of this study was to understand, could this nondestructive testing method quantitatively be applied to additively manufactured parts using a longer pulse.

It was found that the assumption of negligible internal temperature distribution could be relaxed, and by using the starting point (t_0) at the halfway point of the pulse, a range of pulse lengths could be used to accurately quantify sub-surface defects in AM printed parts. Based on numerical simulation, the significance of having the starting point (t_0) be at the halfway point of the pulse is to nullify the effect of varying pulse lengths on the peak times used to quantify the defect depth. The peak times for a specific depth are based on the thermal properties of the material, therefore a method had to be determined to maximize accuracy for the same depth being pulse heated with, for example, a 100ms or a 400ms pulse. Using the halfway point of the pulse allows for this variation and basically normalizes the pulse length so that a range of pulse lengths can utilized to acquire the desired energy input.

With the FDM printed ABS and using the halfway point, defect depths of 0.3mm, 0.8mm, and 1.2mm were able to be accurately calculated with a longer pulse using the peak temperature contrast method. The log second derivative method had a much larger variation in the calculated depth and it was found out to be attributed to minor abrupt temperature adjustments made by the infrared camera. These abrupt temperature adjustments would occur instantaneously, jumping either up or down in temperature by approximately 0.07˚C as seen in Figure 2.1. This did not affect the peak temperature contrast slope method as it uses a reference area the abrupt temperature shift gets cancelled out. This will be further analyzed in the next

sections for future work. The defect depth of 1.8mm was calculated shallower than the actual defect by approximately 0.2mm. Using the 8x8mm defect width to calculate the depth, this is most likely attributed to the width to depth ratio being too small for the specific thermal properties of ABS. The affective defect width to depth ratio will be further discussed in the future works section.

6.1.2 Longer Pulse Capability and Limitations

Understanding the capability of quantifying defects using the longer pulse method of PT was the first part of this study. Upon determination that the longer pulse method proved successful, the next step was to determine and characterize what range of pulse lengths could be used based on the thermal diffusivity of the material being tested and the defect depth being analyzed. To understand the range of pulse lengths, four materials were analyzed using numerical simulations for defect depth quantification using both the peak temperature contrast slope method and the log seconder derivative method. The numerical simulation was ran through a MATLAB script that utilized the FTCS approximation method to determine the surface temperatures after pulse heating. Ensuring that $r < 0.5$, the MATLAB script was compared to Solidworks simulations and proved to be an accurate method for determining defect depths and thus was used for all numerical simulation results.

The four materials that were analyzed were Copper, ABS, PLA, and 316L SS. It was shown based on the thermal properties and depth of the defect, there is a limitation to the allowable pulse length that can be used for accurate defect detection. The maximum allowable pulse length for both the peak temperature contrast slope method and the log seconder derivative method is based on the peak times associated with each method. It was found that the maximum allowable pulse length cannot exceed 160% of the associated peak times to be within

approximately 5% error of the actual defect depth. Thus, depending on the method used to calculate the defect depth, this maximum allowable pulse length can vary.

The benefit of being able to maximize the pulse length allows for an increased range of materials to be analyzed using this method. It also creates the opportunity to optimize the pulse length to the desired depth for analysis based on a known thermal diffusivity. In turn, maximizing the energy into the part creating a larger thermal contrast between defective and sound regions. This increases the signal to noise ratio in the measurement and facilitates improved measurement accuracy.

6.1.3 Reflective Thermography

During the longer pulse, the radiant heat in the infrared spectrum will reflect off the part into the IR camera. Thus, upon completion of the pulse, shutters were engaged to block the thermal source from emitting more heat onto the part. It was found however, that these radiant reflections could be used to visually characterize the surface of additively manufactured parts and detect defects. For a sound surface with the roads running parallel to the thermal source, the infrared light would diffusely reflect off the surface and apparent surface temperature would appear the same across the face of the part. However, when a defect such as scrape or under extrusion is present, the light would specularly reflect into the IR camera creating a hotspot.

With a thermal resolution of approximately 75μm, defects as small as 181μm were able to be detected in the thermal images when the thermal source was parallel to the road direction. As mentioned in Chapter 4, it is important to note that the sensitivity of using infrared reflections for defect detection is based on the overall condition of the surface. If the surface is naturally rough with many defects, then the defects that can be visibly detected must be larger in size to differentiate. In contrast, for a part with a very smooth surface with minimal defects, the ability

to detect much smaller defects becomes possible. Also, with the thermal source perpendicular to the road direction, an approximate road width can be determined based on the specular reflections that occur at the edges of each road.

6.1.4 Thermal Diffusivity Measurement

The last part of this thesis looked at the capability of using the longer pulse method of PT to calculate the thermal diffusivity of BJ green parts and compare how density and curing temperature affect it. Previous work for BJ parts looked at optimizing process parameters to maximize the strength of the green part and reduce sintering shrinkage. However, understanding the thermal properties of the BJ part could help in determining optimal process parameters as well, such as the drying time and required energy input for desired bed temperature.

To understand how density effected the thermal diffusivity, a PLA fixture was used to simulate a 1mm defect. Then, apparent and tap density of 420 SS powder was thermally excited and the thermal diffusivity of each density was calculated using the peak temperature contrast slope method. The fractional packing tap density was calculated to be 4% larger than that of the apparent density. However, the tap density had a 22% larger calculated thermal diffusivity. This is due to the reduced void space between the particles under tap density and an increase in surface area contact between the powder particles. This increase in surface contact area between the powder particles significantly increased the conductive heat transfer mechanism through the powder to the defect.

When the two BJ parts were analyzed for thermal diffusivity based on curing temperature, it was found that the 185˚C curing temperature increased the thermal diffusivity approximately 150% compared to the 165˚C cured part. This increase in thermal diffusivity is attributed to the setting of the binder at the higher temperature. It is important to note that when

calculating the thermal diffusivity, the use of deeper defects is ideal as to minimize the chance of using a pulse that longer than the maximum allowable for the material. That is why the BJ parts tested had multiple defect depths for cross referencing purposes. Even with a significantly lower calculated thermal diffusivity for the 165˚C cured part than the 185˚C cured part, both were much higher than that of the raw powder. And the increase in thermal diffusivity from the different densities appeared minimal in comparison to the effect the binder and curing has on the part.

6.2 Future Work and Considerations

6.2.1 Defect Detection and Thermal Diffusivity Measurement

For sub-surface defect detection and thermal diffusivity measurements, future work is necessary to understand and quantify the width to depth ratio of the defect for accurate depth and thermal diffusivity calculations. This will help in understanding the limitations of the longer pulse method in defect depth quantification. It is also very beneficial for thermal diffusivity calculation as to ensure 3D conduction is occurring at the specified depth for accurate measurements. Future work is also needed for a more refined model and solution to the abrupt temperature shifts in the infrared data as to allow for experimental use of the log second derivative method with a longer pulse for defect depth quantification.

For the ability to use this method for online process monitoring, future work is needed to understand how a non-uniform initial internal temperature distribution affects the capability of accurate defect detection. Does a separate heat source need to be used to thermally excite the part being made, or for the case of FDM, is the temperature of the extruded material sufficient to reveal thermal contrasts on the surface? This is also crucial for understanding online capability for thermal diffusivity measurements in BJ parts. With the continuous heating of the powder bed,

how quickly do the thermal properties vary when the binder is added to the top layer? Could the drying heater be used for defect detection or is a separate thermal source needed?

Furthermore, all the analysis was done manually by visually inspecting the thermal response images. The area for the defective regions and the sound regions were manually chosen to create the temperature contrast and determine defect depth. Future work would need to look at automating the image analysis to automatically determine the defective and sound region as well as calculate the defect depth based on the thermal response.

6.2.2 Longer Pulse Capability

For the longer pulse capability, based on numerical simulations a range of pulse lengths can be used depending on the defect depth and thermal diffusivity. And a maximum pulse length was determined based on the peak times for each method. Future work is needed to experimentally correlate the accuracy of the calculated maximum pulse lengths. Although thermal losses proved to be negligible based on the simulations, an experimental understanding of the possible losses need to be analyzed for multiple materials. Also, as research continues, the focus of this study was understanding the effect the longer pulse has on two of the more common methods for defect detection. For proper understanding of how using a longer pulse effects PT, more quantification methods would need to be analyzed.

6.2.3 Reflective Thermography

Lastly, for reflective thermography, defect detection was solely based on visual analysis in this study. Future work is needed utilizing computer image analysis to identify, characterize, and determine defects based on the thermal images produced. Also, future work is needed to understand if there is a method to quantitatively analyze the hotspots when the thermal source is perpendicular to the roads and approximate a surface roughness. From an online monitoring

perspective this is very beneficial as surface roughness could be quickly analyzed during the process instead of post process. Creating the possibility for minimizing the need for post process operations to decrease surface roughness. Furthermore, from an online monitoring perspective, how would the reflections vary with multiple thermal sources surrounding the part during the printing process? Would there be a need for external thermal sources, and if so how would the thermal source be positioned so that it can be both perpendicular and parallel to the road direction at different times during the build.

REFERENCES

[1] J. W. Stansbury and M. J. Idacavage, "3D printing with polymers: Challenges among expanding options and opportunities," *Dental Materials*, vol. 32, no. 1, pp. 54-64, 1// 2016.

[2] I. Gibson, D. Rosen, and B. Stucker, *Additive manufacturing technologies : 3D printing, rapid prototyping, and direct digital manufacturing*. New York, NY : Springer, 2015. Second edition., 2015.

[3] M. Attaran, "The rise of 3-D printing: The advantages of additive manufacturing over traditional manufacturing," *Business Horizons*, vol. 60, no. 5, pp. 677-688, 2017/09/01/ 2017.

[4] S. Huang, P. Liu, A. Mokasdar, and L. Hou, "Additive manufacturing and its societal impact: a literature review," *International Journal of Advanced Manufacturing Technology*, Article vol. 67, no. 5-8, pp. 1191-1203, 2013.

[5] M. A. Arie, A. H. Shooshtari, and M. M. Ohadi, "Experimental characterization of an additively manufactured heat exchanger for dry cooling of power plants," *Applied Thermal Engineering*, vol. 129, pp. 187-198, 2018/01/25/ 2018.

[6] J. E. Seppala and K. D. Migler, "Infrared thermography of welding zones produced by polymer extrusion additive manufacturing," *Additive Manufacturing*, Article vol. 12, no. Part A, pp. 71-76, 10/1/October 2016 2016.

[7] R. Song and C. Telenko, "Material and energy loss due to human and machine error in commercial FDM printers," *Journal of Cleaner Production*, vol. 148, pp. 895-904, 2017/04/01/ 2017.

[8] T. Lieneke, V. Denzer, G. A. O. Adam, and D. Zimmer, "Dimensional Tolerances for Additive Manufacturing: Experimental Investigation for Fused Deposition Modeling," *Procedia CIRP*, vol. 43, pp. 286-291, 2016/01/01/ 2016.

[9] L. P. Zhang and Y. Y. Zhao, "Particle size distribution of tin powder produced by centrifugal atomisation using rotating cups," *Powder Technology*, vol. 318, pp. 62-67, 2017/08/01/ 2017.

[10] C. Kousiatza and D. Karalekas, "In-situ monitoring of strain and temperature distributions during fused deposition modeling process," *Materials & Design*, vol. 97, pp. 400-6, 05/05 2016.

[11] S. F. Costa, F. M. Duarte, and J. A. Covas, "Estimation of filament temperature and adhesion development in fused deposition techniques," *Journal of Materials Processing Technology,* vol. 245, pp. 167-179, 7// 2017.

[12] T. Craeghs, S. Clijsters, J. P. Kruth, F. Bechmann, and M. C. Ebert, "Detection of Process Failures in Layerwise Laser Melting with Optical Process Monitoring," *Physics Procedia,* vol. 39, pp. 753-759, 2012/01/01/ 2012.

[13] Y. Chivel and I. Smurov, "On-line temperature monitoring in selective laser sintering/melting," *Physics Procedia,* vol. 5, pp. 515-521, 2010/01/01/ 2010.

[14] S. Tammas-Williams, H. Zhao, F. Léonard, F. Derguti, I. Todd, and P. B. Prangnell, "XCT analysis of the influence of melt strategies on defect population in Ti–6Al–4V components manufactured by Selective Electron Beam Melting," *Materials Characterization,* vol. 102, no. Supplement C, pp. 47-61, 2015/04/01/ 2015.

[15] H. Rieder, A. Dillhöfer, M. Spies, J. Bamberg, and T. Hess, "Online monitoring of additive manufacturing processes using ultrasound," in *Proceedings of the 11th European Conference on Non-Destructive Testing, October*, 2014, pp. 6-10.

[16] S. E. Zeltmann, N. Gupta, N. G. Tsoutsos, M. Maniatakos, J. Rajendran, and R. Karri, "Manufacturing and security challenges in 3D printing," *JOM,* vol. 68, no. 7, pp. 1872-81, 07/ 2016.

[17] G. Guan *et al.*, "Evaluation of selective laser sintering processes by optical coherence tomography," *Materials & Design,* vol. 88, no. Supplement C, pp. 837-846, 2015/12/25/ 2015.

[18] C. Ibarra-Castanedo, J. R. Tarpani, and X. P. V. Maldague, "Nondestructive testing with thermography," *European Journal of Physics,* Article vol. 34, no. 6, pp. S91-S109, 2013.

[19] H. Krauss, C. Eschey, and M. Zaeh, "Thermography for monitoring the selective laser melting process," in *Proceedings of the Solid Freeform Fabrication Symposium*, 2012.

[20] J. Schwerdtfeger, R. F. Singer, and C. Korner, "In situ flaw detection by IR-imaging during electron beam melting," *Rapid Prototyping Journal,* vol. 18, no. 4, pp. 259-263, 2012.

[21] Z. Zhi, T. Ning, F. Lichun, and Z. Cunlin, "Specified value based defect depth prediction using pulsed thermography," *Journal of Applied Physics,* Report no. 2, p. 023112, 2012.

[22] D. Sharath, M. Menaka, and B. Venkatraman, "Defect Characterization Using Pulsed Thermography," *Journal of Nondestructive Evaluation,* Report no. 2, p. 134, 2013.

[23] J. G. Sun, "Analysis of pulsed thermography methods for defect depth prediction," *Journal of Heat Transfer,* no. 4, p. 329, 2006.

[24] T. Liang, W. Ren, G. Y. Tian, M. Elradi, and Y. Gao, "Low energy impact damage detection in CFRP using eddy current pulsed thermography," *Composite Structures,* vol. 143, pp. 352-361, 2016/05/20/ 2016.

[25] G. Tapia and A. Elwany, "A Review on Process Monitoring and Control in Metal-Based Additive Manufacturing," *Journal of Manufacturing Science and Engineering,* vol. 136, no. 6, pp. 060801-060801-10, 2014.

[26] S. K. Everton, M. Hirsch, P. Stravroulakis, R. K. Leach, and A. T. Clare, "Review of in-situ process monitoring and in-situ metrology for metal additive manufacturing," *Materials & Design,* vol. 95, no. Supplement C, pp. 431-445, 2016/04/05/ 2016.

[27] W. J. Parker, R. J. Jenkins, C. P. Butler, and G. L. Abbott, "Flash Method of Determining Thermal Diffusivity, Heat Capacity, and Thermal Conductivity," *Journal of Applied Physics,* vol. 32, no. 9, p. 1679, 09// 1961.

[28] H. I. Ringermacher, R. J. Archacki, and W. A. Veronesi, "Nondestructive testing: transient depth thermography," ed: Google Patents, 1998.

[29] S. M. Shepard, J. R. Lhota, B. A. Rubadeux, D. Wang, and T. Ahmed, "Reconstruction and enhancement of active thermographic image sequences," *Optical Engineering,* vol. 42, no. 5, p. 1337, 05// 2003.

[30] J. R. Pierce and N. B. Crane, "Preliminary Nondestructive Testing Analysis on 3D Printed Structure Using Pulsed Thermography," in *ASME 2017 International Mechanical Engineering Congress and Exposition*, 2017, pp. V008T10A083-V008T10A083: American Society of Mechanical Engineers.

[31] B. Anna and G. Selçuk, "Mechanical characterization of parts fabricated using fused deposition modeling," *Rapid Prototyping Journal,* vol. 9, no. 4, pp. 252-264, 2003/10/01 2003.

[32] S. Masamune and J. Smith, "Thermal conductivity of beds of spherical particles," *Industrial & Engineering Chemistry Fundamentals,* vol. 2, no. 2, pp. 136-143, 1963.

[33] J. W. Kim, K. W. Yun, and H. C. Jung, "Investigation of optimal thermal injection conditions and the capability of IR thermography for detecting wall-thinning defects in small-diameter piping components," *Nuclear Engineering and Design,* vol. 262, pp. 39-51, 2013/09/01/ 2013.

[34] D. P. Almond, S. L. Angioni, and S. G. Pickering, "Long pulse excitation thermographic non-destructive evaluation," *NDT & E International,* vol. 87, pp. 7-14, 2017/04/01/ 2017.

[35] D. W. Hahn and M. N. Ã–zisik, *Heat conduction*. John Wiley & Sons, 2012.

[36] J. Sun, "Method for determining defect depth using thermal imaging," 2003. Available: http://ezproxy.lib.usf.edu/login?url=http://search.ebscohost.com/login.aspx?direct=true&db=edspgr&AN=edspgr.06542849&site=eds-live.

[37] G. W. Recktenwald, "Finite-difference approximations to the heat equation," *Mechanical Engineering*, vol. 10, pp. 1-27, 2004.

[38] K. W. Morton and D. F. Mayers, *Numerical solution of partial differential equations: an introduction*. Cambridge university press, 2005.

[39] L. Villalpando, H. Eiliat, and R. J. Urbanic, "An Optimization Approach for Components Built by Fused Deposition Modeling with Parametric Internal Structures," *Procedia CIRP*, vol. 17, pp. 800-805, 2014/01/01/ 2014.

[40] L. M. Galantucci, F. Lavecchia, and G. Percoco, "Experimental study aiming to enhance the surface finish of fused deposition modeled parts," *CIRP Annals - Manufacturing Technology*, vol. 58, no. 1, pp. 189-192, 2009/01/01/ 2009.

[41] P. A. van Nijnatten, "Regular Reflectance and Transmittance," *Experimental Methods in the Physical Sciences*, vol. 46, pp. 143-178, 2014/01/01/ 2014.

[42] A. Höpe, "Diffuse Reflectance and Transmittance," *Experimental Methods in the Physical Sciences*, vol. 46, pp. 179-219, 2014/01/01/ 2014.

[43] M. K. Thompson *et al.*, "Design for Additive Manufacturing: Trends, opportunities, considerations, and constraints," *CIRP Annals*, vol. 65, no. 2, pp. 737-760, 2016/01/01/ 2016.

[44] Y. Bai, G. Wagner, and C. B. Williams, "Effect of Particle Size Distribution on Powder Packing and Sintering in Binder Jetting Additive Manufacturing of Metals," *Journal of Manufacturing Science and Engineering*, vol. 139, no. 8, pp. 081019-081019-6, 2017.

[45] H. Y. Sohn and C. Moreland, *The Effect of Particle Size Distribution on Packing Density*. 1968, pp. 162-167.

[46] M. Doyle, K. Agarwal, W. Sealy, and K. Schull, "Effect of Layer Thickness and Orientation on Mechanical Behavior of Binder Jet Stainless Steel 420 + Bronze Parts," *Procedia Manufacturing*, vol. 1, pp. 251-262, 2015/01/01/ 2015.

[47] H. Miyanaji, N. Momenzadeh, and L. Yang, "Effect of printing speed on quality of printed parts in Binder Jetting Process," *Additive Manufacturing*, vol. 20, pp. 1-10, 2018/03/01/ 2018.

[48] H. Miyanaji, S. Zhang, and L. Yang, "A new physics-based model for equilibrium saturation determination in binder jetting additive manufacturing process," *International Journal of Machine Tools and Manufacture*, vol. 124, pp. 1-11, 2018/01/01/ 2018.

[49] M. Vaezi and C. K. Chua, "Effects of layer thickness and binder saturation level parameters on 3D printing process," *The International Journal of Advanced Manufacturing Technology,* vol. 53, no. 1, pp. 275-284, 2011/03/01 2011.

[50] W. L. Vargas and J. J. McCarthy, "Conductivity of granular media with stagnant interstitial fluids via thermal particle dynamics simulation," *International Journal of Heat and Mass Transfer,* vol. 45, no. 24, pp. 4847-4856, 2002/11/01/ 2002.

[51] W. M. P. and B. M. L., "Modified curing protocol for improved strength of binder-jetted 3D parts," *Rapid Prototyping Journal,* vol. 23, no. 6, pp. 1195-1201, 2017.

[52] S. Joseph Gregorski, *High green density metal parts by vibrational compaction of dry powder in three dimensional printing process*. 2005.

[53] T. Do, P. Kwon, and C. S. Shin, "Process development toward full-density stainless steel parts with binder jetting printing," *International Journal of Machine Tools and Manufacture,* vol. 121, no. Supplement C, pp. 50-60, 2017/10/01/ 2017.

[54] A. Kumar, Y. Bai, A. Eklund, and C. B. Williams, "Effects of Hot Isostatic Pressing on Copper Parts Fabricated via Binder Jetting," *Procedia Manufacturing,* vol. 10, no. Supplement C, pp. 935-944, 2017/01/01/ 2017.

[55] A. Mostafaei, E. L. Stevens, E. T. Hughes, S. D. Biery, C. Hilla, and M. Chmielus, "Powder bed binder jet printed alloy 625: Densification, microstructure and mechanical properties," *Materials & Design,* vol. 108, pp. 126-135, 2016/10/15/ 2016.

[56] M. G. Randall, "Powder metallurgy science," *Metal Powder Industries Federation, Princeton, New Jersey, USA,* 1994.

[57] M. R. Alkahari *et al.*, "Thermal conductivity of metal powder and consolidated material fabricated via selective laser melting," in *Key Engineering Materials*, 2012, vol. 523, pp. 244-249: Trans Tech Publ.

APPENDIX A: MATLAB SCRIPT FOR PEAK TEMPERATURE CONTRAST METHOD

```
%% Constants for Heat analysis
clc
clear
format long
% Convection Coefficient
H = 10;

% Specific Heat
    %Cp = 1800; %PLA
    %Cp = 398; %Copper
    %Cp = 1386; % ABS
    Cp = 500; % Steel
% Density
    %P = 1300;
    %P = 8912;
    %P = 1020;
    P = 7990;
% Thermal Conductivity
    %K = 0.13;
    %K = 400;
    %K = 0.2256;
    K = 16.2;
% Thermal Diffusivity
    alpha = K/(Cp*P);
% Heat Flux in
    Q = 4000;
% Initial Temperature
    Ti = 298;
% Spacing Discretization in z
    del_xz = 0.000001;
% Time Discretizaton
    del_t = 0.0000001;
% r calculation for stability (r <= 0.5)
    R = (alpha*del_t)/((del_xz)^2);
% Depth of Starting Defect
    Dd = 0.0005+(2*del_xz);
% Starting Pulse Length
    P_Start = 0.022;
% Depth of Part
    D = 0.0015+(2*del_xz);
% Time of Analysis
    t_total = 0.04;
% Size of Matrix
    Rows_Sound = (D)/del_xz;
% Steps of Time
    t_total_step = t_total/del_t;
```

```
for z = 1:1:t_total_step+1
    X_Axis(1,z) = del_t.*z - del_t;
end
%% Creating 2-D Matrix of Internal Temp. Distribution for defect During Pulse

% Creating Time = 0 Matrix (Note: the 2nd row of elements is the surface)
for a = 1:1:round(Dd/del_xz)
    Part_Defect(a,1) = 298;
end

for z = 2:1:(round(P_Start/del_t))
    for x = 2:1:(round(Dd/del_xz))
        if x < (round(Dd/del_xz))
            Part_Defect(x,z) = ((1-(2*R)).*Part_Defect(x,z-
1))+(R.*(Part_Defect(x+1,z-1) + Part_Defect(x-1,z-1)));
            Part_Defect(1,z) = ((Q/K)*(2.*del_xz)) + ((-
H*(2*del_xz))/K)*(Part_Defect(2,z)-Ti) - (0.9*((2*del_xz)/K)*(5.67*10^(-
8))*((Part_Defect(2,z)^4-Ti^4)))  + Part_Defect(3,z-1);
            else
                Part_Defect((round(Dd/del_xz)),z) = ((-
H*(2*del_xz))/K)*(Part_Defect((round(Dd/del_xz))-1,z)-Ti)-
(0.9*((2*del_xz)/K)*(5.67*10^(-8))*((Part_Defect((round(Dd/del_xz))-1,z)^4) -
Ti^4))  + Part_Defect((round(Dd/del_xz))-2,z);
        end
    end
    z
end
%% Creating 2-D Matrix of Internal Temp. Distribution for defect After Pulse

for z = (round(P_Start/del_t))+1:1:t_total_step+1
    for x = 2:1:(round(Dd/del_xz))
        if x < (round(Dd/del_xz))
            Part_Defect(x,z) = ((1-(2*R)).*Part_Defect(x,z-
1))+(R.*(Part_Defect(x+1,z-1) + Part_Defect(x-1,z-1)));
            Part_Defect(1,z) = ((-H*(2*del_xz))/K)*(Part_Defect(1+1,z)-Ti)  -
(0.9*((2*del_xz)/K)*(5.67*10^(-8))*((Part_Defect(2,z)^4) - Ti^4)) +
Part_Defect(1+2,z);
        else
            Part_Defect((round(Dd/del_xz)),z) = ((-
H*(2*del_xz))/K)*(Part_Defect((round(Dd/del_xz))-1,z)-Ti)-
(0.9*((2*del_xz)/K)*(5.67*10^(-8))*((Part_Defect((round(Dd/del_xz))-1,z)^4) -
Ti^4))  + Part_Defect((round(Dd/del_xz))-2,z);
        end
    end
    z
end
%% Creating 2-D Matrix of Internal Temp. Distribution for sound area During
Pulse
for f = 1:1:round(D/del_xz)
    Part_Sound(f,1) = 298;
end

for e = 2:1:(round(P_Start/del_t))
    for g = 2:1:(round(D/del_xz))
        if g < (round(D/del_xz))
```

```
            Part_Sound(g,e) = ((1-(2*R)).*Part_Sound(g,e-
1))+(R.*(Part_Sound(g+1,e-1) + Part_Sound(g-1,e-1)));
            Part_Sound(1,e) = ((Q/K)*(2.*del_xz))+ ((-
H*(2*del_xz))/K)*(Part_Defect(2,e)-Ti) - (0.9*((2*del_xz)/K)*(5.67*10^(-
8))*((Part_Sound(2,e)^4) - Ti^4)) + Part_Sound(3,e-1);
        else
            Part_Sound((round(D/del_xz)),e) = ((-
H*(2*del_xz))/K)*(Part_Sound((round(D/del_xz))-1,e)-Ti)-
(0.9*((2*del_xz)/K)*(5.67*10^(-8))*((Part_Sound((round(Dd/del_xz))-1,e)^4) -
Ti^4))  + Part_Sound((round(D/del_xz))-2,e);
        end
    end
    e
end

%% Creating 2-D Matrix of Internal Temp. Distribution for sound area After
Pulse

for e = (round(P_Start/del_t))+1:1:t_total_step+1
    for g = 2:1:(round(D/del_xz))
        if g < (round(D/del_xz))
            Part_Sound(g,e) = ((1-(2*R)).*Part_Sound(g,e-
1))+(R.*(Part_Sound(g+1,e-1) + Part_Sound(g-1,e-1)));
            Part_Sound(1,e) = ((-H*(2*del_xz))/K)*(Part_Sound(1+1,e)-Ti)-
(0.9*((2*del_xz)/K)*(5.67*10^(-8))*((Part_Sound(2,e)^4) - Ti^4)) +
Part_Sound(1+2,e);
        else
            Part_Sound((round(D/del_xz)),e) = ((-
H*(2*del_xz))/K)*(Part_Sound((round(D/del_xz))-1,e)-Ti)-
(0.9*((2*del_xz)/K)*(5.67*10^(-8))*((Part_Sound((round(Dd/del_xz))-1,e)^4) -
Ti^4))  + Part_Sound((round(D/del_xz))-2,e);
        end
    end
    e
end
%% Need to Remember that the ACTUAL surface location is the SECOND ROW

Temperature_Defect = Part_Defect(2,:);
Temperature_Sound = Part_Sound(2,:);

%figure
%plot(X_Axis,Temperature_Defect)

%figure
%plot(X_Axis,Temperature_Sound)

Temperature_Contrast = Temperature_Defect-Temperature_Sound;

figure
plot(X_Axis,Temperature_Contrast)

for s = 2:1:t_total_step
    Temp_Contrast_Deriv(1,s) = (Temperature_Contrast(1,s+1) -
Temperature_Contrast(1,s-1))/del_xz;
end
```

```
[Peak Time] = max(Temp_Contrast_Deriv(:));
ts = Time*del_t - (P_Start/2)+del_t;

Defect_depth_Temp_Contrast_Method = (sqrt((ts*alpha*pi^2)/3.64))*1000;

Defect_Calculation = Defect_depth_Temp_Contrast_Method
```

APPENDIX B: MATLAB SCRIPT FOR LOG SECOND DERIVATIVE METHOD

```
%% Constants for Heat analysis
clc
clear
format long
% Convection Coefficient
H = 10;

% Specific Heat
    %Cp = 1800; %PLA
    Cp = 398; %Copper
    %Cp = 1386; % ABS
    %Cp = 500; % Steel
% Density
    %P = 1300;
    P = 8912;
    %P = 1020;
    %P = 7990;
% Thermal Conductivity
    %K = 0.13;
    K = 400;
    %K = 0.2256;
    %K = 16.2;
% Thermal Diffusivity
    alpha = K/(Cp*P);

% Heat Flux in
    Q = 5000000;
% Initial Temperature
    Ti = 298;
% Spacing Discretization in z
    del_xz = 0.000015;
% Time Discretization
    del_t = 0.0000008;

% r calculation for stability (r <= 0.5)
    R = (alpha*del_t)/((del_xz)^2);
% Depth of Starting Defect
    Dd = 0.002+(2*del_xz);
% Starting Pulse Length
    P_Start = 0.012;
% Depth of Part
    D = 0.001+(2*del_xz);
% Time of Analysis
    t_total = 0.07;
% Size of Matrix
    Rows_Sound = (D)/del_xz;
```

```
% Steps of Time
    t_total_step = t_total/del_t;

for z = 1:1:t_total_step+1
    X_Axis(1,z) = del_t.*z - del_t;
end
%% Creating 2-D Matrix of Internal Temp. Distribution for defect During Pulse

% Creating Time = 0 Matrix (Note: the 2nd row of elements is the surface)
for a = 1:1:round(Dd/del_xz)
    Part_Defect(a,1) = 298;
end

for z = 2:1:(round(P_Start/del_t))
    for x = 2:1:(round(Dd/del_xz))
        if x < (round(Dd/del_xz))
            Part_Defect(x,z) = ((1-(2*R)).*Part_Defect(x,z-
1))+(R.*(Part_Defect(x+1,z-1) + Part_Defect(x-1,z-1)));
            Part_Defect(1,z) = ((Q/K)*(2.*del_xz)) + ((-
H*(2*del_xz))/K)*(Part_Defect(2,z)-Ti) - (0.9*((2*del_xz)/K)*(5.67*10^(-
8))*((Part_Defect(2,z)^4-Ti^4))) + Part_Defect(3,z-1);
            else
                Part_Defect((round(Dd/del_xz)),z) = ((-
H*(2*del_xz))/K)*(Part_Defect((round(Dd/del_xz))-1,z)-Ti)-
(0.9*((2*del_xz)/K)*(5.67*10^(-8))*((Part_Defect((round(Dd/del_xz))-1,z)^4) -
Ti^4)) + Part_Defect((round(Dd/del_xz))-2,z);
        end
    end
    z
end
%% Creating 2-D Matrix of Internal Temp. Distribution for defect After Pulse

for z = (round(P_Start/del_t))+1:1:t_total_step+1
    for x = 2:1:(round(Dd/del_xz))
        if x < (round(Dd/del_xz))
            Part_Defect(x,z) = ((1-(2*R)).*Part_Defect(x,z-
1))+(R.*(Part_Defect(x+1,z-1) + Part_Defect(x-1,z-1)));
            Part_Defect(1,z) = ((-H*(2*del_xz))/K)*(Part_Defect(1+1,z)-Ti) -
(0.9*((2*del_xz)/K)*(5.67*10^(-8))*((Part_Defect(2,z)^4-Ti^4))) +
Part_Defect(1+2,z);
        else
            Part_Defect((round(Dd/del_xz)),z) = ((-
H*(2*del_xz))/K)*(Part_Defect((round(Dd/del_xz))-1,z)-Ti) -
(0.9*((2*del_xz)/K)*(5.67*10^(-8))*((Part_Defect((round(Dd/del_xz))-1,z)^4) -
Ti^4)) + Part_Defect((round(Dd/del_xz))-2,z);
        end
    end
    z
end

%% Need to Remember that the ACTUAL surface location is the SECOND ROW

Temperature_Defect_Ti = Part_Defect(2,:);

Temperature_Defect = Temperature_Defect_Ti - 298;
```

```
Ln_Temp_Defect = log(Temperature_Defect);
Ln_X_Axis = log(X_Axis);

for k = 1:1:(t_total_step - round(P_Start/del_t))
    Post_pulse_Ln_Temp_Defect(1,k) =
Ln_Temp_Defect(1,((k)+(round(P_Start/del_t))));
end

for g = 1:1:(t_total_step - round(P_Start/del_t))
    Post_pulse_Ln_X_Axis(1,g) = Ln_X_Axis(1,g);
end

%figure
%plot(Post_pulse_Ln_X_Axis,Post_pulse_Ln_Temp_Defect)


[ROW COLUMN] = size(Post_pulse_Ln_Temp_Defect);

for e = 2:1:COLUMN-1
    Ln_2nd_Deriv(1,e-1) = (Post_pulse_Ln_Temp_Defect(1,e+1) -
(2*Post_pulse_Ln_Temp_Defect(1,e)) + Post_pulse_Ln_Temp_Defect(1,e-
1))/((Post_pulse_Ln_X_Axis(1,e)-Post_pulse_Ln_X_Axis(1,e-1))^2);
end

for f = 1:1:COLUMN-2
    Ln_2nd_Deriv_X_Axis(1,f) = Post_pulse_Ln_X_Axis(1,f);
end

%fit = polyfit(Post_pulse_Ln_X_Axis,Post_pulse_Ln_Temp_Defect,7);

%for a = 2:1:8
%    fit1(1,a-1) = fit(1,a)*(8-a);
%end

%for b = 1:1:6
%    fit2(1,b) = fit1(1,b)*(6-b);
%end

%for d = 1:1:(t_total_step - round(P_Start/del_t))
%    Ln_2nd_deriv_Temp(1,d) =
(fit2(1,1)*Post_pulse_Ln_X_Axis(1,d)^4)+(fit2(1,2)*Post_pulse_Ln_X_Axis(1,d)^
3)+(fit2(1,3)*Post_pulse_Ln_X_Axis(1,d)^2)+(fit2(1,4)*Post_pulse_Ln_X_Axis(1,
d))+(fit(1,5));
%end

%for w = 100:1:(t_total_step - round(P_Start/del_t))
%    Updated_Ln_2nd_deriv_Temp(1,w-99) = Ln_2nd_deriv_Temp(1,w);
%end

%for w = 100:1:(t_total_step - round(P_Start/del_t))
%    Updated_Ln_X_Axis(1,w-99) = Post_pulse_Ln_X_Axis(1,w);
%end
```

```
figure
plot(Ln_2nd_Deriv_X_Axis,Ln_2nd_Deriv)


[Peak Time] = max(Ln_2nd_Deriv(:));

Actual_Time = exp(Ln_2nd_Deriv_X_Axis(1,Time));

ts = Actual_Time + (P_Start/2)+del_t;

Defect_depth_Temp_log2nd_Method = (sqrt(ts*alpha*pi))*1000;

Defect_Calculation = Defect_depth_Temp_log2nd_Method

%figure
%plot(Temp_Contrast_Deriv)
```